UNIVERSITÀ
DEGLI STUDI
DI TRIESTE

Università degli Studi di Trieste
XXXVII Ciclo del Dottorato di Ricerca in
Ingegneria dell'Informazione e Industriale

Ente finanziatore: Elettra Sincrotrone Trieste S.C.p.A.

From Pixels to Diagnosis: Applications of X-ray Virtual Histology in Clinical Pathology

Settore scientifico-disciplinare: IBIO-01/A Bioingegneria

Dottoranda:
Giulia Saccomano

Coordinatore di corso:
Prof. Fulvio Babich
(Università degli Studi di Trieste)

Supervisore:
Prof. Francesco Brun
(Università degli Studi di Trieste)

Co-Supervisore:
Dr. Diego Dreossi
(Elettra Sincrotrone Trieste S.C.p.A.)

Anno Accademico 2023/2024

From pixels to diagnosis: applications of X-ray virtual histology in clinical pathology

Giulia Saccomano
Matr. PHD1200058

University of Trieste
Dept. of Architecture and Engineering
Via A. Valerio 6/1
34126 Trieste TS, Italy

Elettra Sincrotrone Trieste S.C.p.A.
Area Science Park - S.S. 14, km 163.5
34149 Basovizza TS, Italy

Summary

Histopathology is the medical discipline that studies the signs and characteristics of human disease processes in biological tissues. In the field of clinical diagnostics, the histopathological examination is a fundamental step in the process of defining the diagnosis, prognosis, and treatment plan. Despite the advancement of technology and the production of increasingly accurate and robust results, the two-dimensional information obtained through histopathology remains constrained by the sectioning plane. In contrast, X-ray virtual histology (XVH) represents an emerging imaging technique that produces high-resolution three-dimensional insights at the microscopic level, thereby overcoming the two-dimensional limitation of conventional histology. By leveraging the intrinsic characteristics of X-rays to capture comprehensive microarchitectural information, XVH could reduce the reliance on physical sectioning of the biological specimen, thereby preserving its structural integrity.

This thesis aims to apply synchrotron-based XVH to two of the most aggressive and heterogeneous cancer types, which are melanoma skin cancer and non-small cell lung cancer (NSCLC). The need for superior image resolution and contrast provided by synchrotron light is essential for detecting subtle morphological variations within tumors. These capabilities are of particular significance for the investigation of infiltrative characteristics that drive tumor invasion, a process that may require further examination to gain a comprehensive understanding of its underlying mechanisms. In this work, the invasive phenotypes of melanoma, such as melanocytic nests and pagetoid spread, were translated from histopathology to XVH for the first time. Moreover, three-dimensional reconstruction of some adverse prognostic factors in NSCLC, such as spread through air spaces (STAS), pleural invasion, and lympho-vascular invasion, demonstrates the superiority of XVH over other experimental techniques in terms of image quality and diagnostic potential. To effectively manage and analyze the large datasets generated by XVH, an important contribution of this thesis lies in the integration of advanced deep learning algorithms for the automated segmentation and classification of tumor tissues. This approach enhances the identification of critical features such as cellular architecture, tumor boundaries, and vasculature, thereby streamlining the interpretation of complex histological data.

In addition to synchrotron-based imaging, this thesis also provides a preliminary exploration of the potential of laboratory-based X-ray virtual histology systems. By qualitatively comparing the performance of a phase-contrast X-ray imaging laboratory, this study anticipates their potential to broaden access to XVH technology. Unlike synchrotrons, which are limited in availability and unlikely to meet the routine needs of clinical settings, laboratory-based systems could provide a more practical and accessible solution for both clinical and research applications.

The overarching objective of this thesis is to advance the technical development of X-ray virtual histology while also enhancing its clinical relevance through close collaboration with medical professionals. This work aims to highlight the promising potential of X-ray virtual histology in cancer diagnostics and research by serving as a critical bridge between the technical advancements pursued by engineers and physicists and the clinical insights provided by medical doctors. Through this interdisciplinary approach, the thesis facilitates the translation of this innovative imaging technology into practical medical applications.

Sommario

L'istopatologia è la disciplina medica che studia le alterazioni struttuali dei tessuti biologici nei processi patologici. Nel campo della diagnostica clinica, l'esame istopatologico è di fondamentale importanza nella definizione della diagnosi, della prognosi e della terapia. Nonostante l'avanzamento tecnologico della tecnica e la produzione di risultati sempre più robusti e accurati, le informazioni bidimensionali ottenute tramite l'esame istopatologico rimangono vincolate al piano di sezionamento. Al contrario, l'istologia virtuale a raggi X, in inglese X-ray Virtual Histology (XVH), è una tecnica di imaging emergente che produce osservazioni interne tridimensionali ad alta risoluzione. Inoltre, sfruttando le proprietà di interazione dei raggi X con la materia per acquisire informazioni strutturali, la tecnica XVH elimina la necessità di sezionare fisicamente il campione biologico, preservandone l'integrità strutturale.

Questa tesi di dottorato si propone di applicare l'istologia virtuale a raggi X impiegando la luce di sincrotrone a due tipologie di tumore molto aggressive, quali il melanoma e il cancro al polmone a non-piccole cellule (NSCLC). La luce di sincrotrone è essenziale per garantire elevata risoluzione e contrasto dell'immagine, utili per rilevare le sottili variazioni morfologiche tissutali. Tali fattori sono particolarmente importanti per guidare l'indagine sul processo di invasività dei tumori, sul quale manca tutt'ora una comprensione completa dei meccanismi scatenanti. In questo lavoro, i fenotipi invasivi del melanoma, quali i nidi melanocitici e la diffusione pagetoide, sono stati tradotti per la prima volta dall'istopatologia alla XVH. Inoltre, la ricostruzione della micro-architettura di alcuni fattori prognostici avversi nel NSCLC, come la diffusione attraverso gli spazi aerei (STAS), l'invasione pleurica e l'invasione linfovascolare, hanno dimostrato la superiorità della XVH rispetto ad altre tecniche sperimentali in termini sia di qualità dell'immagine che di potenziale diagnostico. Inoltre, l'impiego di algoritmi avanzati di deep learning per segmentare automaticamente i tessuti hanno facilitato l'identificazione di caratteristiche critiche come l'organizzazione cellulare, i confini tumorali e la vascolarizzazione.

Oltre all'imaging di XVH con luce di sincrotrone, questa tesi esplora in modo preliminare il potenziale della tecnica XVH con sorgenti da laboratorio. Confrontando solo qualitativamente i risultati ottenuti mediante una tecnica a contrasto di fase con sorgenti da laboratorio, questo lavoro valuta il loro potenziale per facilitare un più ampio accesso alla tecnologia XVH in contesti clinici e di ricerca. Infatti, al contrario dei sincrotroni, la cui accessibilità è limitata e difficilmente possono soddisfare le esigenze di routine degli ambienti clinici, i sistemi da laboratorio potrebbero rappresentare una soluzione più pratica e accessibile sia per applicazioni cliniche che di ricerca.

Obiettivo ultimo di questa tesi è quello di far progredire lo sviluppo tecnico

dell'istologia virtuale a raggi X, migliorandone al contempo la rilevanza clinica attraverso una stretta collaborazione con i professionisti del settore medico. Questo lavoro mira ad evidenziare il promettente potenziale dell'istologia virtuale a raggi X nella diagnostica medica e nella ricerca sul cancro, fungendo da ponte critico tra i progressi tecnici perseguiti da ingegneri e fisici e le intuizioni cliniche fornite dai medici. Attraverso questo approccio interdisciplinare, la tesi vuole facilitare la traslazione di questa innovativa tecnologia di imaging verso applicazioni pratiche.

Contents

List of Abbreviations

Adk	Adenocarcinoma
AI	Artificial Intelligence
BCC	Basal Cell Carcinoma
CNN	Convolutional Neural Network
CNR	Contrast-to-Noise Ratio
CT	Computed Tomography
DL	Deep Learning
FBP	Filtered Back Projection
FDK	Feldkamp Kress Davis
FFPE	Formalin-Fixed Paraffin-Embedded
FOV	Field-Of-View
LVI	Lympho-Vascular Invasion
Micro-CT	Computed micro-Tomography
MIP	Micropapillary
Mis	Melanoma In Situ
ML	Machine Learning
MRI	Magnetic Resonance Imaging
NMM	Nodular Malignant Melanoma
NMSC	Non-Melanoma Skin Cancer
NSCLC	Non-Small Cell Lung Cancer
OCT	Optical Coherence Tomography
PET	Positron Emission Tomography
PBI	Propagation-Based Imaging

ROI	Region-Of-Interest
SCLC	Small Cell Lung Cancer
SDD	Sample-to-Detector Distance
SN	Solid Nest
SqCC	Squamous Cell Carcinoma
SSD	Sample-to-Source Distance
SSM	Superficial Spreading Melanoma
STAS	Spread Through Air Spaces
TNM	Tumor Node Metastasis
VOI	Volume-Of-Interest
XVH	X-ray Virtual Histology
XPCT	X-ray Phase-Contrast Tomography
WHO	World Health Organization
WSI	Whole Slide Imaging

List of Figures

List of Tables

CHAPTER 1

Introduction

In the last forty years, technological improvement in the data science field has been remarkable. The increase in computer capabilities, the rapid development in the manufacturing of X-ray detectors, and the activity of the scientific community have guided the future of clinical diagnostics. Among these advancements, X-ray Virtual Histology (XVH) has emerged as a powerful imaging tool for non-invasive tissue analysis, offering unprecedented insights into biological structures. Such technique has mainly been employed for preclinical and medical purposes, such as support for histopathological examination. Thanks to its high resolution and contrast data, XVH is mainly limited to synchrotron facilities. Yet, its availability is limited to selected groups of researchers that can access these facilities. However, improvement in hardware components (e.g., laser jet X-ray sources, photon counting detectors), imaging methods (e.g., phase-contrast imaging), and software (e.g., AI-driven data processing tools) has also favored the application of XVH in highly specialized laboratory setups.

One of the greatest benefits of Artificial Intelligence (AI) methods is the capacity of rapidly extracting and processing vast quantities of data. This aspect has facilitated the fast processing of huge amount of data available, which would otherwise necessitate the involvement of a considerable number of professionals for its processing and interpretation. In the last twenty years, many research studies have been published thanks to the aid of AI in medicine, testifying the effectiveness in the fields. Furthermore, since the most requested attribute of an AI application in the medical field is data scalability, this technology aligns well with international guidelines and standardized methods of the clinical sector. On the contrary, experimental data often exhibits a higher degree of variability due to the independence of research laboratories and the diverse experimental setups they employ. This variability can pose challenges to repeatability in data processing and analysis. These challenges arise because data acquisition in experimental laboratories is highly dependent on the specific technologies (e.g., source and detector supplier) and the availability of specimens. Furthermore, current state-of-the-art segmentation algorithms struggle with low-contrast and low-resolution variability between tissues and cellular components. Additionally, AI-based algorithms can prove beneficial when dealing with limited data availability and can favor tools that are not system-dependent.

For these reasons, coupling X-ray virtual histology with AI-based segmentation methods for automated data processing can allow for precise tissue classification and segmentation, paving the way for more accurate and efficient histopathological assessments. Til now, it has been mainly considered for experimental use but the technique holds the potential to become a versatile tool even in clinical routine.

1.1 Goal of the Thesis

The goal of the thesis is to present the potential application of X-ray Virtual Histology in the diagnosis of melanoma and lung cancers. This is supported by the production of scientific dissemination in the field of new advanced techniques and their clinical impact. In particular, the aim is to further develop novel methods and insights for imaging biological samples without any staining in a large-scale facility. A specific emphasis is placed on enhancing the diagnostic capabilities of XVH by elucidating the invasive characteristics of tumors and other prognostic variables.

The preliminary XVH results obtained via laboratory setups are also shown, along with a discussion of future perspectives. In summary, the research aims to:

- Enhance image quality optimizing all experimental variables, including the acquisition and reconstruction parameters, when performing synchrotron-based XVH;
- Evaluate the efficacy of XVH in comparison with conventional histological methods;
- Provide insights into the potential of XVH as a tool for improved cancer diagnostics and treatment planning, particularly in melanoma and NSCLC;
- Explore the potential of deep learning and machine learning methods to extract pathological features from XVH data;
- Investigate the most promising approach of application of this imaging modality to a laboratory-based setup, enabling broader access beyond synchrotron facilities.

This work aims to contribute to advancing the use of X-ray imaging in medical and preclinical research and diagnostics, offering a non-destructive alternative to conventional histology capable to provide more insight in several practical applications.

To do so, this research has been conducted in collaboration with several facilities and institutions. The Department of Pathology of the University Hospital of Cattinara (Trieste, Italy) provided the samples. Data acquisition and reconstruction were conducted at the SYRMEP beamline (Elettra synchrotron - Trieste, Italy) and at the laboratory of OptImaTo (University of Trieste - Trieste, Italy). Finally, data analysis was performed at the Computational Pathology Group (Radboud University Medical Center - Nijmegen, The Netherlands).

1.2 Outline of the Thesis

The outline of the thesis is as follows:

- Chapter 2 reports an overview of the pathology, etiology, and classification of the cancer types analyzed in this study, which are melanoma and lung cancer.
- Chapter 3 mounts a technical description of the methodologies used in this study, from imaging techniques, such as conventional histology and X-ray phase-contrast tomography, to deep learning models.
- Chapter 4 describes the materials and methods employed for all scientific experiments presented in this thesis in the following chapters.
- Chapter 5 exposes the findings of the optimization process for selected variables that influence the performance of X-ray virtual histology using the synchrotron configuration setup.
- Chapter 6 presents the results of synchrotron-based XVH in the study of skin tumors, with a particular focus on melanoma.
- Chapter 7 describes the development and application of a semantic segmentation model to detect the melanocytic lesion in XVH images.
- Chapter 8 explores the application of synchrotron-based XVH in the study of non-small cell lung cancers, focusing on histological invasive patterns and features.
- Chapter 9 shows preliminary results obtained by applying XVH with a laboratory X-ray source.
- Chapter 10 summarizes all the findings and discusses the future implications of XVH in the biomedical context.
- Chapter 11 draws the conclusion.

CHAPTER 2

Cancer Pathology

Cancer is one of the most studied disease in the healthcare field. It is the uncontrollable growth of abnormal and damaged cells that may spread to other parts of the body. These cells are affected by genetic alterations, which makes them unresponsive to biological signals. With the aid of imaging, molecular testing, and genetics, research on this topic is constantly improving. However, knowledge on specific types of cancer still needs further attention in order to fully grasp their dynamics. Cancer incidence can be traced to several elements, such as lifestyle, environmental factors, and age. In this chapter, a section is dedicated to the description of cancer phenomena and its statistics, as well as a comprehensive overview of melanoma and lung cancers. The objective is to build the foundations to fully understand the subsequent chapters. The rationale behind the selection of these specific cancers was based on their classification as the two most lethal forms of cancer worldwide. According to [1], lung cancer leads the statistic as the most diagnosed and deadliest form of cancer, while melanoma has the highest ratio between diagnosis and death.

2.1 Cancer Epidemiology

Cancer is a genetic disease that is caused by changes to genes that control the way our cells function, especially how they grow and divide. In a normal condition, human cells grow and multiply to form new ones in order to replace those which have grown old or have been damaged. When this process breaks down, abnormal or damaged cells may grow and multiply uncontrollably leading to the formation of tumors. Tumors are lumps of tissue that can be benign, not cancerous, or malignant, cancerous. Benign tumors do not spread into nearby tissues and, when removed, they usually do not grow back. On the contrary, cancerous tumors are well known to invade nearby tissues and travel to distant places in the body to form new tumors, named metastasis.

Cancer cells differ from normal cells for several factors [2] [3]: firstly, they grow in the absence of signals telling them to grow, while at the same time ignoring those that order them to stop dividing and multiplying (phase M, mitosis) or to die (apoptosis). Then, tumors grow towards blood vessels since they are supplied with oxygen and nutrients by them. Finally, cancer cells may underwent multiple changes in their chromosomes, and they can trick the immune system into protecting their growth instead of attacking them.

To date, over 100 types of cancers have been identified, each one named after the organ or tissue from which it originates (e.g., lung or brain) and the type of cell from

which it develops (e.g., epithelial or squamous cells).

The incidence of cancer is higher in elderly people than young ones due to the deceleration of biological processes [4]. This is connected to the capacity of the body to eliminate cells with damaged DNA before they become cancerous, which declines with age. Such phenomenon showcases the correlation of higher cancer risks in later life. However, those affected have an unique combination of genetic changes that are different from others. In order to fully understand how cancer develops and should be treated, their classification and study through multi-techniques is crucial.

2.1.1 Cancer Statistics

In 2020, a global statistics provided by the World Health Organization (WHO) indicates that female breast cancer is the most prevalent cancer affecting both genders (11.4% of all cases), followed by lung cancer (10.8%), prostate cancer (7.3%), and non-melanoma skin cancer (6.1%). However, when the data is stratified by cancer mortality, lung cancer is the most lethal disease (18.0%), followed by liver (8.3%), stomach (7.7%), and breast cancer (6.9%) [5].

New data has been provided for 2022, changing the worldwide scenario. Figure 2.1 reports a graphical representation of the incidence and mortality rates of all cases of cancer diagnosed worldwide 2.1(a) and in Europe 2.1(b) in 2022.

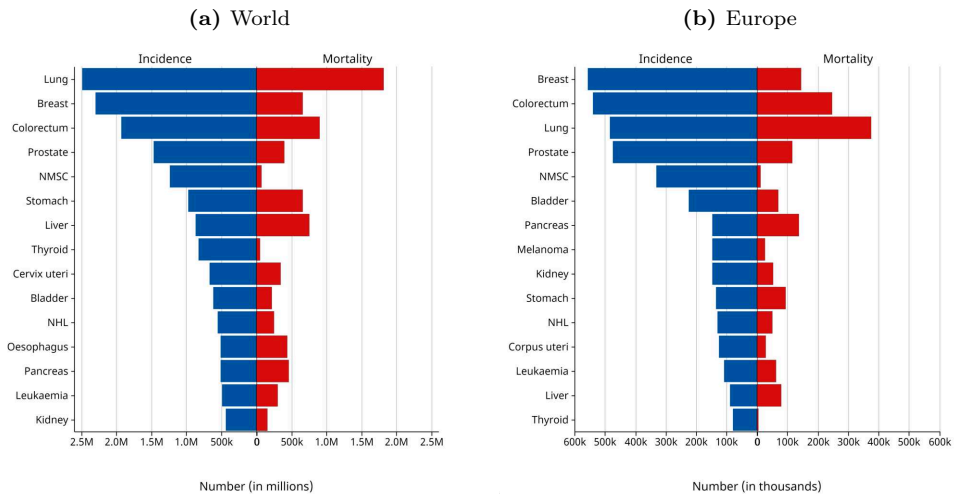

Figure 2.1. The incidence and mortality of cancer cases in absolute numbers (a) worldwide and (b) in European countries in 2022. Acronyms: NMSC, non-melanoma skin cancer; NHL, Non-Hodgkin lymphoma. Data source: Cancer Today | IARC, Globocan [1].

In 2022, lung cancer dominates the worldwide stage both in incidence and mortality, followed by breast and colorectum cancer. Even in European countries, lung

cancer is the most deadly disease, while breast cancer is still the most diagnosed one when considering both genders.

It is evident that mortality rates among patients diagnosed with lung cancer are significantly higher than other cancers. A significant correlation was observed between lung cancer mortality and the socioeconomic development of regions [6] [7]. Countries with lower levels of development exhibited higher prevalences of smoking, underdeveloped healthcare infrastructures, and a lower level of public awareness concerning the risks associated with lung cancer. This is probably imputable to the lack of observable symptoms in the early stages of the disease. Moreover, the presence of a nodule is highly correlated to the probability of having metastasis in other parts of the body [8]. The primary reason for that should be that the lungs are designed for respiration, including the oxygenation of blood cells (erythrocytes) in blood vessels. This means that the presence of one or more nodules in the lungs may be indicative of a high probability of cancer cells spreading throughout the body by means of the circulatory system. For this reason, one of the most important prognostic factors to consider is to highlight the presence of lympho-vascular invasion in the histopathological exam.

The incidence of skin cancer has steadily risen in recent decades. As a matter of fact, Non-Melanoma Skin Cancer (NMSC), as in Figure 2.1, represents the fifth most frequently diagnosed cancer in 2022, even if basal cell carcinoma has been excluded from this statistics.

On the contrary, also from the graph in Figure 2.1, in 2022 melanoma occupies the eighth place in term of incidence with higher rate of mortality than other skin cancers. Even if accounting for only 5% of all skin cancer [9], melanoma is responsible for the majority of deaths in this category due its aggressive nature and tendency to spread to other organs becoming metastatic [10].

It should be noted that non-melanoma skin cancers are often unrepresented in health registers due to the practice of treating them in primary care [11]. For this reason, such type of cancers are often excluded from statistics or classified as “other cancers”.

2.2 Melanoma Skin Cancers

Skin cancer is an increasingly common and concerning medical condition resulting from the uncontrolled growth of skin cells [12]. While excessive sunbathing as well as artificial UV lamps are the most important risk factors for the development of the disease, aging and familiarity can also play an important prognostic role.

Due to their different characteristics, behaviors, and treatments, cutaneous cancers can be classified into two main groups: non-melanoma and melanoma. The first category includes basal cell carcinoma and squamous cell carcinoma, which are the most frequently occurring types of skin cancer, while melanoma is less common, although more serious.

2.2.1 Melanoma Pathogenesis

Cutaneous melanoma develops from malignant transformations of pigment-producing melanocytes in the basal layer of the skin epidermis. Melanoma arises when DNA is damaged, as a result of ultraviolet radiation exposure. This induces mutations in melanocytes, leading to uncontrolled cell growth. Melanoma might manifest as a discrete lesion on the skin or as a change in the appearance of an existing nevus. In some cases, it could also originate in the eyes or mucous membranes.

The skin phenotype plays an important role with higher risk for fair-skinned individuals: in 2006 American Caucasians accounted for 70% of melanoma cases [13], while black population had an increased mortality as a result of late detection and a different biology [14].

The evolution of cutaneous melanoma is contingent upon the thickness of the melanoma at the time of diagnosis and removal. The greater the depth of infiltration, the greater the risk of mortality for the patient. Consequently, the most effective strategy for reducing mortality from melanoma is early diagnosis.

2.2.2 Melanoma Diagnosis

First melanoma signs are often associated with a change in an existing mole and the development of a new pigmented or unusual-looking growth on the skin.

Mole inspections consist of observing nevi using a dermatoscope, which is a special instrument equipped with an epiluminescence microscope. The procedure is painless and allows the doctor to view details of the inner appearance of a nevus that are invisible to the naked eye. This enables the early detection of melanoma, which would otherwise be undetected.

The preliminary diagnosis of melanoma is based on the revised ABCDE rule of pigmented lesions (Asymmetry, irregular Border, change in Color, Diameter, Evolution): when one or more of the features listed above are identified in a mole, biopsy material is removed and analyzed in the laboratory.

2.2.3 Prognostic Factors

Many prognostic parameters are considered when analyzing excised tissue through histopathology. These include mitotic rate, lymphovascular invasion, neurotropism, and tumor-infiltrating lymphocytes [15]. The most important prognostic indicators are the tumor thickness - also known as Breslow Thickness - and the presence of ulceration overlying the tumor [16]. Even if the current diagnostic workflow has been mostly specialized in producing robust and accurate results, the correct interpretation of malignant lesions remains one of the greatest challenges for pathologists [17]. For such reasons, training and expertise are fundamental factors in overcoming the lack of objective and reproducible diagnostic criteria, especially when considering melanoma diagnosis [18].

2.2.3.1 Tumor Depth (Breslow Thickness)

The Breslow thickness, a measurement of the depth of invasion of melanoma cells into the skin, is employed by pathologists to assess the likelihood of metastasis and overall survival [15]. Table 2.1 and Figure 2.2 show a simplified representation of the correlation between TNM staging and tumor depth, according to the eighth edition of American Joint Committee on Cancer (AJCC) on melanoma staging [19] [20].

T Category	Thickness
Tis	N/A
T0	N/A
T1	$\leq$ 1.0 mm
T2	1.0 - 2.0 mm
T3	2.0 - 4.0 mm
T4	$>$ 4.0 mm

Table 2.1. Simplified T category (primary tumor) criteria representation for melanoma [19] [20]. Legend: Tis, melanoma in situ; T0, no evidence of primary tumor; N/A, not applicable.

A lesion thicker than 1 mm is considered as invasive melanoma and it is associated with higher risk of metastasis. Pathologists might face some criticality when determining the deepest dermal cell to measure tumor thickness.

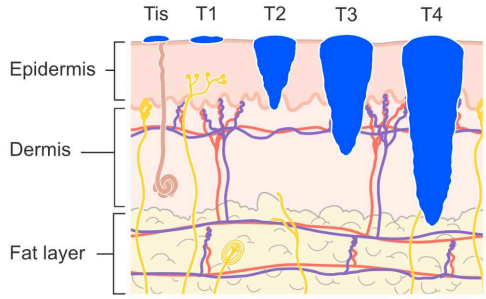

Figure 2.2. Illustration of tumor staging system based on the thickness of the melanoma and the extent of invasion into surrounding skin layers, as reported in Table 2.1. Image taken from [21].

2.2.3.2 Ulceration

Ulcerated melanoma, which indicates the loss of the epidermal layer, is characterized by an aggressive tumor behaviour and increased risk of metastasis [22] [23]. Some research has underlined the correlation between extensively ulcerated melanoma and

poorer prognosis than minimally ulcerated melanoma [23] [24] [25]. It is also important for pathologists to distinguish between a true ulceration and residual blood resulting from sectioning or other artefactual disruption.

Based on these specific criteria, differentiation between T1a (<1mm and no ulceration) and T1b (>1mm or presence of ulceration) subcategories in Tumor Node Metastasis (TNM) staging of melanoma is a critical phase to determine the refining prognostic stratification and treatment decisions [26] [27] [28] [29].

In particular, even if the melanoma has a Breslow thickness below 1 mm but presents an ulceration, the consideration of sentinel lymph node biopsy is needed to understand if tumor cells have invaded the lymph node leading to an increased risk of metastasis.

2.2.4 Melanoma Types

As melanoma may present in a variety of shapes, patterns, and stages of invasiveness, the correct identification of these features can have a significant impact on a patient's prospect of survival [30] [31] [15] [32]. The appearance and growth of melanoma skin cancers will differ depending on the morphological type.

2.2.4.1 Melanoma In Situ

Melanoma In Situ (Mis) is a malignant tumor confined to the outer layer of the skin (the epidermis) and not the second layer of the skin (the dermis). Also referred to as stage 0 melanoma, melanoma in situ has no sign of invasion of surrounding tissues, lymph nodes, or distant sites. In the TNM system, this aspect is considered Tis - Tumor in situ, N0 - no spread to the lymph nodes, and M0 - no sign of metastasis.

Patients with Stage 0 melanoma are considered at very low risk for local recurrence or for regional and distant metastases. For this reason, the standard treatment of melanoma in situ is surgery. The removal of any remaining cancer from the biopsy site is called excision.

2.2.4.2 Superficial Spreading Melanoma

Superficial Spreading Melanoma (SSM) is the most common histological pattern among all invasive melanoma variants. The tendency of spreading horizontally rather than vertically into the dermal tissue characterizes such tumor.

SSM is characterized by the presence of atypical melanocytes that have passed the epidermal-dermal junction, slowly invading the dermis. Architectural changes, such as atypical melanocytes, are visible within epidermis. These melanocytes exhibit patterns of irregularities in both nuclear shape and size, also known as pleomorphism, and irregular distribution.

Due to the gradual invasion and advance into the dermis of the disease, pagetoid infiltration of the epidermis by melanocytes is frequently observable in superficial

spreading melanoma. Pagetoid cells are often larger and more atypical than normal cells, with a tendency to diffuse along the basal layer of the epidermis.

2.2.4.3 Nodular Malignant Melanoma

Nodular Malignant Melanoma (NMM) is the most aggressive form of melanoma. Compared to other melanoma subtypes, it tends to grow more rapidly in thickness (vertical growth phase) than in diameter (radial growth phase).

Nodular melanoma appears as a compact mass of dysplastic tumor cells with upward epidermal invasion. Its tumor cells are often characterized by a high mitotic activity, which indicates a high level of cellular proliferation seeking for expansion. The tendency of highly atypical melanocytes to conglomerate into clusters or nests strongly promotes the vertical growth pattern, while keeping minimal adjacent epidermal spread. As a result, the tumor mass appears distinct and confined in its shell with respect to other skin layers (e.g. epidermis and dermis).

2.3 Lung Cancers

Lung cancer is one of the most prevalent and lethal forms of cancer, arising from abnormal cellular proliferation in lung tissues, predominantly in the lining of air passage. The early stages may be asymptomatic, which presents a challenge in terms of early detection. Despite the advances in targeted therapies and immunotherapy, the prognosis remains contingent on the stage of diagnosis, with later stages often exhibiting lower survival rates.

2.3.1 Etiology And Pathogenesis

Lung cancer etiology encompasses various factors that contribute to the initiation and development of the disease. The most significant etiological factor is tobacco smoke, responsible for approximately 85% of lung cancers [33]. Carcinogens in tobacco smoke cause DNA damage and mutations in lung cells [34–36]. Occupational exposure to carcinogens, including asbestos, radon gas, arsenic, and certain chemicals, has been identified as a significant risk factor for developing lung cancer [37]. Furthermore, environmental factors, including air pollution and second-hand smoke, have been identified as contributing factors to the incidence of the disease [38]. Additionally, certain viral infections and chronic lung diseases have been linked to an increased risk of lung cancer.

The pathogenesis of lung cancer is the result of a complex interplay between genetic and environmental factors, leading to the transformation of normal lung cells into malignant ones. This process is initiated by the exposure of lung tissues to carcinogens, which cause genetic mutations in the epithelial cells that line the airways, thereby promoting uncontrolled cell proliferation. Additionally, genetic predisposition

plays a role, while chronic inflammation and oxidative stress contribute to further genetic damage and cellular changes.

As mutated cells proliferate, they accumulate additional genetic alterations, which leads to increased tumor heterogeneity and the ability to invade surrounding tissues and metastasize to distant organs. The tumor microenvironment, including interactions with immune cells and the extracellular matrix, also plays a crucial role in tumor progression and resistance to therapy.

2.3.2 Screening And Diagnosis

In the case of suspected lung cancer, a series of tests will be prescribed by a qualified health professional, including imaging techniques. Detecting lung cancer nodules involves a multi-step process that typically begins with imaging techniques such as chest X-rays or more advanced methods like Computed Tomography (CT) scans. CT scans, in particular, are highly effective in identifying small nodules, providing detailed cross-sectional images of the lungs. If a suspicious nodule is detected, further evaluation may involve Positron Emission Tomography (PET) scans to assess metabolic activity, which can help differentiate between benign and malignant nodules. However, imaging alone cannot confirm a cancer diagnosis, so a biopsy is often required.

This can be done through various methods, including bronchoscopy, mediastinoscopy, needle biopsy, or, in some cases, surgical biopsy, where a sample of the tissue is extracted for microscopic examination. The biopsy helps determine whether the nodule is cancerous, as well as the type and stage of lung cancer, enabling doctors to develop a targeted treatment plan.

The TNM system is used to stage most cancers and describes the anatomic spread of a tumor. In it, the T descriptor describes the extent of the primary tumor, the N descriptor reflects the extent of regional lymph node involvement, and the M descriptor defines spread to distant sites. The current staging system for lung cancer is developed by the International Association for the Study of Lung Cancer (IASLC), whose eights edition of IASLC for T category of TNM staging is reported in Table 2.2 [39] [40].

T Category	**Tumor Size**
Tis	N/A
T0	N/A
T1	$\leq$ 3.0 cm surrounded by visceral pleura
T2	3.0 - 5.0 cm
T3	$>$ 7.0 cm
T4	any size with invasion of other organ

Table 2.2. Simplified T category (primary tumor) criteria representation for lung cancers [39] [40]. Legend: Tis, cancer in situ; T0, no evidence of primary tumor; N/A, not applicable.

In the majority of cases, the T descriptor is determined by the tumor size as measured by the greatest dimension on CT imaging. It is imperative that surgical excised tumors are measured prior to fixation in order to determine the greatest diameter, as the process of fixation in formalin has been observed to cause shrinkage of up to 20% in tumor size [41]. A diagnosis of stage 1, or T1, indicates the earliest and most localised form of the disease. As the tumor grows in size or spreads beyond the lungs, the stage increases in number. A stage 4 lung cancer has metastasised to other areas of the body.

2.3.3 Prognostic Factors

Prognostic factors in lung cancers are essential for predicting outcomes and guiding treatment. Tumor size, location, and lymph node involvement further influence outcomes, with larger tumors and extensive lymph node involvement indicating a poorer prognosis [42].

Lung cancers can be classified histologically based on its cellular characteristics. Histological prognostic factors to consider are many: tumor grade, histological subtype, and the infiltration at the tumor front are just some of them.

2.3.3.1 Tumor Grade

The histological grading system typically ranges from well-differentiated (G1) to poorly differentiated (G3 or G4), based on the degree of abnormality observed in the cancer cells under a microscope, as reported in Table 2.3.

Tumor Grade	**Cancer Cells Description**
G1	Well-differentiated
G2	Moderately differentiated
G3	Poorly differentiated
G4	Undifferentiated

Table 2.3. Histological grading of invasive lung cancers [43] [1].

Addressing the correct histological subtype and assessing the correct grade can vary prognosis and treatment modalities, and complete surgical resection in early stages are crucial for long-term survival. While grade G1 cancer cells resemble normal lung cells and grow slowly, those of grade G2 are moderately differentiated and display a greater degree of variation compared to normal lung cells, exhibiting a moderate growth rate. In contrast, grade G3 cancer cells are poorly differentiated and exhibit a high level of aggressiveness, with a tendency to grow and spread rapidly. Grade G4 cancer cells display a high degree of abnormality, making it challenging to determine their origin. Such tumors are the most aggressive forms of lung cancer and therefore require the most urgent attention.

2.3.3.2 Pleural Invasion

Pleural invasion is the presence of the tumor at the surface of the visceral pleura. This has been associated with a poor prognosis and higher recurrence rates, according to [44]. Several studies demonstrated that there are significant survival difference in patients that presents the invasion of the visceral pleural elastica [45] [46].

The classification of the pleural invasion is based on the criteria of Hammar [47], for which the tumor invasion can be classified in four stages as reported in Table 2.4 and Figure 2.3.

Tumor Invasion	Types of Pleural Invasion
Pl0	No invasion
Pl1	Invasion through the elastic layer of visceral pleura
Pl2	Tumor at the surface of visceral pleura without involvement of adjacent structures
Pl3	Tumor invasion into parietal pleura

Table 2.4. Histological classification of pleural invasion in lung cancers. [47]

Tumors of any size with the invasion of the visceral pleural, such as Pl1 and Pl2, are classified as T2, while tumors with parietal pleural invasion (Pl3) are classified as T3, unless other factors result in a higher designation [48].

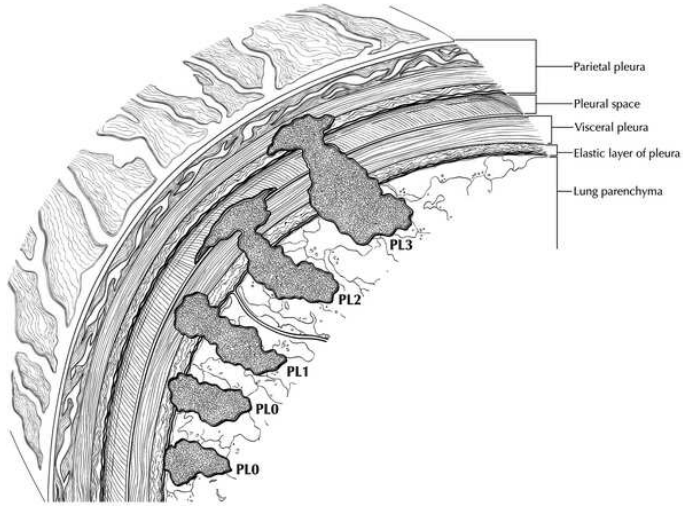

Figure 2.3. Illustration of distinct stages of pleural invasion as reported in Table 2.4. Image taken from [49].

2.3.3.3 Spread Through Air Spaces

Spread Through Air Spaces (STAS) represents the presence of tumor cells within the alveolar spaces, which are remote from the primary tumor. This indicates a form of microscopic spread, and its prognostic impact is related to an increased likelihood of recurrence and survival rates [50–52]. As indicated by the WHO [1], the presence of STAS has the potential to influence the surgical approach, which may result in the implementation of a more extensive resection or the consideration of adjuvant therapies.

2.3.3.4 Lympho-Vascular Invasion

Lympho-Vascular Invasion (LVI) is defined as the presence of tumor cells or emboli within the lumen of lymphatic or blood vessels. It has been identified as an adverse prognostic factor for a number of solid tumors [53, 54]. In lung cancers, numerous studies have demonstrated that LVI is also a poor prognostic factor for recurrence-free and overall survival in non-small cell lung cancers [55–59]. Furthermore, LVI is associated with an increased risk of regional lymph node involvement and indicates a poorer prognosis due to an increased likelihood of metastasis [60].

2.3.4 Lung Cancers Subtypes

Lung cancers can be classified into two main histological subtypes: Small Cell Lung Cancer, which accounts for approximately 15 % of lung cancer cases, and Non-Small Cell Lung Cancer, which comprises about 85 % of all cases [61]. The hierarchical taxonomy is presented in Figure 2.4.

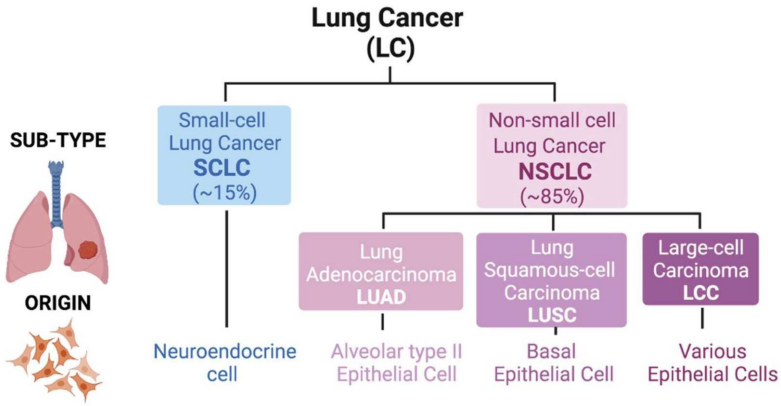

Figure 2.4. Graphical representation of the classification of lung cancers. Image taken from [62].

2.3.4.1 Small Cell Lung Cancers

In Small Cell Lung Cancer (SCLC), the tumor develops from neuroendocrine cells as a result of the malfunction of two crucial genes, namely RB and TP53 [62]. The disease is typified by the presence of small cells that exhibit a propensity for rapid growth, which in turn gives rise to the formation of large tumors. SCLC is typically more aggressive than NSCLC and often exhibits a propensity for rapid metastasis to other parts of the body [63].

2.3.4.2 Non-Small Cell Lung Cancers

In Non-Small Cell Lung Cancer (NSCLC), the tumor has its origin in lung epithelia as a result of specific genetic alterations [64]. NSCLC is further classified into three principal categories: Adenocarcinoma (Adk), Squamous Cell Carcinoma (SqCC), and Large Cell Carcinoma. Adenocarcinoma is the most common type, especially among non-smokers [65]. It originates in the mucus-secreting glands or alveoli and tends to occur in the outer regions of the lung. Squamous cell carcinoma originates in the squamous cells that line the airways and is most commonly observed in the central region of the lungs [66]. A history of smoking is frequently linked to the development of this form of cancer [67, 68]. Large cell carcinoma can manifest in any portion of the lung and is distinguished by the presence of large, atypical cells [69]. It exhibits rapid growth and metastatic potential.

The aim of this chapter is to provide a thorough fundamental understanding of the general aspects of cancer pathology, with a specific focus on the two cancers examined in this thesis: melanoma and non-small cell lung cancer. The subsequent chapter will address the imaging techniques employed in this study, including conventional histology and X-ray phase-contrast tomography, offering an in-depth introduction to the concept of X-ray Virtual Histology.

CHAPTER 3

Advanced Imaging Techniques

The principal concept of cancer pathology has been grasped and the basic forms of cancer to be treated in this thesis have been established in the previous chapter. This chapter presents the imaging techniques employed for their analysis.

3.1 Histopathology

Histopathology is the medical discipline that studies signs and characteristics of human disease processes in biological tissue. The histopathological examination represents the gold standard methodology in clinical routine as it produces accurate and robust results ready to be interpreted by pathologists. The two-dimensional information obtained with histopathology relates to the sectioned cutting plane. While it is possible to produce three-dimensional histological volumes by serial cutting, this technique presents limitations related to the representative nature of the 2D histological section and the mechanical deformation undergone in the execution of the cut.

3.1.1 Tissue Preparation For The Histological Exam

The histological procedure involves several steps, from the excision of the tissue to the visualization of thin sections positioned onto glass slides, as illustrated in Figure 3.1.

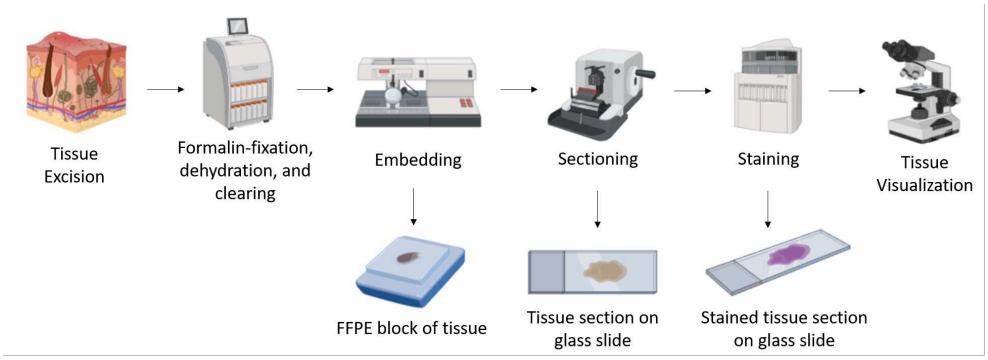

Figure 3.1. Clinical histopathological workflow to examine tissues for diagnostic purposes.

Tissue Excision The suspected pathological tissue is excised by biopsy or resection. If an internal suspected mass is inaccessible, an imaging exam (e.g., ultrasound, CT, Magnetic Resonance Imaging (MRI)), enables precise location of the tumor, might be ordered before the performing of the biopsy. After the surgery, the biopsy is sent to the pathological laboratory.

Formalin-Fixation To preserve the tissue from degradation, the excision is fixed in a solution of formaldehyde gas dissolved in water, commonly referred to as formalin. This process takes the name of formalin-fixation, which prevents the denaturation of proteins, and the degradation of cellular structures by means of post-mortem autolysis.

Dehydration And clearing After formalin fixation, tissues are typically dehydrated to remove water and replace it with a solvent that is miscible with both water and paraffin. This is usually done through a series of alcohol baths of increasing concentrations (e.g., 70%, 80%, 95%, 100% ethanol). Dehydration helps to prepare the tissue for infiltration with paraffin, since it is not miscible with water. Following dehydration, tissues are cleared to remove the alcohol and any remaining water. This step is essential to ensure proper infiltration of the tissue with molten paraffin wax.

Embedding The tissue is then infiltrated with molten paraffin wax, which replaces the clearing agent. The goal is to impregnate the tissue with paraffin wax, ensuring that it is fully embedded and supported during sectioning. The tissue is also oriented appropriately within the mold to ensure optimal sectioning. After embedding, the paraffin wax is allowed to solidify, forming a solid block.

Sectioning Thin slices of tissue are sectioned using a microtome, an instrument designed to produce tissue section of few microns (around 4-5 µm). These delicate tissues, that are mounted onto glass slides, may undergo further processing steps, such as deparaffinization and rehydration, to prepare them for staining.

Staining Depending on the specific cellular components or structures to visualize, the prepared tissue sections are then stained using various histological stains. The most used is the Hematoxylin and Eosin (H&E) staining, which is widely utilized to visualize tissue morphology and to aid in the diagnosis of various diseases. While haematoxylin selectively stains with purple acidic structures in tissues, such as cell nuclei and some cytoplasmic components, eosin selectively stains with pink coloration basic structures in tissues, such as cytoplasm and extracellular matrix. Once the tissue sections are mounted on glass slides, they are ready for microscopic examination.

3.1.2 Diagnosis Via Histopathological Exam

The stained tissue sections are examined under a light microscope allowing pathologists and researchers to observe tissue morphology, cellular details, and pathological changes. The pathologist interprets the cellular reaction to the staining procedure combined with the microarchitecture of the tissue. The organization of tissues and organs is observed at a microscopic and sub-microscopic level to provide precise information regarding the classification, diagnosis, prognosis, and treatment therapy.

Most hospitals are now equipping their pathology laboratories with advanced scanners, which use the Whole Slide Imaging (WSI) technique, to create digital archives that are accessible at any time. Furthermore, this technology provides the opportunity of digitally convert the entire tissues on glass slides into high-resolution virtual slides. Thanks to their high-magnification dynamic, zoomable WSI enables the migration of the diagnostic specimen from the microscope to the computer screen.

3.1.3 Computational Pathology

In the last few years, computational pathology has proven instrumental in decision making during the histopathological diagnosis [70]. It can be considered as the "omics" or "big-data" approach applied to pathology, where multiple sources of patient information, including pathology image data and meta-data, are combined to extract patterns and analyze features. The most employed subset of this field is related to WSI. Due to the high complexity of such data, the extraction of information from digitized pathology images is typically performed using AI methods, such as deep learning.

The use of deep learning algorithms could improve sensitivity with equal specificity, while requiring significantly less time for diagnostics [71]. An ideal decision support tool would incorporate such algorithms into a user-friendly system, aiding clinicians in making the best treatment decisions, while avoiding information overload and decision paralysis. In fact, as the role of the pathologist is essential in every stage of the clinical trial, personal experience and knowledge play a key factor in the diagnostics and prognostics outcomes [72]. On the contrary, deep learning is capable of identifying specific features in an automated way, unveiling hidden details that could simplify procedural workflow, while at the same time supporting the generation of quantitative measurements that would otherwise be unfeasible through manual means [73].

3.1.4 Limitations Of Conventional Histology

As all measurement tools, conventional histology has some limitations. First, the laborious process of tissue preparation may require days to produce results. Second, the presence of artifacts can be considerable due to the numerous stages of the histological protocol. Finally, conventional histology still remains a bi-dimensional approach

which might be unable to appreciate the expansion and arrangement of elements of interest in the surrounding volume.

3.1.4.1 Two-Dimensional Observations

The histological slide provides a single two-dimensional view of the specimen, which precludes the consideration of neighboring areas. To overcome this aspect, the mounting of several serial sections on the same slide is frequently employed in order to facilitate the visualization of more proximal areas of the tumor under examination. The specialist pathologist employs an abstraction process to hypothesize the probable spatial spread of the tissue or tumor.

In some cases, numerous serial sectioning can be employed for a three-dimensional evaluation of the sample [74]. However, as previously stated, this approach is time-consuming and prone to artifacts when preparing and merging different sections into a three-dimensional dataset. The presence of mounting or cutting artifacts can easily compromise the integrity of the dataset. Furthermore, the destruction of the sample during the histological procedure can affect reproducibility in case of missing information.

3.1.4.2 Artifacts Related To Histological Process

Many types of artifacts can occur during the production of histological results. In some cases, they can lead to a misinterpretation of some pathological aspects. In others, they can even lead to complete uselessness of the sample. As histology involves the sample destruction to have an internal observation, it is important to limit procedural artifacts or, at least, to be able to recognize and classify them. For example, sectioning can produce scores and tearing sections in hard tissues, such as bone or cartilage or when calcifications are present, while the displacement of tissue components mainly happens in soft tissues. Moreover, an unsharp knife can produce compression artifacts and can contaminate the produced section with floating pieces of tissue not belonging to it [75]. One of the most occurring mounting artifacts is the folding of tissues, which could cause limited visibility of the overlapping tissue [76]. Finally, an improper dose of staining could make cellular differentiation difficult, and thus the diagnosis.

3.1.4.3 Artifacts In Digital Pathology

In the context of digital pathology, the term “artifact” is used to describe distortions or inaccuracies that may be present in tissue images, which have the potential to impact the accuracy of diagnosis and analysis. Such artifacts may be the result of factors inherent to the preparation of the slides or to the scanning process itself (e.g. image blurring, compression artifacts, or uneven lighting). These artifacts have the potential to obscure critical cellular details, which could result in misinterpretations

by pathologists or affect the performance of image analysis algorithms. Nevertheless, some research is developing algorithms to identify and minimize these artifacts, thereby ensuring the generation of high-quality digital images [77, 78].

As stated so far, the histological exam is a powerful tool without its withdraws. This leaves an open door for complimentary support. One of them being X-ray Phase-Contrast Tomography, which will be presented in the next section.

3.2 X-ray Phase-Contrast Micro-Tomography

This section introduces the concept of Computed Tomography, which is then extended to its high-resolution version, termed Computed micro-Tomography (Micro-CT). To delve into all its applications, this section will briefly discuss the principle of interaction of X-rays with matter, the concept of Propagation-Based Imaging (PBI), and briefly describe the synchrotron and the laboratory facilities where this technique is employed.

3.2.1 Computed Tomography

CT refers to a diagnostic imaging technique widely used in the clinical context. A rotating gantry holds the X-ray source and detector, and the patient lies down on a bed which can be moved to select which part of the body to image. Such combination of X-ray and computed technologies facilitates the production of internal sections and 3D images of the body scanned.

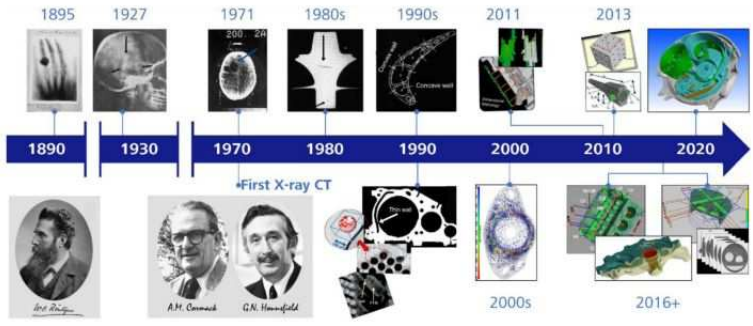

Figure 3.2. Improvement and development of X-ray technologies through years, from the first radiography to non-destructive measurements for industrial application, passing through the invention of the first tomographer. Image taken from [79].

The fundamental concept of CT was to leverage the physical information collected by two-dimensional radiographies at different angles. In the clinical context, two-dimensional X-ray imaging is a widely employed technique for the investigation

of bone and thoracic pathologies, as well as for angiographies. As a single two-dimensional observation, the radiographic image is unable to represent the three-dimensionality of the object imaged, while representing the most absorbing elements impressed by a single exposure to X-rays. By acquiring projection images from numerous perspectives around the sample, it is possible to subsequently reconstruct the object into a three-dimensional (3D) image. By combining the mathematical principle of the Radon transform with the physical information of the projectional radiography, it is possible to solve a n-dimension problem by its n-1 equations.

The first prototype, named computerized axial tomography (CAT), was implemented by Godfrey Hounsfield and Cormack in the 1970's. From its inception, the potential of this system was evident, and its evolution into a non-destructive evaluation and dimensional measurement tool has also been embraced by the industrial sector, as evidenced in Figure 3.2.

3.2.2 X-ray Micro-Tomography

X-ray micro-Tomography, also referred to as X-ray micro-Computed Tomography or micro-CT, is often employed in the non-clinical context where the source and the detector are kept stationary while the sample is rotated between frames. It is similar to conventional CT, but offers much finer spatial resolution in the micrometer range. This type of setup allows to modulate the magnification, and thus the effective pixel size, as well as the effect of the phase contrast by playing on the distances of the object from the source and detector. The geometric magnification M of a micro-CT system is defined as in Equation 3.1:

$$M = \frac{SSD + SDD}{SSD} \tag{3.1}$$

where SSD is the source-to-sample distance, and SDD is the source-to-detector distance. The magnification defines the effective pixel size of the radiography (p_e), which can be as expressed in Equation 3.2:

$$p_e = \frac{p_d}{M} \tag{3.2}$$

in which p_d is the physical size of the pixel of the detector.

3.2.2.1 X-ray Beam Geometries Configurations

There are several common beam geometry configurations for X-ray micro-CT scanners, depending on the type of X-ray source, as illustrated in Figure 3.3.

In cone-beam scanning, the X-ray beam is not collimated and diverges from a point source to form a cone-shaped beam that illuminates the sample. This geometry allows for efficient imaging by capturing the entire volume of the sample, or a considerable thickness of it, in a single rotation, with the planar detector positioned to record a

two-dimensional projection of the transmitted X-rays. Then, data collected by the planar detector are reconstructed into images using a cone-beam algorithm. While it offers high resolution and flexibility, cone beam geometry can introduce geometric distortions, that need to be addressed during the reconstruction step. Cone beam systems are widely used in laboratory setups due to their compactness and efficient imaging capabilities,

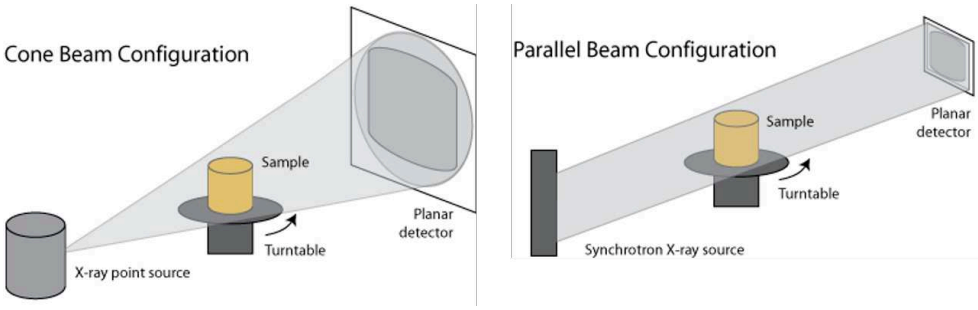

Figure 3.3. Comparison of cone beam and parallel beam configurations for X-ray Imaging. On the left, the cone beam configuration uses an X-ray point source, creating diverging rays that project onto a planar detector. On the right, the parallel beam one employs a synchrotron X-ray source to produce parallel rays, which are captured by a planar detector. In both cases, the sample rotates on a turntable during imaging. Image taken from [80].

The parallel beam configuration is typically available in synchrotron facilities, in which the synchrotron radiation produced is a broad spectrum of X-ray wavelengths, commonly referred to as a "white beam". Such beam is highly collimated, resulting in a nearly parallel geometry that eliminates divergence and enables superior resolution compared to laboratory systems. Furthermore, given the high intensity of synchrotron radiation, the acquisition of data is often expedited. In this case, volumetric data are acquired and there is no distortion, due to the elevated distance between the original source (the bending magnet) and the sample in the experimental station that creates a geometrical magnification of 1 ($M \approx 1$). However, the object size is limited by the width of the X-ray beam, which typically is in a range of few centimeters. These physical properties make synchrotron-based micro-CT an indispensable tool for achieving high precision and clarity in three-dimensional imaging.

In summary, X-ray micro-Tomography offers detailed internal examination without damaging the sample for non-destructive testing and quantitative measurement. The adaptability of this imaging technique makes it a frequently employed tool in biomedical research, geology, and materials science, rather than solely within the context of clinical applications. However, conventional micro-CT imaging cannot appreciate fine structures in low-density or weakly absorbing material, so phase-contrast micro-CT techniques are often employed to recover important information that could not be resolved by conventional micro-CT.

3.2.3 X-ray Phase-Contrast Imaging

X-ray Phase-Contrast Tomography (XPCT) has several advantages over conventional absorption-based micro-CT. First, the increased contrast for materials with similar X-ray absorption properties makes it useful for imaging soft tissues, biological samples, and materials with low absorption contrast [81]. Secondly, it improves spatial resolution, as it can achieve high spatial resolution, allowing for the visualization of fine structures within the sample. Then, phase-contrast data can provide quantitative information about the refractive index of materials, which can be useful for studying material properties and biological specimens. Finally, it can sometimes be performed with lower X-ray doses compared to absorption-based techniques, reducing the risk of radiation damage to sensitive samples.

XPCT is an important tool in various scientific fields, including biology, materials science, and geology, where it enables the study of internal structures and processes with unprecedented detail and contrast.

3.2.3.1 Physical Principles Of X-ray Phase-Contrast

When transmitted through materials, the intensity of X-rays changes depending on the different absorption coefficients of materials allowing the observation of the internal features of objects using non-invasive X-ray imaging. However, the image created according to the adsorption principle exhibits poor contrast when dealing with low-Z materials. X-ray phase-contrast imaging is able to retrieve information about the phase composition of such tissues (e.g., biological specimens), providing higher sensitivity and contrast than absorption imaging. Moreover, higher contrast makes the different composition of an object more distinguishable by enhancing the edges and boundaries within the sample. Here, the following principles of X-ray Phase-Contrast imaging.

Lambert-Beer Law In radiology and tomography, the Lambert-Beer law defines the reduction in intensity of the X-rays passing through an object. The attenuation of X-rays are proportional to the density and composition of the tissue, that is represented by the linear coefficient (μ) along the beam path in Equation 3.3:

$$I(x, y) = I_0 e^{-\int \mu(x,y,z)dz} \tag{3.3}$$

In tomography, the attenuation coefficient of tissues μ is used to obtain the internal, detailed cross-sectional images of the body by determining how much the X-ray beam is attenuated as it passes through the tissue.

The Refractive Index In X-ray phase-contrast imaging, an object can be described by its refractive index $n(E)$:

$$n(E) = 1 - \delta(E) + i\beta(E) \tag{3.4}$$

where δ is the decrement of the real part responsible for the phase shift, and β represents the imaginary part deputed for attenuation. The refractive index describes how much the speed of light (or X-rays) changes as it passes through a material. As a consequence, its parameters (δ and β) are dependent on the object's characteristics (e.g. electron density ρ_e, μ), and the energy of the X-ray wave (E), as reported in the next equations:

$$\delta(E) \propto \frac{\rho_e}{E^2} \qquad \beta(E) \propto \frac{\mu}{E} \tag{3.5}$$

The Phase-Shift When X-rays pass through the sample, they may undergo phase shifts due to variations in the refractive index of different materials within the sample, as represented in Figure 3.4.

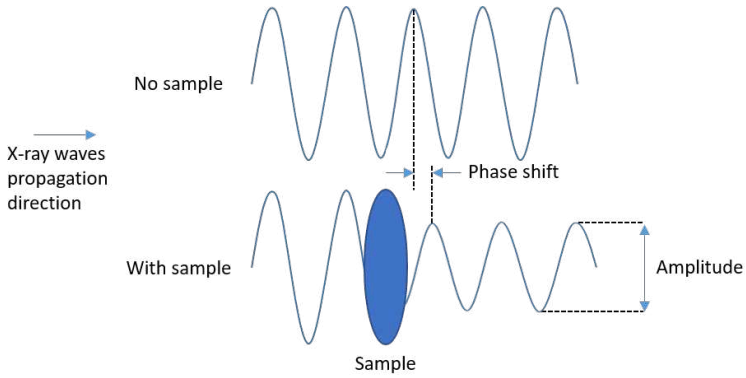

Figure 3.4. X-ray waves propagation with and without the sample. The plot illustrates both phase shift and amplitude reduction of the wave that is induced after propagating through the medium.

X-ray phase-contrast imaging exploits the phase shift induced by the object when the X-ray is trespassing such object. In the wave model, the interaction of X-rays with matter is described through the complex refractive index $n(x, y, z; E)$. When considering X-ray waves pass through an object, the object-modulated wave $\psi_{out}(x, y; E)$ is defined as in Equation 3.6:

$$\psi_{out}(x, y; E) = \psi_{in}(E) e^{-k \int 1-n(x,y,z;E)dz} \tag{3.6}$$

where $\psi_{in}(E)$ is the incoming plane X-ray wave, $e^{-k \int 1-n(x,y,z;E)dz}$ represents the complex transmission function through the object, and $k = 2\pi/\lambda$ is the wave number. By simply using Equation 3.4 into Equation 3.6, the object-modulated wave becomes:

$$\psi_{out}(x, y; E) = \psi_{in}(E) e^{-k \int \beta(x,y,z;E)dz} e^{-ik \int \delta(x,y,x;E)dz} \tag{3.7}$$

The Equation 3.7 is now described as a combination of three factors: the amplitude of the incoming wave (ψ_{in}), the amplitude modulation reduction due to the sample (-$a(x, y)$ of Equation 3.8), and the phase shift ($\phi(x, y)$ of Equation 3.9).

$$-a(x, y) = ik \int \beta(x, y, z)dz \tag{3.8}$$

$$\phi(x, y) = -k \int \delta(x, y, x)dz \tag{3.9}$$

In conclusion, the parameter δ is responsible for the phase shift that occurs when radiation passes through an object. As defined in Equation 3.5, this parameter refers to the object's electron density, which indicates that the phase shift is related to the density of the object.

3.2.4 X-ray Phase-Contrast Imaging Configurations

There are several methods to perform X-ray phase-contrast imaging, such as X-ray holography, gratings interferometer, edge-illumination, diffraction-enhanced imaging, and propagation-based imaging. In order to provide a concise overview of the techniques employed in this thesis, it is necessary to limit the description to those that were actually used in the experiments.

3.2.4.1 Propagation-Based Imaging

Propagation-based imaging (PBI) leverages the phase-contrast to produce high-contrast images. PBI setup is the simplest configuration to perform phase-contrast which needs nothing more than the X-ray source and a movable detector. Unlike for absorption-based imaging in Figure 3.5(a), PBI relies on the specific positioning of the sample relative to the source (R_1) and the detector (R_2) as represented in Figure 3.5(b).

Unlike traditional absorption-based imaging in which only the contribution of attenuation is considered, PBI projections contain both attenuation and phase information. As X-rays passes through different materials, the induced phase-shifts create inference patterns when the X-rays propagate beyond the object. By modulating the distance of the object and the source and detector as in Figure 3.6, such phase-shifts manifest as intensity variations, named fringes, on the detector.

The phase-contrast signal is pronounced in the presence of discontinuities in the object, such as at object boundaries, and is discernible as a series of strong white and black fringe pairs as in Figure 3.6. This phenomenon is known as edge enhancement.

Attenuation And Phase Detection In an optical model, the refraction could be described by a ray-tracing approach, thus meaning considering X-ray photons as particles instead of waves. In ray tracing, every local deviations of the wave vector is equivalent to deviations in the trajectory of photons (i.e. refraction). This implies

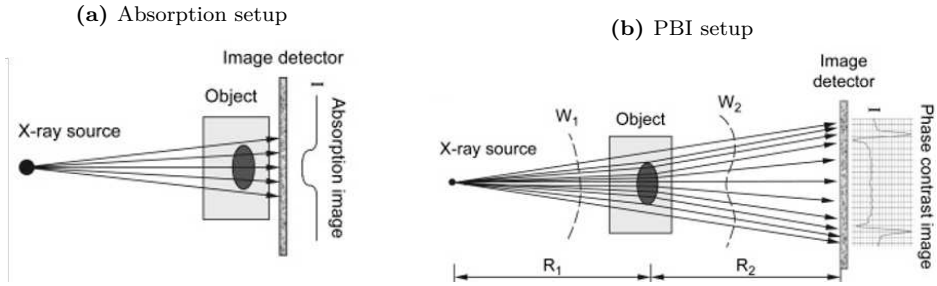

Figure 3.5. X-ray setup employing 3.5(a) the absorption mode and 3.5(b) the propagation-based mode. The impact of the two configurations is discernible in the profiles resulting from the sample's presence within the wave propagation, demonstrating on the left the phenomenon of attenuation and on the right the effects of interference patterns. Image adapted from [82].

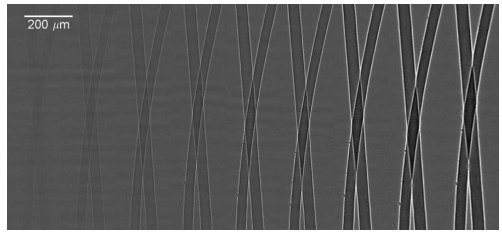

Figure 3.6. A sample of a pair of hair acquired at different sample-to-detector distances ranging from 20 to 1140 mm. The effect of phase-contrast signal becomes more evident as the distance increase. Image taken from [83].

that photons impacting on the object at the position $(x, y, z = 0)$ are refracted to the position $(x, y, z' = z_0)$ where the detector is placed (defined as "image plane" in Figure 3.7).

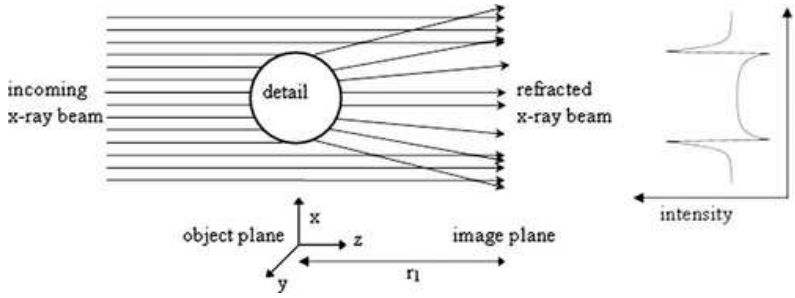

Figure 3.7. Graphical representation depicts the optical model illustrating the refraction of an X-ray beam due to the presence of an object and the subsequent generation of the characteristic intensity profile. Image taken from [84].

As highlighted by Figure 3.7, the shift of photons serves for the purpose of tracking the changes in X-ray detectable intensity as it progresses from the sample plane to the detector plane. As a result, the intensity reaching the image plane is indicative of the Laplacian of the phase shifts ($\nabla^2\phi(x,y)$) that have been introduced into the incident beam as a consequence of its passage through the object. This information is represented in Equation 3.10:

$$I(x,y,z=z_0) = I(x,y,z=0)\left(1-\frac{z_0}{k}\nabla^2\phi(x,y)\right) \tag{3.10}$$

where $I(x,y,z=z_0)$ and $I(x,y,z=0)$ are respectively the intensity measured at the image plane and at the object, and $\left(1-\frac{z_0}{k}\nabla^2\phi(x,y)\right)$ is the Jacobian of the coordinate transformation.

By applying the Lambert-Beer law of Equation 3.3 in Equation 3.10 and simplifying $I(x,y,z=z_0) = I(x,y)$ and $I(x,y,z=0) = I_0$), Equation 3.11 is obtained:

$$I(x,y) = I_0 e^{-\int \mu(x,y,z)dz}\left(1-\frac{z_0}{k}\nabla^2\phi(x,y)\right) \tag{3.11}$$

where the detected $I_0 e^{-\int \mu(x,y,z)dz}$ which represents the attenuation component, and $\left(1-\frac{z_0}{k}\nabla^2\phi(x,y)\right)$ the phase contribution. This shows that the detected image contains both the attenuation and the phase information. Moreover, the presence of the Laplacian operator modulating the intensity makes propagation-based imaging a double-differential phase-contrast imaging technique.

Homogeneous Transport-Intensity Equation The mostly used approximation to retrieve the projected phase component is the Homogeneous Transport-Intensity Equation (TIE-Hom) described in [85]. Assuming that the object is monomorphous, which means that is composed by a single material, the detected attenuation and phase intensities represented in Equations 3.8 and 3.9 can be solved as in Equations 3.12 and 3.13:

$$\int \mu(x,y,z)dz = 2k\beta t(x,y) \tag{3.12}$$

$$\int \delta(x,y,z) = \delta t(x,y) \tag{3.13}$$

As a result, the detected intensities in Equations 3.13 are functions of the projected thickness of the object ($t(x,y)$), which need to be retrieved. Then, δ and β components are known or, at least, they can be easily calculated since they are dependent on the material's characteristics (see Equation 3.5). By using Equations 3.12 and 3.13, Equation 3.11 becomes:

$$I(x,y) = I_0 e^{-2k\beta t(x,y)}\left(1-z_0\frac{\delta}{2k\beta}\nabla^2\right) \tag{3.14}$$

By inverting Equation 3.14 and using the Fourier Differentiation Theorem, the projected thickness $t(x,y)$ of the object can be retrieved as follows:

$$t(x,y) = -\frac{1}{2k\beta} log\left(\mathfrak{F}^{-1}\left(\frac{\mathfrak{F}(I(x,y)/I_0)}{1+z_0\frac{\delta}{2k\beta}(u^2+v^2)}\right)\right) \tag{3.15}$$

where $\mathfrak{F}$ is the two-dimensional forward Fourier transform, $\mathfrak{F}^{-1}$ is the backward Fourier operator, and u, v represent the Fourier conjugate coordinates of x, y. The Equation 3.15 represents the projected phase shift of the X-ray wavefront.

3.2.5 X-ray Phase-Contrast Tomography With A Synchrotron Source

Synchrotron sources are highly suitable for XPCT as they produce highly intense and focused beams of light or other radiations. Synchrotrons are invaluable in fields such as physics, chemistry, biology, and materials science due to their ability to reveal detailed insights that are otherwise inaccessible with conventional techniques.

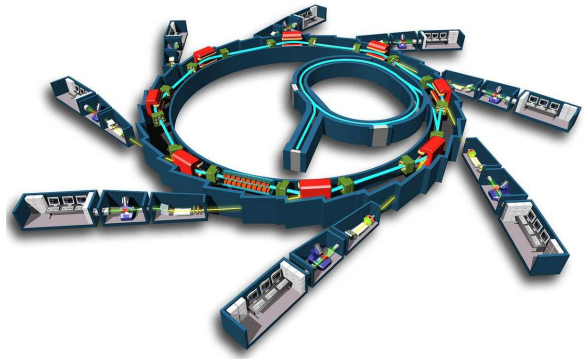

Figure 3.8. Schematic representation of a synchrotron radiation source. Electrons are accelerated to near-light speeds in a storage ring, producing highly collimated and intense X-ray beams as they are deflected by magnetic fields. These X-ray beams are directed toward experimental stations for imaging and analysis, enabling advanced techniques such as phase-contrast and high-resolution tomography. Image taken from [86].

As shown in Figure 3.8, the synchrotron works by accelerating charged particles, such as electrons, to nearly the speed of light within a circular path using electric fields for acceleration and magnetic fields for steering. In the storage ring, these high-speed electrons pass through undulators, wigglers, and bending magnets, and, when such high-speed electrons change directions, they emit energy in form of X-rays. The so-called synchrotron radiation is an intensely bright, highly tunable light, billions of times more luminous than conventional sources. Beamlines collect and transport this radiation coming from the bending magnet to the experimental stations, where this radiation is harnessed for a wide variety of applications, including studying the structure of materials, biological molecules, and chemical processes at atomic

and molecular levels, and investigation techniques, including spectroscopy, diffraction, absorption, scattering and imaging. In X-ray imaging, the resulting X-ray beam allows for precise detection of phase shifts that occur as the X-rays interact with the sample, as its highly collimated and coherent properties.

3.2.6 Physical And Mathematical Principles Of X-ray Tomography

X-ray Tomography combines physics principles like X-ray attenuation, and interaction with matter, alongside mathematical tools for image reconstruction, to produce detailed images of internal structures. It uses X-rays and their differential absorption to create detailed cross-sectional images of internal structures. Multiple images are taken from different angles, and mathematical algorithms like the Radon transform and Filtered Back Projection reconstruct 3D images from 2D projections. The Beer-Lambert law describes how X-ray intensity decreases due to attenuation, aiding in visualizing the internal structure.

3.2.6.1 From Projections To Slices

Tomography is the solution of an inverse problem which involves the Radon transform to define the attenuation profile of the object, the Fourier transformation to translate the spectral information into the Fourier space, and finally the Fourier Slice Theorem which inverts the object in the Fourier space into the real space.

Radon Transform The basic assumption of tomography is that an object can be internally studied by collecting a series of radiographies from different angles. The goal is to accurately retrieve the attenuation coefficients $\mu(x, y, z)$ of the sample, and thus reconstruct it. The Radon transform considers each radiography, also known as projection $p(\rho, \theta)$, as the summation of the attenuation profiles of the object scanned $f(x, y)$, providing information about its composition. Figure 3.9 and Equation 3.16 describe such concept:

$$p(\theta, \rho) = \int_{-\infty}^{+\infty} \int_{-\infty}^{+\infty} f(x, y)\delta(xcos(\theta) + ysen(\theta) - \rho)dxdy \tag{3.16}$$

Fourier Slice Theorem By considering multiple projections acquired over the sample rotation, multiple attenuation contributions are collected to compose the sinogram, which is a graphical representation of the intensity measurements at many different angles. Every vertical line of the sinogram can be used to compute the 1D Fourier transform, and then to compose the 2D Fourier domain in the Fourier space. The direct Fourier image shows the high frequencies in the center and the low frequencies with darker tones far away.

The Fourier slice theorem states that the Fourier transform of a projection $P(\omega, \theta)$, obtained by integrating the object along parallel lines, is equivalent to a slice of the

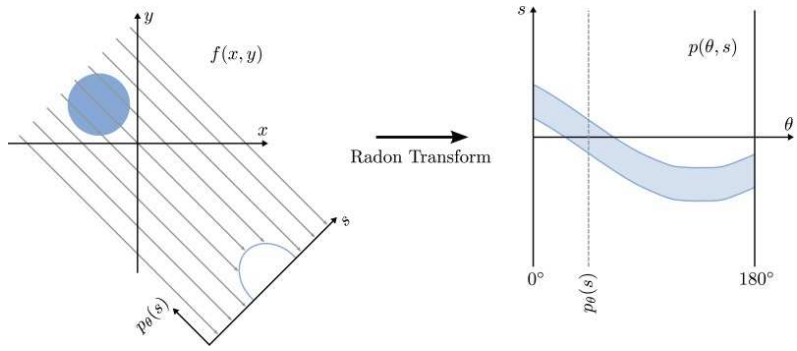

Figure 3.9. Visualization of the Radon Transform. On the left, the original 2D function f(x,y) is projected along parallel lines at a given angle θ, producing a set of line profiles. On the right, the result of the Radon Transform $p(\theta, s)$ is shown as a function of angle θ and distance $s = xcos(\theta) + ysen(\theta)$, where the curve represents the sinogram corresponding of the transformed data corresponding to the projections. Image taken from [87].

Fourier transform of the object taken through the origin. Equation 3.17 represents the definition of such property:

$$P(\omega, \theta) = \int_{-\infty}^{+\infty} p(\rho, \theta) e^{-j2\pi\omega\rho} d\rho \tag{3.17}$$

By substituting Equation 3.16 into Equation 3.17, the Fourier Slice Theorem is obtained, expressed as Equation 3.18:

$$P(\omega, \theta) = \int_{-\infty}^{+\infty} \int_{-\infty}^{+\infty} \int_{-\infty}^{+\infty} f(x, y)\delta(xcos(\theta) + ysen(\theta) - \rho) e^{-j2\pi\omega\rho} dxdyd\rho \tag{3.18}$$

Rearranging the order of integration, Equation 3.18 becomes:

$$P(\omega, \theta) = \int_{-\infty}^{+\infty} \int_{-\infty}^{+\infty} f(x, y) \left(\int_{-\infty}^{+\infty} \delta(xcos(\theta) + ysen(\theta) - \rho) e^{-j2\pi\omega\rho} d\rho \right) dxdy \tag{3.19}$$

By integrating over the delta function, the expression simplifies to as Equation 3.20:

$$P(\omega, \theta) = \int_{-\infty}^{+\infty} \int_{-\infty}^{+\infty} f(x, y) e^{-j2\pi(xcos(\theta)+ysen(\theta))\omega} dxdy \tag{3.20}$$

Backprojection The Fourier slice theorem, which establishes a relationship between the two-dimensional Fourier transform of an image and the one-dimensional

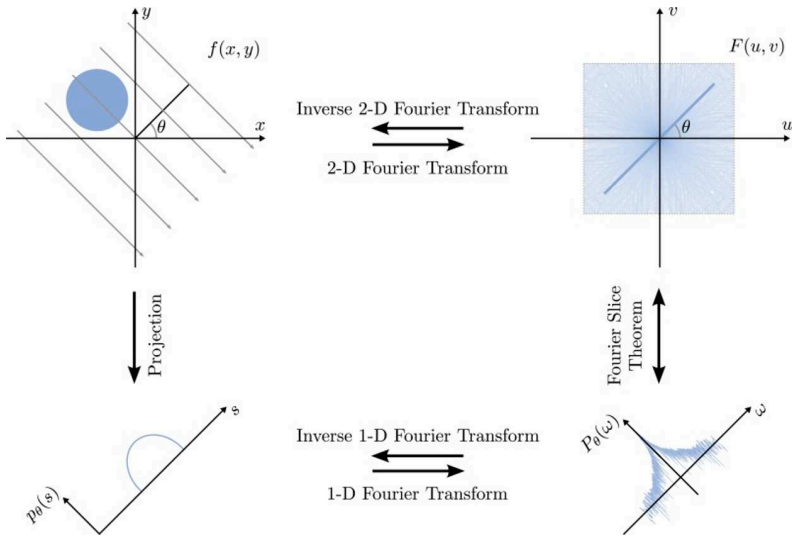

Figure 3.10. The Fourier slice theorem establishes an equivalence between the Fourier transform $P(\omega, \theta)$ ($P_\theta(\omega)$ in the image) of the projection $p_\theta(s)$ and a line in the Fourier transform $F(u, v)$ of $f(x, y)$, which runs through the origin and forms the angle θ with the u-axis. Image taken from [87].

Fourier transforms of its projections, facilitates the reconstruction of the image from its projections. In the reconstruction problem, each column of the sinogram is first subjected to a high-pass filter (it is represented as $|\omega|$ in Equation 3.21) to account for the sparser sampling at higher spatial frequencies. The filtered data are then processed and backprojected from the Fourier space into the real space. Equation 3.21 represents the reconstructed slice f of the object in the cartesian space (x, y) retrieved from 2D Fourier:

$$f(x,y) = \int_0^{\pi} \int_0^{\infty} |\omega| P(\omega,\theta) e^{j2\pi\omega(xcos(\theta)+ysen(\theta))} d\omega d\theta \tag{3.21}$$

3.2.6.2 Reconstruction Algorithms

Reconstruction algorithms are computational methods employed for the purpose of reconstructing axial images from a series of projections. Filtered Back Projection (FBP) and iterative reconstruction algorithms represent two fundamental approaches utilized in image reconstruction, particularly within the domain of medical imaging.

FBP And FDK Reconstruction Algorithms In the context of parallel beam geometry, such as that encountered at a synchrotron facility, the FBP is employed and defined in Equation 3.21. Given the considerable distance between the source

and the detector, which is in the region of hundreds of meters, the configuration of the geometry is considered to be parallel. In contrast, laboratory X-ray setups typically employ a cone beam geometry, in which the distance between the source and the detector is not negligible, resulting in higher magnification than that of synchrotrons ($M \approx 1$). In the case of such a geometry, the Feldkamp Kress Davis (FDK) algorithm is employed instead.

Iterative Reconstruction Algorithms Beside the previously discussed algorithms, iterative algorithms represent a mathematical approach to solve the linearized model of $p = Af$. Here, p represent the measured X-ray projection, f is the computed projection from the current reconstructed image estimated, and A is the non-zero matrix that comprises the experimental geometry.

The object f can hence retrieved iteratively by minimizing of residual error between the measured and the computed projection. More specifically, at each iteration, the iterative algorithm first performs the slice reconstruction, then it applies a forward projection to estimate the projection, and finally it measures the residual error between the two. The methodology for approximating the projection solution, denoted as $\hat{p}$, iteratively can be schematized as in Equation 3.22:

$$\hat{p} = argmin||Af - p||^2 + R(x) \tag{3.22}$$

where $R(x)$ is an optional term that describes a regularization function.

Iterative algorithms divide into two branches: the algebraic reconstruction algorithms (e.g., simultaneous algebraic reconstruction technique - SART), and the statistical-based algorithms (e.g., statistical iterative reconstruction technique - SIRT; maximum likelihood expectation maximization - MLEM; conjugate least gradient squares - CGLS). SART improves image quality by iteratively applying a relaxation factor when refining an initial image, while SIRT averages the corrections over all projections before updating the image estimate. On the contrary, MLEM iteratively maximizes the likelihood of the observed projection data given the estimated image, while CGLS applies the conjugate gradient to the normal equations resulting from the least squares problem.

Even though they are computationally intensive, iterative algorithms perform well with limited and noisy data compared to FBP and FDK. Moreover, the easily incorporation of prior information and constraints make them suitable for advanced and specialized imaging applications.

3.2.7 Common X-ray Tomography Artifacts

X-ray tomography artifacts are distortions in the reconstructed images that can reduce image quality. Common artifacts include ring artifacts, motion artifacts, beam hardening and metal artifacts. Other artifacts can arise from incomplete data or

errors in the reconstruction algorithms, leading to inaccurate representations of the internal structure.

Ring Artifacts Ring artifacts are the most common artifacts in CT images. Dead or saturated pixels in the projections form circular patterns in slices, while high absorbing materials could generate partial rounded shades. There are some algorithms that are able to solve dead or saturated pixels, but lightening pixels are the most difficult one to deal with.

Motion Artifacts Motion artifacts in X-ray tomography are caused by the movement of the object during the scan, which results in distortions of the reconstructed image and makes it more difficult to accurately diagnose or assess the internal structure. The misalignment between projections taken from different angles, caused by this movement, leads to blurry or streaky images.

Metal Artifacts And Beam Hardening In X-ray imaging, the presence of highly absorbing materials, such as metals, can result in the formation of artifacts. Metals absorb a significant amount of radiation, leading to a phenomenon known as beam hardening, where lower-energy X-rays are more readily absorbed, leaving higher-energy X-rays to dominate the image. This leads to image artifacts like streaks or dark bands, as the beam becomes "hardened," distorting the final image by creating non-uniform attenuation.

3.3 X-ray Virtual Histology

X-ray Virtual Histology (XVH) is an advanced imaging technique that produces three-dimensional internal visualizations of biological samples without the necessity for physical slicing.

XVH employs high-resolution X-ray imaging, specifically XPCT, which can achieve resolutions down to the micron level and enable the visualization of the tissues in three dimensions. This allows for the detailed imaging of cellular and subcellular structures, thereby revealing their spatial relationships that might otherwise be missed in two-dimensional slices.

The non-destructive nature of XVH permits the successful implementation of 3D high-resolution applications to all organs that could be observed only at low resolution using conventional CT or MRI, as well as at high resolution using conventional histology. Furthermore, XVH results particularly useful in cases where traditional staining methods are impractical or where the sample must remain intact. These technological advancements offer the production of 3D imaging of biological samples in a non-destructive way, making XVH a powerful tool in biomedical research.

More advanced systems, like synchrotron-based XVH, push the boundaries even further by providing submicron resolutions with exceptional contrast, even in unstained soft tissues, as illustrated in Figure 3.11.

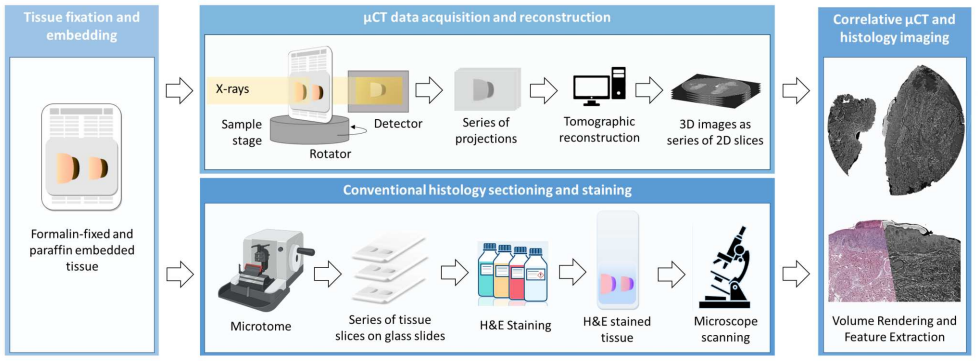

Figure 3.11. A simple workflow for correlative imaging of X-ray Virtual Histology. The same paraffin block undergoes two different investigations, which are X-ray Phase-Contrast Tomography (here referred to as µCT) and conventional histology, and the results are compared and processed for data analysis.

The technology offers a multitude of potential applications, spanning the domains of biomedical research and pathology. Firstly, XVH is employed to study the morphology of tissues, including organs, bones, and soft tissues, without altering their natural state. Secondly, it permits the identification of pathological tissue abnormalities, similar to the traditional histology method, while offering a supplementary 3D perspective of the context. In particular, its application to biological tissues provides an important complement, and in some cases an alternative, to classical histology.

3.3.1 Applications In Biomedical Research And Diagnostics

Over the past two decades, there has been notable interests in the utilization of XPCT for the investigation of biological tissues. The field of applications is extensive, encompassing research into cancer, tissue engineering, and disease.

X-ray virtual histology has demonstrated considerable potential in biomedical research, where its capacity to generate three-dimensional reconstructions of tissue architecture is proving invaluable. It is of particular interest to consider the applications of XVH in the context of neurodegenerative diseases, as evidenced by the literature cited in [88–93]. Similarly, the potential of XVH in pulmonary imaging is supported by the findings of [94–100].

In the field of developmental biology, for instance, researchers are now able to trace the formation of organs and tissues in embryos without the need of the physical sectioning, thus preserving the samples for longitudinal studies [101, 102].

Furthermore, this technology has significant potential in medical diagnostics. For example, XVH has been applied to breast cancer diagnostics [103–108] and to pancreatic cancer diagnostics [109–112] by providing a 3D map of tumor growth and surrounding tissue structures, offering insights into cancer progression that would otherwise require invasive biopsy procedures.

Similarly, XVH holds promise for applications in cardiology and neurology, where imaging of the heart microstructure [113,114] and the brain [115,116] microstructures without damaging tissue could transform the methodology used to study disease.

3.3.2 Challenges And Limitations

As every technique, XVH faces some challenges. One significant limitation is the difficulty in achieving adequate contrast in soft tissues without the use of contrast agents or staining techniques. While synchrotron-based XPCT imaging addresses this issue, such advanced facilities are expensive and limited in access to a restrict number of scientific experts. However, the effort in development new generation of X-ray laboratory facility address this limitation and provides a more accessible alternative. Another challenge is the large volume of data generated by 3D imaging techniques, which requires substantial computational resources for image processing, segmentation, and analysis. As the field progresses, addressing these limitations through innovations in contrast enhancement, data processing algorithms, and safer imaging protocols will be critical for the broader application of X-ray virtual histology in both research and clinical settings.

To conclude, XVH data are challenging to segment due to the relatively poor contrast between tissue types and the volumetric nature of the data, which results in massive amounts of information to process. These factors can complicate manual or traditional segmentation approaches. On the contrary, semantic segmentation algorithms powered by deep learning can overcome these challenges by learning complex patterns and distinguishing subtle differences in tissue features. Leveraging large annotated datasets and advanced architectures, these models achieve high precision and consistency, outperforming traditional methods. Furthermore, their ability to generalize across varying imaging conditions makes them indispensable for analyzing complex XVH datasets. The next section explores the properties and applications of semantic segmentation algorithms in overcoming these challenges.

3.4 Semantic Segmentation

Semantic segmentation is a Deep Learning (DL)-based computer vision task that categorizes each pixel of an image into a label. In medical imaging, it is one of the most used approaches for its capacity to partition digital images into multiple segments of pixels that form distinct categories [117]. The technology facilitates

the production of volume-rendered images, which are of considerable utility in the localization of tumors and other pathologies, as well as in the measurement of tissue volumes and the study of anatomical structure.

Regarding the implementation of DL into the field of imaging, there are three main categories of DL application: Image Classification, which is the process of categorizing groups of pixels; Object Detection, which specifies the location of multiple objects in the image; and Image Segmentation, which creates a pixel-wise mask of each object in the image [118] [119]. Figure 3.12 explains graphically the methodology and architectural approach behind the final output for these three categories. All three approaches have in common the encoding layer, which compresses the extracted patches from the image into a latent space representation. To perform DL-based image segmentation, the decoder layer is required to decode the encoded image back to the original dimension.

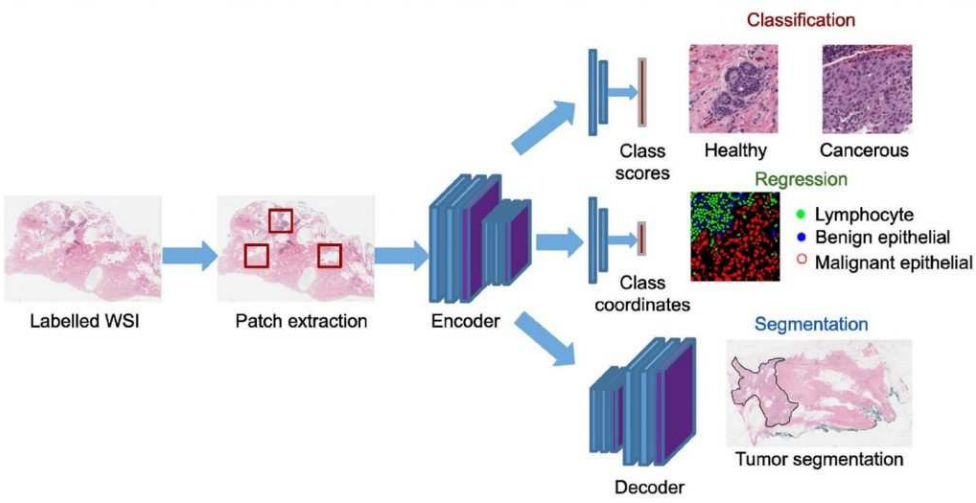

Figure 3.12. Application of tasks of image classification, object detection, and image segmentation to histopathology. Image taken from [120].

Together with instance segmentation, semantic segmentation belongs to the DL algorithms used for image segmentation. While instance segmentation identifies and separates individual objects within an image, making them countable, semantic segmentation categorizes each pixel into a label. These aspects are illustrated in Figure 3.13.

A complex combination of the two methodologies is panoptic segmentation, which solves both instance segmentation and semantic segmentation problems together. The objective of panoptic segmentation is to divide the image into discrete regions or parts that are meaningful from a semantic perspective, while simultaneously identifying and differentiating between individual instances of objects within those regions. In a given image, each pixel is assigned a semantic label, with pixels belonging to classes

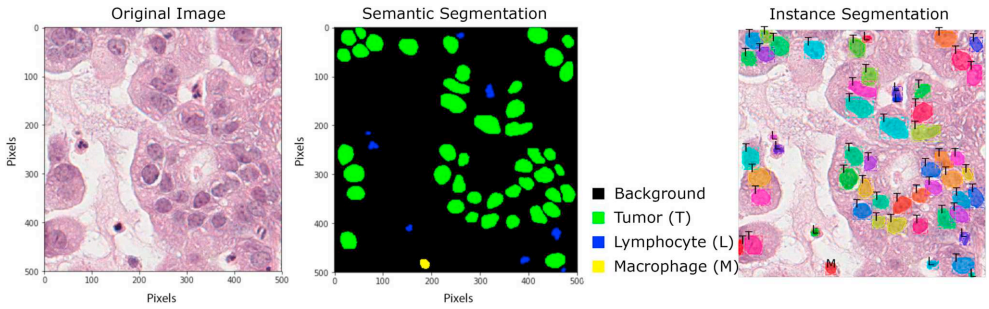

Figure 3.13. Examples of instance segmentation and semantic segmentation approaches applied to segment nuclei in a pathology image. Image taken from [121].

representing countable objects with instances (such as tumor cells and lymphocyte) being assigned unique instance identities.

3.4.1 Deep Learning Concepts

Deep Learning (DL) is a mathematical model derived from Machine Learning (ML) that focuses on understanding complex patterns in unstructured data. It strives to simulate the complex decision-making power of the human brain by employing multilayered neural networks.

In contrast to the classic programming approach, which involves providing data and methods to the model as input to obtain results, DL extracts the rules that relate data and expected results. The objective is to develop generalized models that can be applied with satisfactory outputs to data that has not been previously encountered. Consequently, the term "training" is used to describe the process of utilizing a ML or DL systems, rather than the term "coding".

Unlike traditional machine learning, which relies on manual engineering, deep learning automatizes the extraction process of features. Given sufficient data and computational power, DL models can learn which features are relevant, enabling tasks like image recognition or fraud detection.

In order to perform any DL model, three aspects must be considered: first, the input data; second, examples of the expected results; third, a metric to evaluate the learning rate. The aim is to identify the more suitable input representations that are more likely to minimize the distance between the output produced by the algorithm and the desired one.

3.4.2 Deep Neural Networks

In contrast to traditional neural networks, which typically comprise only two or three neural layers, deep networks may contain hundreds of layers. The depth of these layers permits the introduction of greater complexity. The fundamental operation of

deep neural networks is the mapping of inputs to targets, which is achieved through a series of data transformations. This is accomplished through the data traversing the layers of the network, during which an extensive sequence of data transformations is learned by the model itself.

3.4.2.1 Artificial Neurons And Neural Network

A neural network, in its most basic form, is comprised of a series of interconnected layers of nodes, named neurons. This definition was inspired by the biological neuron, which represents both the anatomical and functional elements of the nervous system. As biological neurons exchange electric signals with other thousands of neurons, neural networks consist of multiple layers of neurons, which are the primary agents in the overall data transformation process. Each neuron can be conceptualized as a processing unit, whereby inputs (x_i) are received, multiplied by weights (w_i), summed, and then subjected to an additional bias (w_0) before being passed through an activation function (g). The concept is shown graphically in Figure 3.14 and mathematically in Equation 3.23.

$$y(x) = g\left(\sum_{i=1}^{n} x_i w_i + w_0\right) \tag{3.23}$$

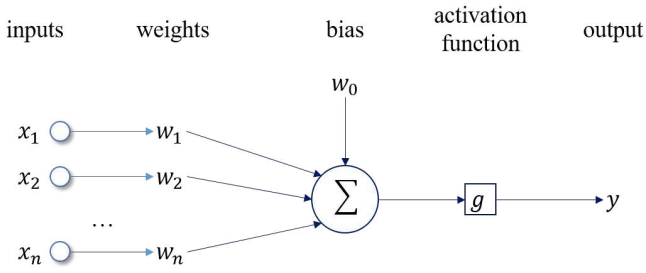

Figure 3.14. A schematic representation of the input elaboration and transformation made by a neuron.

The activation function, which may be either sigmoid or ReLU, introduces nonlinearity, thereby enabling the network to learn complex patterns. Acting as a discriminator, it allows each neuron to determine whether to activate based on the data it receives. As a consequence, by regulating the output of the network's neurons, the activation function influences both the learning processes and the network's predictive capabilities.

3.4.2.2 Forward And Backpropagation

The process of training a neural network comprises two principal stages: forward propagation and backpropagation. In the forward propagation phase, the data flows from the input layer through the network's layers to the output, thereby generating a prediction. Nevertheless, it is possible that the resulting prediction may deviate significantly from the actual outcome, particularly during the initial stages of training.

This is where backpropagation becomes relevant. It is an optimization algorithm that is fundamental to the process of adjusting the network. An error is calculated by comparing the network's prediction with the actual truth. Subsequently, the error is propagated in reverse through the network, with the weights being adjusted using calculus, specifically the chain rule, in order to minimize the error.

3.4.2.3 Loss Function And Optimization Techniques

The discrepancy between the anticipated and actual values is calculated using a loss function, also known as a cost function. This function provides a measure of the discrepancy between the network's predictions and the actual outcomes. The most commonly employed loss functions are mean squared error (MSE) for regression tasks and cross-entropy for classification.

Optimization algorithms, such as Gradient Descent or its variants (e.g., Adam or RMSprop), employ an iterative process whereby the weights in the network are adjusted in order to minimize the loss. This can be conceptualized as a process of navigating on a rough terrain in order to identify the lowest point in a valley. This is analogous to the role performed by these algorithms in the error landscape of the network.

3.4.2.4 Metrics For Performance Evaluation Of The Model

Performance evaluation metrics in deep learning help assess the effectiveness of models. The most commonly employed metrics are accuracy, precision, and recall. The Dice similarity coefficient (F1-score) is a metric that balances precision and recall for imbalanced data sets. It is particularly useful in conjunction with the Jaccard coefficient (IoU) in deep learning, especially for tasks such as image segmentation.

Accuracy Accuracy represents a fundamental metric in the domain of classification. The proportion of correctly predicted instances is quantified in relation to the total number of instances present within the dataset, as figured in Equation 3.24:

$$Accuracy = \frac{TP + TN}{TP + TN + FP + FN} \tag{3.24}$$

where TP stands for True Positive, TN is True Negative, FP means False Positive, and FN is False Negative cases. In circumstances where class distributions

are balanced and the cost of misclassification is uniform across classes, accuracy is a particularly reliable metric.

Precision Precision is a crucial performance indicator in classification tasks, particularly in contexts where the objective is to minimize the number of false positives. As indicated in Equation 3.25, it measures the ratio of accurate positive predictions to the total number of positive predictions generated by the model. This metric offers valuable insights into the model's efficacy in correctly identifying positive instances while minimizing false alarms.

$$Precision = \frac{TP}{TP + FP} \tag{3.25}$$

However, while precision is valuable for minimizing false positives, it does not account for false negatives. Consequently, a model may achieve high precision by making few positive predictions, potentially overlooking many true positive cases.

Recall The recall, also known as sensitivity or true positive rate, is a pivotal metric in the field of classification, as it serves to highlight the model's capacity to identify all relevant instances. It quantifies the ratio of actual positive cases that have been correctly identified by the model to the number of false negative cases, as illustrated in Equation 3.26.

$$Recall = \frac{TP}{TP + FN} \tag{3.26}$$

It is not always advantageous to pursue high accuracy and high recall simultaneously. In certain instances and contexts, it is desirable to seek an imbalance between the two metrics, as this may yield more optimal results.

Dice Similarity Coefficient The dice similarity coefficient, also referred to as the dice-score and F1-score, is one of the most used metrics to evaluate the performance of a model. It is defined as the harmonic mean of precision and recall, as defined in Equation 3.27:

$$DiceScore = \frac{2 \times TP}{2 \times TP + FP + FN} \tag{3.27}$$

In comparison to a conventional average, the harmonic average assigns greater weight to smaller values, thereby accounting for the prevalence of these values in the data set. Consequently, a classifier attains a high F1-score exclusively when both precision and recall are elevated.

Jaccard Coefficient Jaccard index, also known as Intersection over Union (IoU), is a metric used to measure the similarity between two sets. It considers the area of the intersection over the union of the predicted segmentation and the ground truth, as in Equation 3.28:

$$IoU = \frac{TP}{TP + FP + FN} \tag{3.28}$$

In a model with the task of semantic segmentation, IoU and F1-score are the most commonly used metrics because they penalize false positives.

3.4.3 Convolutional Neural Networks

Convolutional Neural Network (CNN) is one of the most common neural network architecture designed for processing image data. It is specialized in processing grid-like data such as images, using convolutional layers to detect patterns and features. CNN enables the identification of patterns such as edges, shapes, and textures, which can be combined to facilitate the recognition of intricate structures, including those observed in cat whiskers and human faces.

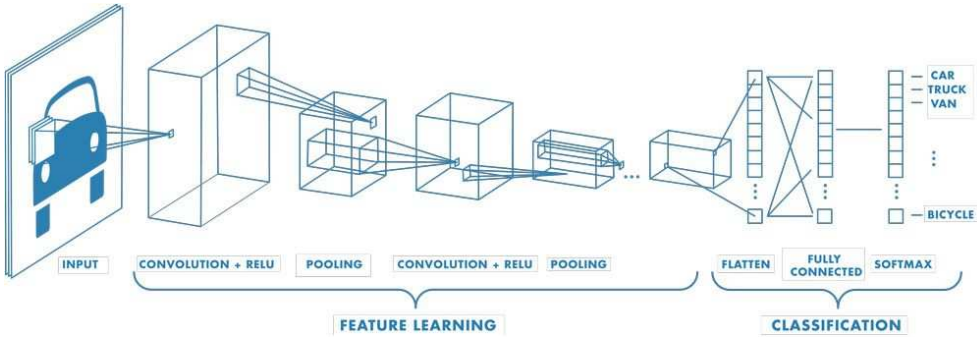

Figure 3.15. Convolutional neural layer architecture design. Image taken from [122].

Like other neural networks, a CNN is composed of three layers: the input layer, which receives the initial data; the hidden layers, intermediate layers that process inputs from the previous layer applying weights and activation functions to model complex patterns; and the output layer, which produces the final prediction or classification. This architectural design consists of a series of layers used for feature identification, followed by layers meant for classification, as shown in Figure 3.15.

3.4.3.1 Feature Detection Layers

Feature detection layers are meant to perform three types of operations on data: convolution, pooling, or rectified linear unit. These operations are repeated over tens or hundreds of layers, with each layer learning to detect different features.

Convolution Convolutional layers are employed to scan input images using convolutions with small, learnable filters, thereby capturing spatial hierarchies. The convolution is a mathematical operation that involves element-wise multiplication and summation of the overlapping values of a small matrix, called kernel or filter, and the large matrix, such as the input image. For a 2D convolution, the process is defined as in Equation 3.29:

$$I(x,y) * K(x,y) = \sum_{m=-\infty}^{+\infty} \sum_{n-\infty}^{+\infty} I(m,n) \cdot K(x-m, y-n) \tag{3.29}$$

where $I(x,y)$ represents the input matrix, and $K(x,y)$ is the kernel. To control the size of the output matrix, padding can be added. The result is the production of a new matrix, known as the feature map or convolved feature, that is the sum of element-wise products.

Pooling Pooling layers at subsequent stages serve to further reduce the data set in terms of both its dimensions and computational demands placed upon the system. The pooling operation simplifies the output by performing non-linear downsampling on the spatial dimensions of the input feature map, reducing the number of parameters that the network needs to process and learn about. There are several types of pooling operations, each with different approaches to downsample the feature map: max pooling, which extracts the most prominent features in each region; average pooling, which considers the average value of features in each region; global max or average pooling, which selects the maximum value or the average of all values in the feature map. The goal is to reduce the computational complexity of the network, make the model robust to variation and distortions, and help in controlling overfitting.

Rectified Linear Unit Rectified Linear Unit (ReLU) is a type of activation function that permits more rapid and efficacious training. The purpose of introducing a ReLU layer is to introduce non-linearity in the network, enabling its capacity to learn from complex data. By assigning negative values a value of zero and maintaining positive values, ReLU functions as a neuron that discriminates between instances of activation and information transfer. In other words, it determines when to activate and to pass information forward, and when to deactivate and halt the flow of such information. This concept can be represented by the Equation 3.30:

$$ReLU(x) = max(0, x) \tag{3.30}$$

where ReLU is a half rectified function, since $ReLU(x)$ is zero when x is less than zero and it is equal to x when x is above or equal to zero. The drawback of the negative side of the graph is to set to zero its gradient value. This implies that this function lacks the possibility of updating weights and biases for some neurons during the backpropagation process. If too many inputs lead to negative values, many neurons may output zero for all inputs, effectively not contributing to the learning

process. To overcome the so-called "dying ReLU problem", many variants have been proposed. One such variant is the Leaky ReLU, which is defined in Equation 3.31:

$$LeakyReLU(x) = max(\alpha x, x) \tag{3.31}$$

By employing a relatively modest positive value (such as 0.01) for the parameter α, the Leaky ReLU function allows a slight non-zero gradient for negative inputs. This effectively circumvents the issue of the "dying ReLU" and expands the range from $[0, \infty]$ to $[-\infty, +\infty]$.

3.4.3.2 Classification Layers

After the feature detection layers, the architecture of CNN shifts to classify the results. This stage is crucial for assigning probabilities and classifying features.

Flatten Flattening is a fundamental procedure used to connect the output of the convolutional-based layers to the fully connected layers. The process involves the conversion of multi-dimensional input, typically a two-dimensional feature map or a three-dimensional tensor, into a one-dimensional vector.

Fully Connected Layer Fully connected layers, known as dense layers, are critical for combining and processing features extracted by earlier layers. As a type of neural network layer, whose concept was previously described in Section 3.4.2.1, every neuron is connected to every neuron of the previous layer and exchanges information. As every deep transformation occurring in each layer is stored in weights, CNN weights and biases are shared and equal for all hidden neurons in a certain layer. This means that every hidden neuron retrieves the same feature in different parts of the image. The goal is to gain tolerance for the identification of objects independently from the position occupied in the image. The principal objective of fully connected layers is to facilitate the process of learning complex representations of data through the integration of diverse features and the development of non-linear decision boundaries. The final product of this step is a vector, whose length is equal to the number of classes of the classification problem.

Softmax The final layer of the CNN architecture is the softmax function that provides the classification output. The output is a vector of the dimension of the classes to be predicted, in which every class has assigned a probability.

The objective of this chapter is to establish a comprehensive foundation on the imaging techniques and advanced technologies constituting the basis of this thesis. The subsequent chapter will delve into the "Materials and Methods", detailing the experimental protocols employed to develop the X-ray Virtual Histology applications.

CHAPTER 4

Materials And Methods

This chapter delineates the experimental protocols and methodologies employed in this thesis. The chapter, which is divided into four sections, provides a comprehensive overview of the experimental framework that supports the findings of this research. Firstly, Section 4.1 outlines the methodology employed for the optimization of the synchrotron-based X-ray virtual histology. The subsequent Sections 4.2 and 4.3 present the application of this technique to the study of melanoma and skin tumors, and non-small cell lung cancers (NSCLC), respectively. Finally, Section 4.4 explores the application of X-ray virtual histology in an X-ray laboratory context.

To this end, Formalin-Fixed Paraffin-Embedded (FFPE) blocks containing biological tissue were selected by the Department of Pathology of the University Hospital of Cattinara (Trieste, Italy) for X-ray Phase-Contrast micro-Tomography investigation at the SYRMEP beamline of Elettra synchrotron (Trieste, Italy) [123]. Conventional histology was used to discriminate the most noteworthy cases based on the diagnostic and morphological tissue properties.

4.1 Optimization Of Protocol For Synchrotron X-ray Virtual Histology

The following sections present five typologies of experimental properties that are relevant to the optimization of synchrotron-based X-ray virtual histology: the spatial resolution, two distinct medium embedding configurations, the optimal exposure time, the optimal orientation of the FFPE block, and the most effective experimental setup, focusing on pixel size and sample-to-detector distance. These aspects are all considered to improve image contrast and quality using the selected synchrotron beamline.

4.1.1 Methodology For Testing Spatial Resolution With Micro-CT Bar Pattern Phantom

The Micro-CT bar pattern NANO phantom[1] (QRM GmBH, Germany) in Figure 4.1 was used for a directly visible measurement of spatial resolution in micro-CT. The X-ray acquisition was performed at the SYRMEP beamline employing the parallel beam

[1] https://www.qrm.de/en/products/micro-ct-bar-pattern-phantoms-airnano-customized

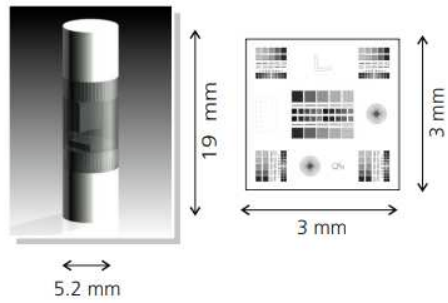

Figure 4.1. Graphical representation of the Micro-CT bar pattern phantom. The left image reports a 3D schematic of the cylindrical phantom with a vertical and a horizontal chips. The right image presents a magnified view of the embedded test pattern, which includes bar patterns and structures for resolution assessment, contained within a 3 mm × 3 mm area. Image taken from the QRM flyer.

geometry and the polychromatic beam configuration. Micro-CT images were collected with an Orca Flash 4.0 sCMOS camera (2048 × 2048 pixels^2 sensitive area), which was coupled with a 17 µm thick GGG scintillator. The white beam was filtered with a 1.0 mm Al filter. The effective pixel size was set at 2 µm with a Sample-to-Detector Distance (SDD) of 200 mm and a 21.0 keV average X-ray energy. 1800 projections were acquired over a 180° rotation with 50 ms exposure time. The projections of the test object were flat fielded (the procedure is reported in the paragraph "Pre-Processing" of Section 4.2.2) and reconstructed with a FBP algorithm in attenuation with the open source software SYRMEP Tomo Project [124]. To assess the spatial resolution, the line profile of pixel intensity was considered perpendicular to bar patterns.

4.1.2 Assessment Of Skin Tissue Embedded In Paraffin And In Agar Medium Via XPCT

Two excised formalin-fixed skin tissues were provided by the Department of Pathology of the University Hospital of Cattinara (Trieste, Italy). They were embedded in two different pipettes with melted agar, and then scanned at the SYRMEP beamline of Elettra synchrotron (Trieste, Italy). The X-ray acquisition was conducted employing the parallel beam geometry and the polychromatic beam configuration, setting a SDD of 200 mm, an effective pixel size of 2.0 µm and a 21.0 keV average X-ray energy. Projections were collected with an Orca Flash 4.0 sCMOS camera (2048 × 2048 pixels^2 sensitive area), which was coupled with a 17 µm thick GGG scintillator. 1800 projections were collected over a 180° rotation with an exposure time of 50 ms, in order to reduce the melting of the agar medium. Projections were flat fielded, phase retrieved with the algorithm based on the Transport of the Intensity Equation (TIE-Hom, [85])

using a δ over β ratio of 200 (see the paragraph "Phase-Retrieval" of Section 4.2.2), and then reconstructed with FBP reconstruction algorithm. Conversely, a FFPE block containing a skin tissue was scanned employing the same configuration settings, except for the exposure time set to 200 ms.

4.1.3 Evaluating Sample Orientation For XVH Protocol

An excised tissue of lung cancers with a diagnosis of adenocarcinoma in a FFPE block was scanned at the SYRMEP beamline of Elettra synchrotron (Trieste, Italy). It was placed on the rotator stage in two different positions, horizontally and vertically. The X-ray acquisitions were carried out under consistent conditions, with a SDD set at 200 mm and a pixel size of 2.0 µm in parallel and white beam. An Orca Flash 4.0 sCMOS camera (2048 $\times$ 2048 pixels^2 sensitive area) coupled with a 17 µm thick GGG scintillator was used to collect micro-CT projections. To ensure comprehensive visualization of the entire pathological area of the sample, the field of view was increased. To this end, a total of 3600 projections were captured over a full 360° rotation, with an exposure time of 200 ms per projection. This approach, namely extended Field-Of-View (FOV), is described in the paragraph "Pre-Processing" of Section 4.2.2. In conclusion, projections were flat fielded, processed to extend the FOV, phase retrieved using TIE-Hom algorithm with a δ over β ratio of 200, and then reconstructed with FBP reconstruction algorithm.

4.1.4 Testing Procedure Of Propagation-Based Parameters

The same biopsy, considered for experiment 4.1.3, was acquired at several SDD and pixel sizes, as reported in Table 4.1. The parallel geometry and the polychromatic

Config.	**Pixel Size [µm]**	**SDD [mm]**	**Average Energy [keV]**
A	0.9	90	19
B	2.0	90	21
C	4.0	90	21
D	0.9	250	19
E	2.0	250	21
F	4.0	250	21
G	0.9	400	19
H	2.0	400	21
I	4.0	400	21

Table 4.1. Experimental configurations, varying pixel size and sample-to-detector distances, considered as characteristics for propagation-based imaging setup. The discrepancy in average energy across the configurations is attributed to the adjustments in exposure time and beam filtering, which were implemented to guarantee a consistent photon flux per unit area despite the expansion of the field of view and the concomitant increase in pixel size.

beam of the SYRMEP beamline setup were exploited. The experimental parameters of exposure time and beam filtering were modified with the objective of achieving a similar mean number of counts per pixel across all configurations. The adjustment was necessitated by the considerable increase in photon flux per unit area resulting from the enlargement of the field of view as the pixel size increases. To this end, when scanning at 0.9 µm pixel size, the exposure time was set at 100 ms and the beam was filtered with a 0.5 mm Si filter. For the 2.0 µm pixel size configurations, the exposure time was fixed at 100 ms while the beam was filtered by a 1.0 mm Si filter. In final instance, for the configurations with 4.0 µm pixel size, the exposure time was increased to 200 ms and the beam was filtered by a 1.0 mm Si filter. Using the Orca Flash 4.0 sCMOS camera (2048 × 2048 pixels^2 sensitive area) coupled with a 17 µm thick GGG scintillator, 1800 projections were obtained over a 180° rotation of the sample. All projections were subjected to flat-fielding, processing with the TIE-Hom phase-retrieval algorithm that incorporated selective input of the setup parameters and a δ over β ratio of 200, and reconstruction using the FBP algorithm.

4.1.5 Methods For Testing Effects Of Exposure Time

A neuroendocrine neoplasm stored in FFPE block was scanned using different exposure times (50ms, 100ms, 200ms). The X-ray acquisitions were performed employing the white beam in parallel geometry and the Orca Flash 4.0 sCMOS camera (2048 × 2048 pixels^2 sensitive area) coupled with a 17 µm thick GGG scintillator. Micro-CT data were obtained retrieving an effective pixel size of 2.0 µm, an SDD of 20 cm, and an average X-ray energy of 21 keV. 1800 projections were collected over a 180° rotation of the sample. Projections were flat-fielded, filtered with TIE-Hom phase-retrieval algorithm ($\delta/\beta = 200$), and then reconstructed with FBP algorithm.

To assess the visibility of the three configurations, a Contrast-to-Noise Ratio (CNR) was calculated, taking into account three Region-Of-Interest (ROI)s, namely tumor, stroma and healthy tissue, compared to background. The CNR was calculated using the following Equation 4.1:

$$CNR = \frac{\mu_{ROI} - \mu_{BKG}}{\sqrt{\frac{1}{2}(\sigma^2_{ROI} + \sigma^2_{BKG})}} \tag{4.1}$$

with µ denoting the average and σ the standard deviation, both calculated on the ROIs and the background (BKG).

4.2 Application Of X-ray Virtual Histology To Melanoma And Skin Tumors

Excised tissues from patients with high suspicion of cancer diagnosis were formalin-fixed and embedded in paraffin, as the standard procedure for clinical practice, and

then considered for histopathological examination. 32 FFPE blocks containing various typology of human skin tissues and tumors excised, as listed in Table 4.2, were considered for the study of the invasive properties of melanoma.

Skin tissue type	**Quantity**
Control tissue	5
Nevus	3
Seborrheic keratoses	4
Basal cell carcinoma	2
Melanoma in situ	4
Superficial spreading melanoma	8
Nodular melanoma	6
	32

Table 4.2. List of all the cutaneous tissue considered for XPCT investigation.

4.2.1 Conventional Histology

Conventional histology was performed on each FFPE block for histopathological examination. The slicing procedure was repeated to extract additional internal sections of 3-5 µm thickness for histological validation with X-ray micro-Tomography images. Whole-slide images were scanned using a D-Sight 2.0 digital microscope with a $\times 200$ magnification and a 0.25µm pixel resolution.

4.2.2 X-ray Phase-Contrast Micro-CT

As synchrotrons have policy access based on the quality of the proposed experiment, proposal no. 20225155 entitled "X-ray Phase Contrast 3D Virtual Histology for the assessment of staging in human melanoma tissue" with principal investigator G. Saccomano, was written and accepted by the scientific commission panel to have access to the SYRMEP beamline of Elettra synchrotron (Trieste, Italy).

4.2.2.1 Data Acquisition

The propagation-based imaging setup of the SYRMEP beamline, viewable in Figure 4.2(a), was employed for both experiments. To ensure the sample did not move during the X-ray acquisition, FFPE blocks were positioned on a dedicated sample stage onto the rotator stage of the SYRMEP beamline setup, as illustrated in Figure 4.2(b).

All experiments were conducted employing the white-beam configuration. The electron storage ring was operating at 2.0 GeV with a beam current of 308.1 mA. Projections were collected with an Orca Flash 4.0 sCMOS (2048×2048 pixel^2 sensitive area) coupled with a 17 µm thick GGG scintillator. In accordance with the

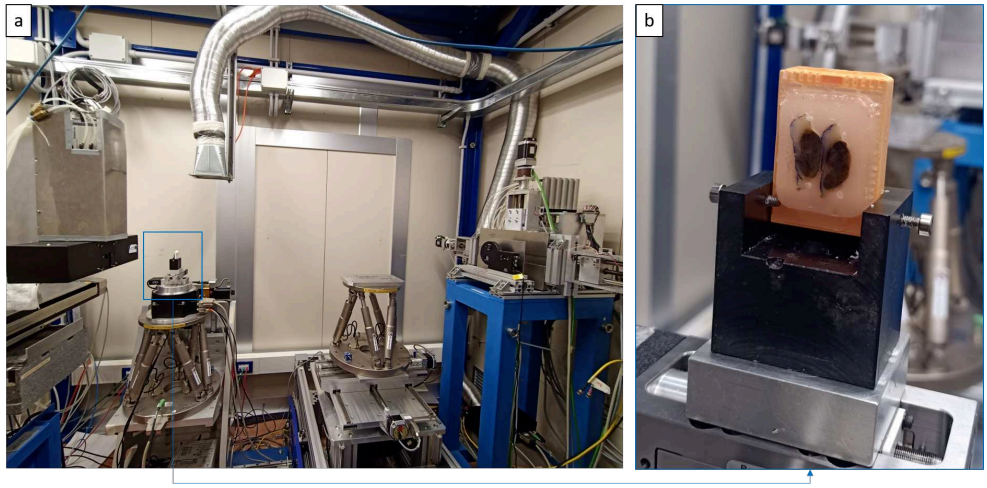

Figure 4.2. (a) Image of the setup taken at the SYRMEP beamline of Elettra synchrotron (Trieste, Italy) in 2022. From the right to the left, X-rays coming from the accelerator pass through the sample positioned onto the rotator stage and then are collected by the detector coupled with a scintillator. (b) A dedicated sample stage employed for XVH applications.

findings presented in Section 5.5, which discuss the ideal phase-contrast properties of the setup for XVH investigation, the sample stage was positioned 200 mm away from the detector to collect data at 2 µm pixel size. The energy spectrum was adjusted by filtering the X-ray beam with a 1.0 mm Al filter. All acquisition parameters are available in Table 4.3.

Experimental parameters	
Pixel size	2 µm
Sample-to-detector distance	200 mm
Average X-ray energy spectrum	21 keV
Projections	3600
Scan rotation	360°
Exposure time	200-250 ms

Table 4.3. XPCT acquisition and reconstruction parameters employed at the SYRMEP beamline of Elettra synchrotron. The values reported for exposure time varies depending of sample thickness and photons statistics at the detector.

The exposure time was adjusted in accordance with the X-ray absorbance properties of the sample during the radiographical examination. In particular, the X-ray statistics collected at the detector were found to be influenced by the amount of paraffin present within the FFPE block. To illustrate this point, Figure 4.3 presents three distinct paraffin embedding shapes. While the orange FFPE blocks require longer

X-ray exposure, the green one yields adequate contrasts with a reduced acquisition time.

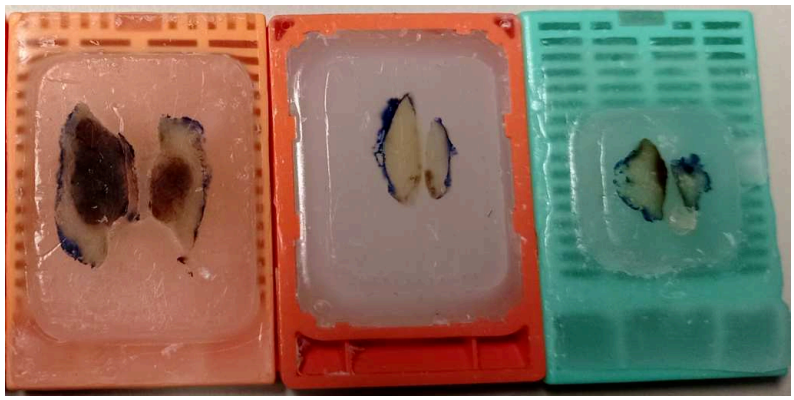

Figure 4.3. Three out of thirty-two FFPE block considered for synchrotron-based XVH investigation. The amount of paraffin used is consistent with the sample dimensions.

Due to sample size, the extended field-of-view acquisition modality (i.e. off-center rotation over 360 degrees) was employed to cover a bigger area of the sample. Multiple vertical and horizontal acquisitions were performed to cover all the relevant portions of the sample within the FFPE block in a so-called "mosaic CT" mode.

4.2.2.2 Data Reconstruction

All datasets were reconstructed using the open-source software SYRMEP Tomo Project [124], developed for propagation-based phase-contrast parallel-beam CT. The software implements the steps described in the following paragraphs.

Pre-Processing The projections were corrected using a flat-fielding technique, which involved the use of dark and flat images, as follows:

$$proj = \frac{proj - dark}{flat - dark}$$

The dark images were acquired while the beam was off, while the flat images were obtained when the beam was on but the sample was outside the field of view. All data were acquired using the Extended FOV mode, which refers to performing two consecutive 180° scans with the axis of rotation translated off-center. As explained in Figure 4.4, the displacement of the axis of rotation causes the projections to shift laterally and enables the scansion of a bigger area of the sample. By the stitching of complementary datasets acquired over 360°, the resulting projections dataset becomes a wide-view dataset, approximately twice the size of the original dataset. Projections were filtered using a ring removal algorithm that removes the dead pixels visible as vertical lines present in the sinogram [125].

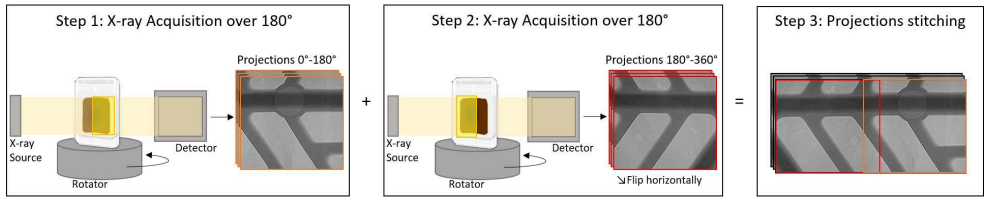

Figure 4.4. Graphical representation of the workflow to perform the extended Field-Of-View (FOV) micro-CT imaging. Firstly, the axis of rotation must be shifted laterally. Then, two consecutive X-ray acquisitions over 180° are performed and the resulting projections are stitched to generate projections almost twice the size of the original ones.

Phase-Retrieval The phase retrieval algorithm based on the Transport of Intensity Equation (TIE-Hom) [85] was applied to the pre-processed projections. The parameters employed depend on the setup configuration (e.g., pixel size, distance, X-ray energy) reported in Table 4.3. To retrieve the phase-contrast effect, the δ over β ratio was set to 200. The computation was performed employing both experimental and material properties. As indicated in the NIST XCOM Database [126], the refractive index δ and the absorption index β for soft tissues, such as skin tissue, were retrieved as $\delta = 2.0 \times 10^{-7}$ and $\beta = 1.0 \times 10^{-9}$ at the average energy of the spectrum at 21 keV.

Reconstruction Lastly, pre-processed projections were reconstructed using an implementation of the Filtered Back Projection algorithm with the so-called ram-lak filter. For each dataset, the software produced thousands of slices in a 32-bit format, with a total file size exceeding 80 Gb.

4.2.2.3 Data Post-Processing For Mosaic CT

After the reconstruction of each individual dataset, additional processing is required to combine the multiple scans into a complete reconstruction of the sample. The steps undertaken to achieve this are described in the following paragraphs.

Vertical Stitching As multiple acquisitions were performed on the same sample to cover all the tissue inside the FFPE block, reconstructed slices were stitched vertically with an in-house Python script detecting the best phase correlation in the boundaries intervals of adjacent scans.

Image Conversion As each pixel represents the intensity of the photons incident to the pixel of the detector, 32 bit format is an intense format that could contain more than 4 million shades of grayscale in a single pixel. Although 32 bit format is the preferred choice to maintain a high dynamic range, it is a relatively costly computational process. Consequently, images were converted into a more handle

format. The assignation of pixels from 32 bits to 8 bits consists of normalizing the intensity value $I(x, y)$ of the image I at the pixel coordinates x, y by the minimum and maximum intensity values, I_{min} and I_{max}, respectively, computed across all images contained in a stack. In the scenario of multiple acquisitions to cover the entirety of the sample area, the minimum and maximum intensity values were automatically calculated on a subset of images from each stack, with a fine step size to accommodate for potential variations. The methodology can be expressed as follows:

$$I(x, y) = \frac{I(x, y) - I_{min}}{I_{max} - I_{min}}$$

The resulting histograms will appear to have the same shape but different intervals. Some outliers in the original image could compress the histogram, while an excessive constriction of the interval could stretch the histogram. In both cases, the resulting image may lose contrast resolution.

Z-Reslicing All reconstructed slices were considered for reslicing, which refers to reformatting a 3D image stack without scaling along a different axis, typically the z-axis. As the vertical orientation of the sample as in Figure 4.2(b) was considered, the z-axis represented the depth of the image stack. Consequently, Z-reslicing was employed to obtain the preferred visualization consistent with the histopathological section plane.

4.2.2.4 Semantic Segmentation With Deep Learning

Several semi-automatic segmentation methods based on deep learning were tested on different XPCT datasets with multiple applications. Firstly, a semantic segmentation approach was used to retrieve the melanocytic lesion in a selected skin tissue dataset.

Background Removal The background was removed by masking the biological tissue with respect to the paraffin background, plastic boxes, and external air bubbles. Using Avizo 3D, approximately three or four 2D sparse annotations were marked as seeds the tissue and the background, and then considered for 3D watershed segmentation by first computing the image gradient.

Data Preparation 22 datasets of skin tissues were selected for the training and the validation set and 8 datasets were assigned to compose the test set (training 70%, validation 15%, test 15%). Three micro-CT annotations were performed considering manually annotated histologies as a reference for segmenting the melanocytic lesion. Three classes (Melanocytic Lesion, Control Tissue, and Background) were defined as labels. Specifically, melanocytic lesion class includes only single and nested malignant melanocytes, necrosis, and ulceration excluding e.g., tumor infiltrate lymphocytes, and macrophages. Control tissue class includes every other skin aspect, thus meaning e.g., normal epidermis, dermis, hypodermis, vessels, keratin-filled cysts, and clusters of benign melanocytes.

nnUNet Model An AI-based semantic segmentation model, named nnUNet (v.2) [127], was adopted to perform the segmentation task. The criteria for selecting the nnUNet model were its automated configuration, robustness to variability, and reproducibility. As the nnUNet model is designed to handle datasets of varying sizes, image resolutions, and intensity distributions with efficacy, the network configuration parameters were automatically extracted and adapted to align with the composition of the training set. Subsequently, the default cross-validation technique employed five trained U-Net networks to obtain a robust assessment of the model's performance. To ensure optimal performance, each validation set was constructed to ensure a uniform distribution of benign and malignant cases across both the training and validation folders. The composition of the validation set is reported in Table 4.4. Lastly, the nnUNet model is readily reproducible and editable, provided that consistent training and inference pipelines are employed.

Fold 0	**Fold 1**	**Fold 2**	**Fold 3**	**Fold 4**
1 NMM	1 NMM	1 NMM	1 NMM	1 NMM
1 SSM	1 SSM	1 SSM	1 SSM	1 SSM
1 MIS	1 MIS	1 MIS	1 SSM	1 Seb-ker
1 Seb-ker	1 Seb-ker	1 Nev	1 Nev	1 Nev
1 Ctrl	1 Ctrl	1 Ctrl	1 Ctrl	1 Ctrl

Table 4.4. Validation set composition per five-validation-folders. Legends: NMM, nodular malignant melanoma; SSM, superficial spreading melanoma; MIS, melanoma in situ; Seb-ker, seborrheic keratoses; Nev, nevus; Ctrl, control tissue.

A pipeline of two consecutive networks was designed. Initially, a preliminary 2D nnUNet network was employed in the generation of 3D volume-of-interest (Volume-Of-Interest (VOI)s) labels from 2D region-of-interests (ROIs). These 3D VOIs were subsequently employed in the configuration of the final 3D nnUNet network, which combined both 2D and 3D configurations.

nnUNet 2D Configuration 10 ROIs per XPCT slice were selected from each manual annotation based on the containing the most interesting pathological features of melanoma. A total of 660 ROIs was considered for training the model (528 ROIs for training set, 132 for validation set). Several image and network parameters have been tested to define the best nnUNet approach for such micro-CT images. To compare their performance, several full cross-validations of 100 epochs were computed and validated on the test set. These tested parameters are reported in 4.5. After that, a full cross-validation was run using the desired parameters for 2D configuration, which resulted to be Configuration I of Table 4.5. The segmentation network was trained on a Nvidia RTX 2080 Ti GPU Card with 48 GB of dedicated RAM memory. To show the outcome of 3D lesion segmentation, the resulting model was inferred on whole-micro-CT volumes, and refined with 3D interpolation.

	ROI size	Patch size	Batch size	ROI norm	Data norm
A	1024×1024	512×512	12	z-score	IN
B	512×512	512×512	12	z-score	IN
D	1024×1024	256×256	12	z-score	IN
E	1024×1024	768×768	12	z-score	IN
F	1024×1024	512×512	4	z-score	IN
G	1024×1024	512×512	20	z-score	IN
H	1024×1024	512×512	12	[0,1]-scale	IN
I	1024×1024	512×512	12	z-score	BN

Table 4.5. Multiple 2D model configuration trained varying deep-learning characteristically parameters (e.g., input image size, patch size, batch size, image and data normalization). All models were trained for 100 epochs.

Performance Evaluation Of The Model The dice score, accuracy, precision, and recall were computed every epoch by calculating the pixel populations of true positive, true negative, false positive, and false negative. All metric results were averaged per cross-validation folder [23] and considered with a 95% confidence interval.

Quantitative Volume-Retrieved Parameters Surface area, volume, and maximum tumor extension (e.g., Breslow thickness) were retrieved with Python scripts (employing scikit-image [128] and matplotlib [129] libraries) considering a set of 200 consecutive micro-CT slices (corresponding to 400 µm depth within the FFPE block). The Breslow thickness was estimated by computing the maximum normal component to the surface of the skin, in the case of superficial melanoma, and the maximum diameter, in the case of nodular melanoma. Additionally, the average and the standard deviation of the measurements were also provided. The volume of the lesions was visualized three-dimensionally employing Avizo 3D software (Thermo Fischer, Germany).

4.3 Application Of X-ray Virtual Histology To Non-Small Cell Lung Cancers

25 FFPE blocks of human lung tissues, as listed in Table 4.6, were selected based on studying the most invasive properties in lung cancers. The tissues were initially examined using conventional histology to establish a diagnosis, and subsequently investigated using XPCT.

Lung tissue type	Quantity
Adenocarcinoma	16
Squamous cell carcinoma	3
Control tissues	3
	22

Table 4.6. Types of lung tissues stored in FFPE blocks considered for XVH investigation.

4.3.1 Conventional Histology

The standard conventional histology production of H&E glass slides was conducted in accordance with standard protocols for diagnostic purposes. Subsequently, the samples were digitized via microscope and a research slide scanner.

Microscope-Based Histology The glass slides containing lung tissue sections were observed via a Leica microscope (DMRME301-371.011 type, Mannheim, Germany), and the most characteristic regions were saved digitally employing a digital camera for microscope. A ruler was used as a reference to retrieve the pixel size at 5× and 20× magnification of the microscope, as represented in Figure 4.5. The pixel size was determined by considering the total number of pixels counted in an interval of 1 mm. Computed pixel sizes are reported in Table 4.7.

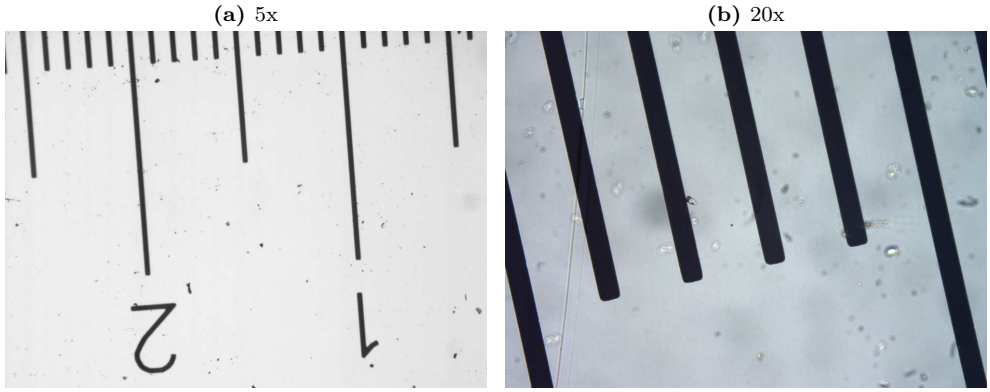

Figure 4.5. Magnification 5x (a) and 20x (b) of the same reference ruler.

Magnification	Pixel size [µm]
20x	0.27
5x	1.01

Table 4.7. Retrieved pixel size from reference image (20x, 5x magnification).

All histologies, acquired with the Leica microscope scanner in brightfield mode, were converted to gigapixel resolution using VIPs software [130].

Research Slide Scanner All lung tissue samples, reported in Table 4.6 and mounted on glass slides, were scanned using an Olympus research slide scanner (Slideviews, VS200, Tokyo, Japan) equipped with a CMOS camera (3.45 µm × 3.45 µm pixel size). The acquisitions were conducted in brightfield using a 20× objective and a 0.8 numerical aperture, which corresponds to a pixel size of 0.27 µm. Subsequently, the digital WSIs were visualized and processed with QuPath, open-source software [131].

4.3.2 X-ray Phase-Contrast Tomography

Proposal no. 20230337, with the title "X-ray virtual histology for the 3D assessment of lymphovascular invasion in resected non–small cell lung cancer" and principal investigator Prof. F. Brun, was approved by Elettra commission panel for beamtime at the SYRMEP beamline of Elettra synchrotron (Trieste, Italy).

4.3.2.1 Data Acquisition, Pre-Processing, And Reconstruction

All data were collected in accordance with the identical experimental parameters delineated in Table 4.3 of X-ray virtual histology for melanoma experiment in Section 4.2.2. Moreover, all data processing and reconstruction stages were conducted as reported in Section 4.2.2.

4.3.2.2 Data Post-Processing

Due to the considerable computational demands associated with the processing of lung tissue within FFPE blocks, a combination of horizontal and vertical stitching techniques was employed using Avizo 3D software. The methodology entails the registration of two or more volumes at a time, with the computation of the normalized mutual information [132], followed by the utilization of Lanczos interpolation for their subsequent merging. Stitched volumes were then considered for 3D visualization and rendering purposes.

Moreover, the maximum intensity projection approach was employed to visualize both the progression of the tumor and the vascularization in some samples. This method projects the most intense pixels extracted from a subset of images in the visualized plane. In contrast, the minimum intensity projection approach, which acts as the previous method but considers the least intense pixels, was used to draw the tubular lymphatic vessels.

4.4 Applications Of Laboratory-Based X-ray Virtual Histology

Five FFPE blocks of human skin tissues were selected considering few types of lesions, as listed in Table 4.8, and scanned in an X-ray laboratory using propagation-based imaging technique.

Skin Tissue Type	Quantity
Seborrheic keratosis	1
Nevus	1
Superficial spreading melanoma	2
Nodular malignant melanoma	1
	5

Table 4.8. Types of skin tissues stored in FFPE blocks considered for XVH investigation.

4.4.1 X-ray Phase-Contrast Tomography With Propagation-Based Imaging Setup

Two experiments were designed to assess the feasibility of using propagation-based imaging in an X-ray laboratory (OptImaTo laboratory, Trieste, Italy [133]) with the objective of studying the skin tissues within FFPE blocks.

4.4.1.1 A Feasibility Test Of Lab-Based PBI X-ray Virtual Histology On A Melanoma Skin Tissue

Experiment was conducted employing a X-rays microfocus liquid-metal-jet source (MetalJet D2+, Excillum, Stockholm, Sweden) and a Lambda 350k detector (X-Spectrum, Hamburg, Germany) with a 75 µm pixel size. The X-ray source (tube voltage: 70 kV, tube current: 3.57 mA, focal spot width: 80 µm, focal spot height: 20 µm) was filtered with a 1.4 mm Al. A melanoma tissue embedded in a FFPE block was simply positioned on the sample stage as appreciable in Figure 4.6. The propagation-based setup was exploited using a Sample-to-Source Distance (SSD) of 380 mm and a sample-to-detector distance (SDD) of 2280 mm, obtaining a magnification factor of 6. The effective pixel size was 12.5 µm. Low-statistics experiment involved the collection of 1080 projections over a 360° rotation with an exposure time of 4.5 s, while the high-statistics experiment collected 1080 projections with 3 repetitions over a 360° rotation with an exposure time of 4.5 s. Data were processed for phase retrieval and ring artifacts removal, and then reconstructed using TIGRE library [134].

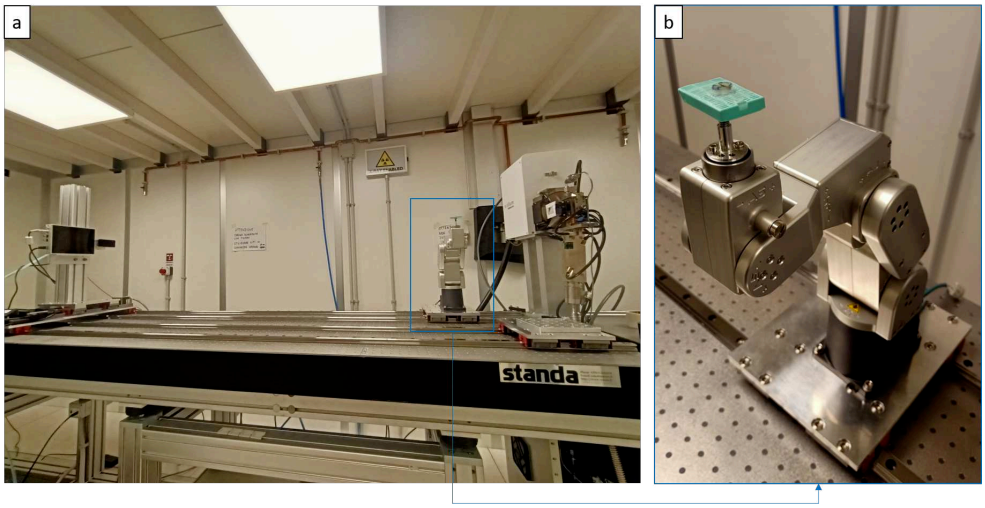

Figure 4.6. (a) Experimental setup of OptImaTo Laboratory (University of Trieste, Trieste, Italy), with (b) a closer look at the sample stage and rotator.

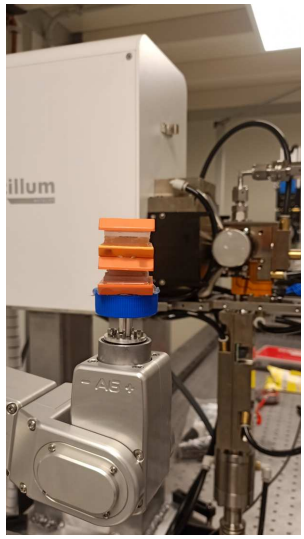

Figure 4.7. Four FFPE blocks stacked vertically to be scanned at Optimato Laboratory.

4.4.1.2 "Sandwich"-Based Configuration For X-ray Virtual Histology

The experiment was repeated using a CMOS detector (Varex, Salt Lake City, United States of America) with a 75 µm pixel size. Employing the same acquisition parameters of the feasibility test, the effective pixel size resulted to be 12.5 µm. Four FFPE blocks - containing one superficial spreading melanoma, one nodular melanoma, one nevus, and one seborreheic keratosis - were selected to construct the sandwich-like configuration as in Figure 4.7. Each sample was affixed to the adjacent sample with wax, and the bottom sample was attached to the sample support with hot glue to prevent any motion during the acquisition process. Subsequently, the sandwich-like sample configuration was secured to the sample stage via screws. Two vertical acquisitions were performed to include two FFPE blocks at a time. Data were processed for ring artifacts removal and phase retrieval using a δ over β ratio of 286, according to [126]. Finally, XVH images were reconstructed using a Python script based on TIGRE library [134].

Following a thorough definition of the methodologies employed for the optimization of experimental parameters and the application of X-ray Virtual Histology to melanoma and non-small cell lung cancers, the subsequent chapters will present the results. Chapter 5 will showcase the outcomes of the optimization protocol for performing synchrotron-based XVH. Chapter 6 will explore the application of XVH for skin tumors and melanoma, with conventional histology as a reference. The findings from this investigation were then leveraged to develop a semantic segmentation model, the outcomes and performance of which are detailed in Chapter 7. Subsequently, Chapter 8 will present the correlative imaging of XVH and histopathology to discuss the invasive properties of NSCLC. Finally, Chapter 9 will display some preliminary results of the application of XVH to skin tissue in FFPE blocks using an X-ray laboratory source.

CHAPTER 5

Results - Optimization Of Synchrotron X-ray Virtual Histology

Propagation-Based Imaging (PBI) represents the most straightforward method for conducting X-ray phase-contrast imaging. It is essential to consider a number of variables when performing XPCT, with particular attention being paid to the analysis of soft tissue. Prior studies conducted at the SYRMEP beamline have concentrated on the optimization of setup parameters [135, 136], thereby providing a more comprehensive analysis than that presented here. However, that research did not address the specific case of skin or lung tissue. The objective of this chapter is to confirm the effectiveness of adapting the most commonly used acquisition protocols to the specific focus of this thesis through straightforward experiments.

This chapter provides an overview of the physical and experimental properties that have the greatest impact on the output of synchrotron-based X-ray virtual histology pipeline. To maximize the throughput through of the allocated beam time, continuous mode acquisition is usually employed. This is achieved by letting the rotator freely rotates while the detector captures a single shot per angle. Additionally, the white beam configuration is selected to increase photon statistics. Accordingly, the parameters typically adjusted by beamline users to optimize the overall image quality are the SDD, pixel size at the detector, and exposure time. However, reducing the pixel size may result in a smaller FOV, necessitating the determination of an optimal balance between pixel size and FOV to avoid an excessive number of scans.

Section 5.1 discusses the spatial resolution achieved using the selected synchrotron beamline. Section 5.2 compares two different embedding configurations for soft tissues, specifically storage in agar versus paraffin. Section 5.3 explores the optimal exposure time necessary for obtaining high-contrast images, while 5.4 evaluates the ideal orientation of the FFPE block to enhance image quality. Finally, 5.5 evaluates the most effective experimental setup, focusing on pixel size and sample-to-detector distance, aiming to improve image contrast.

5.1 Assessing Spatial Resolution Via Bar Pattern Phantom

The Micro-CT Bar Pattern NANO Phantom is used to assess the spatial resolution and imaging performance of the micro-CT system. The instrument allows for the

determination of the in-place and axial spatial resolution through the scanning of the vertical and the horizontal silicon chips, respectively. By inspecting the line profile graph, the intensity variations across alternating high-contrast bars provide insight into the system's ability to distinguish between small structures at varying spatial frequencies.

Given that the phantom sample was acquired at an SDD of 20 cm and at an effective pixel size of 2 µm, the edge enhancement effect has a significant impact on the reconstructed image. In this section, the vertical silicon chip was selected for the assessment of spatial resolution, as it is less susceptible to the effects of edge enhancement and photon starvation artifacts. Figure 5.1 is the coronal reconstructed slice, which depicts a section of the bar pattern observed in various orientations within the micro-CT phantom. The calibrated silicon bars thickness are respectively 2, 4, 6, 8, and 10 µm. Even if the slice has been reconstructed without applying any phase retrieval algorithm, the image and its plotted bar profile show visible effects of edge enhancement.

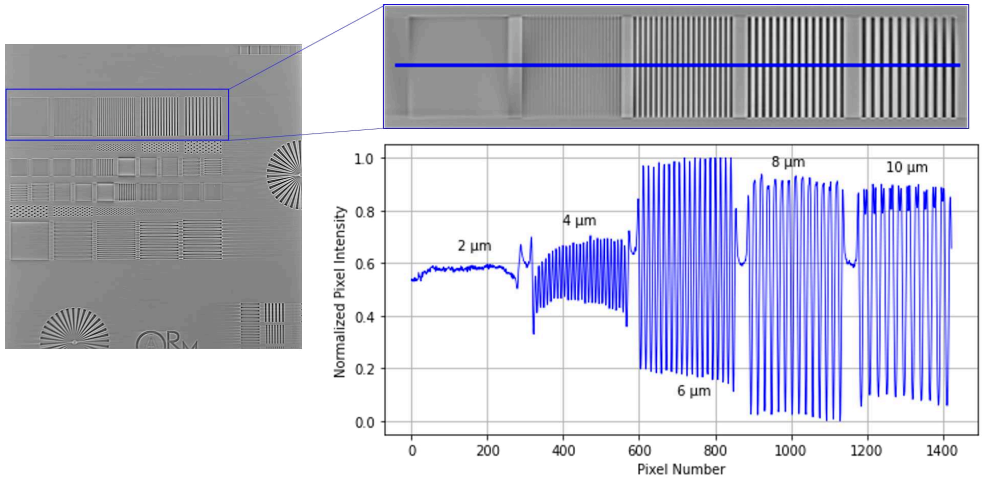

Figure 5.1. Micro-CT image of the Bar Pattern NANO Phantom, used to assess the spatial resolution of the micro-CT system. On the right, the reconstructed slice of the vertical silicon chip. On the left, the top panel displays the zoom of the bar pattern, while the bottom panel illustrates the line profile, which has been plotted to estimate the spatial resolution. The micro-CT phantom was acquired at the SYRMEP beamline of the Elettra synchrotron in parallel geometry, using the propagation-based setup with a polychromatic beam (average X-ray energy: 21 keV, pixel size: 2 µm, SDD: 20 cm).

The line profile analysis of the bar patterns from the micro-CT phantom demonstrates that the bar widths, which range from 4 µm to 10 µm, are distinctly discernible, exhibiting pronounced transitions between the peaks and valleys that represent the alternating high- and low-density regions. The visible peaks thus correspond to the system's effective ability to resolve the 4 µm to 10 µm bar patterns. However, the 2

µm bar pattern is not well-resolved, as indicated by the absence of distinct peaks and valleys in the line profile at this resolution, which can be considered a noise pattern. This indicates that the spatial resolution limit of the system precludes the accurate capture of structures at 2 µm, reflecting its inability to differentiate such fine details. In conclusion, the spatial resolution can be reasonably quantified to be between 4 and 6 µm.

5.2 Evaluation Of Specimen Assessability In Agar And Paraffin

Two configurations were considered in order to determine the optimal embedded media for soft tissues in terms of image clarity. Figure 5.2 depicts the outcome of scanning a skin tissue embedded in agar.

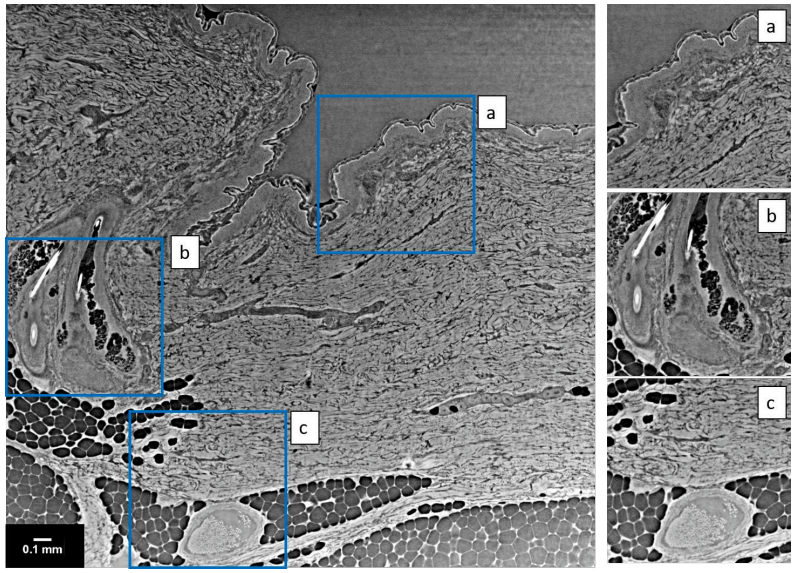

Figure 5.2. Skin tissue embedded in agar and considered for XPCT investigation at the SYRMEP beamline of the Elettra synchrotron. On the left, some zoomed details representing (a) a epidermal-dermal layer junction, (b) a pilosebaceous unit within dermis, and (c) hypodermal layer with a blood vessel. The experiment was conducted in parallel geometry, using the propagation-based setup with a polychromatic beam (average X-ray energy: 21 keV, pixel size: 2.0 µm, SDD: 20 cm).

Given that agar is transparent to X-rays, the effect of phase contrast imaging appears to facilitate the detection of subtle differences between the tissue and the surrounding medium, which can be discerned visually. It is probable that fine struc-

tural details, including individual skin layers (epidermis, dermis), collagen fibers and potentially even cellular details, will be discernible. To exemplify, Figure 5.2(a) illustrates the upper layers of the skin, including the epidermis and dermis. Figure 5.2(b) provides a detailed representation of the pilosebaceous unit, while Figure 5.2(c) demonstrates the high visibility of a blood vessel surrounded by fat tissue in the hypodermis layer.

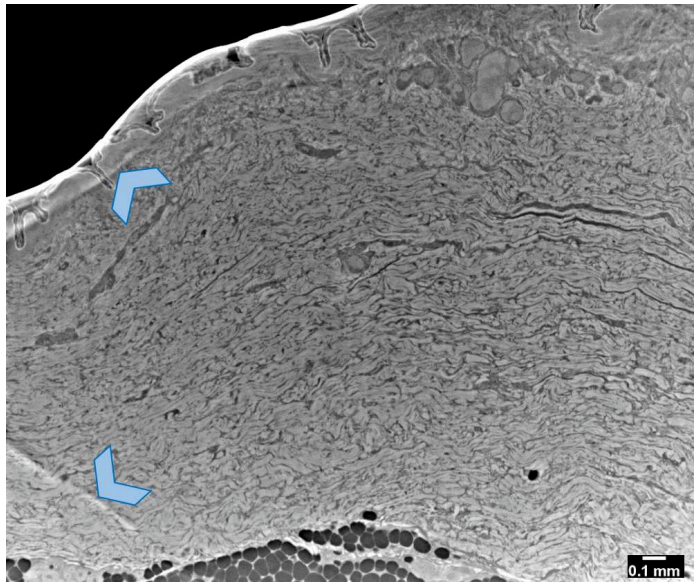

Figure 5.3. The formation of an air bubble is visible as a dark area above the external layer of the embedded tissue in agar. This is attributed to the X-ray exposure of the agar medium. Light blue arrows point at the artifacts induced by the high difference in refractive index. The experiment was conducted in parallel geometry, using the propagation-based setup available at the SYRMEP beamline (Elettra synchrotron of Trieste, Italy). Further experimental details: polychromatic beam, 21 keV average X-ray energy, 2.0 µm pixel size, 20 cm SDD.

In contrast, Figure 5.3 illustrates an alternative skin tissue embedded in agar medium, which exhibited the formation of a substantial air bubble during the scanning process. The presence of the air bubble results in the formation of high-contrast artifacts, which manifest as a bright layer of material on the edge of the skin tissue. Furthermore, the presence of this artifact has an impact on the visibility of the upper layer of the skin, as well as on image clarity, resulting in the appearance of white streaks. A further potential issue is that the formation of an air bubble during X-ray exposure could expand and cause movement of the sample during scanning, resulting in the creation of irreparable artifacts.

The second configuration utilizes a formalin-fixed, paraffin-embedded (FFPE) block, which is a common method for the storage of tissue in clinical practice. Figure

5.4 depicts this configuration. With regard to Figure 5.2, it is evident that all layers of the skin, from the epidermis to the hypodermis and including the dermis, are readily discernible and assessable in Figure 5.4.

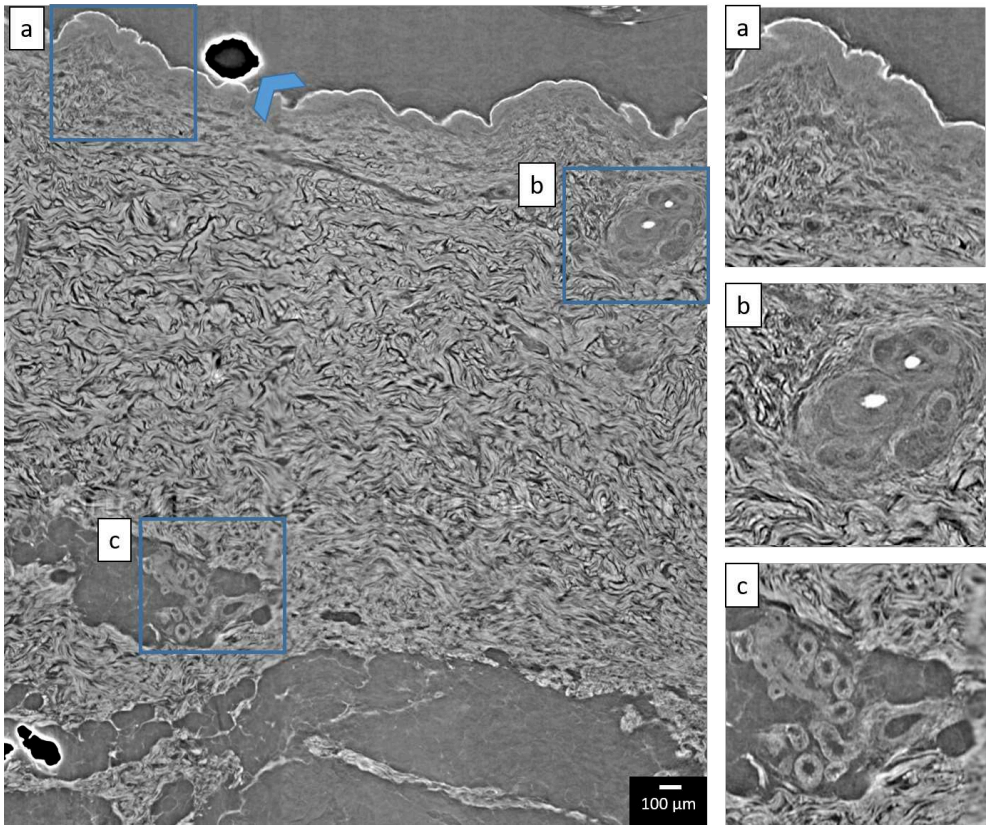

Figure 5.4. Skin tissue embedded in paraffin block and considered for XPCT investigation at the SYRMEP beamline of the Elettra synchrotron (Trieste, Italy). On the right, some zoomed details representing (a) epidermal-dermal layer junction, (b) hair follicle within dermis, (c) hypodermal layer with a blood vessel circumscribed by sweat glands. The experiment was conducted in parallel geometry, using the propagation-based setup available (polychromatic beam, average X-ray energy: 21 keV, pixel size: 2.0 µm, SDD: 20 cm).

The image presents a pronounced contrast between the tissue and the surrounding paraffin, thereby rendering the characteristics of the skin with remarkable clarity. As an example, Figure 5.4(a) demonstrates that XPCT is capable of characterizing the stratum corneum of the epidermis, which is represented as a white line above the overall skin tissue. Furthermore, the stratum basale is marked as a thin edge line between the constant light grey of the epidermis layers and the dermal tissue, while the dense composition of connective tissue represents the dermal layer. As Figure

5.4(b) provides a detailed examination of hair follicles and sebaceous glands, Figure 5.4(c) illustrates adipose tissue, sweat glands, and a nearby blood vessel.

Figure 5.4 depicts the presence of two minor air bubble artifacts. These are not a consequence of the interaction with X-rays; rather, they are the result of the preparation of the sample, despite the process of embedding tissues in paraffin reducing the likelihood of the inclusion of air bubbles.

As illustrated in Figure 5.3, the presence of air bubbles in the sample results in the generation of high-contrast artifacts when X-rays are used for imaging. Nevertheless, their impact within imaged FFPE blocks is not as pronounced as that observed in the previous configuration.

5.3 Effect Of Exposure Time

The same region of a neuroendocrine tissue was scanned by means of XPCT at three increasing exposure times (e.g., 50 ms, 100 ms, 200 ms), and the results are presented in Figure 5.5.

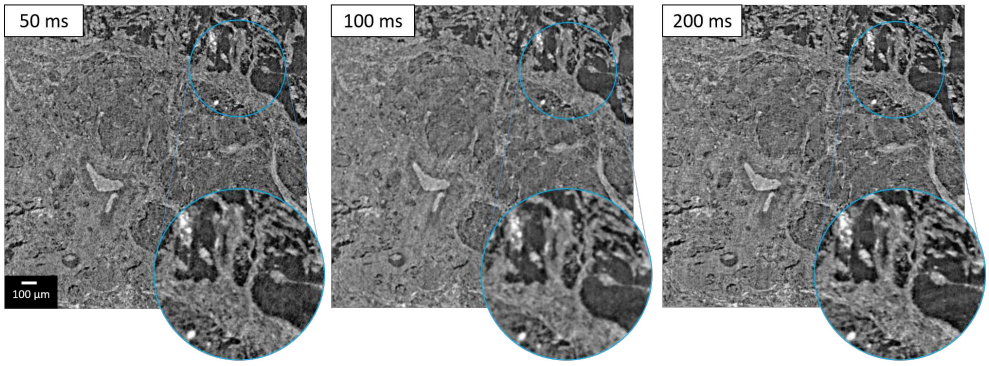

Figure 5.5. Effect of exposure time to X-ray Virtual Histology images of a neuroendocrine tissue. The same tissue was acquired in parallel geometry at the SYRMEP beamline of Elettra synchrotron (Trieste, Italy) employing the white beam configuration at 2.0 µm pixel size, 20 cm SDD, average X-ray energy 21 keV, and in continuous mode.

Although the images may appear to have the same quality to the human eye, the image acquired at 50 ms is the most affected by noise. This manifests as graininess due to the limited amount of X-ray photons reaching the detector. This results in the reduction in image clarity, contrast, and in the ability to detect and discriminate small or subtle features, such as small cells or other abnormalities. Conversely, an increase in exposure time in an XPCT experiment results in a greater distinction between healthy and pathological tissue, thereby facilitating enhanced visualization and more precise identification. However, an excessive exposure time might lead to

a non-linear or, even, saturated detector response in a few pixels, thus leading to the formation of ring artifacts.

In order to determine the optimal images for use in the segmentation phase, the contrast-to-noise ratio (CNR) was calculated for the images displayed in Figure 5.5. The CNR is a crucial measure of the distinguishability between different tissue types or areas of interest, such as tumors, stroma, healtly parenchyma, and clots.

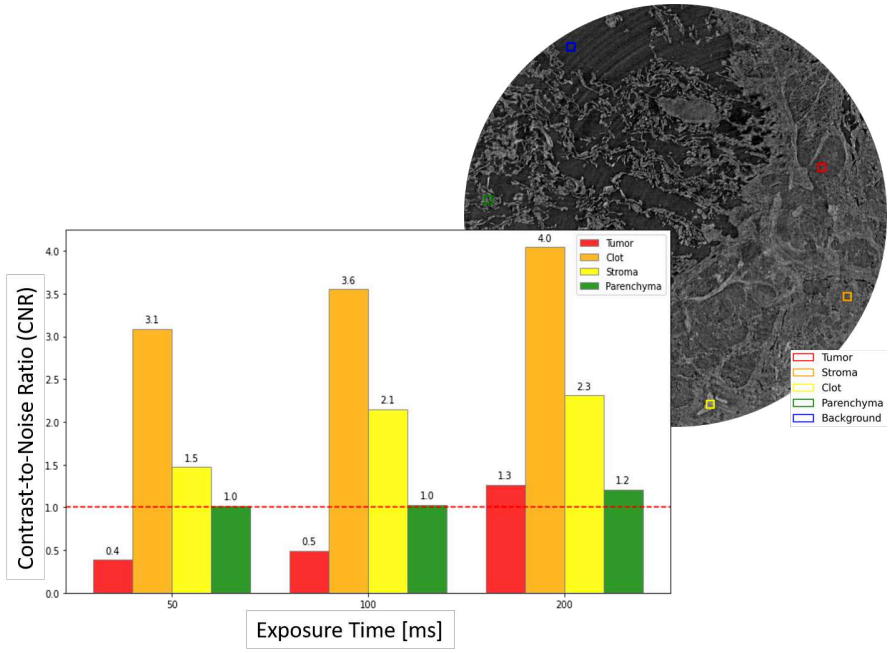

Figure 5.6. Contrast-to-noise ratio (CNR) calculated on the neuroendocrine neoplasm tumor (here referred as tumor), the stroma, the blood clot, and healthy parenchyma, considering paraffin background considered as reference.

In all cases depicted in Figure 5.6, as the exposure time is increased, the contrast-to-noise ratio (CNR) for these regions and the overall image quality improve, thereby enhancing the detectability of subtle differences in density or composition. While the stroma and blood clot demonstrate favourable CNR values across all experimental scenarios, the neoplasm exhibits a CNR value below unity in the experiment conducted with an exposure time of 50 ms. A reduction in CNR results in the obscuration of fine details of the tumor, which then resemble the paraffin background. This makes the segmentation of such structures a challenging process, as it is difficult to distinguish between the tumor's different structures or tissue types and the background. Moreover, an increase in exposure time has a direct impact on the visibility of neuroendocrine tumors, resulting in a gain in CNR values of three times the lowest exposure time when the exposure time is doubled.

Employing the synchrotron-based XPCT setup, higher exposure times for projection in continuous acquisition mode correspond to higher values of CNR. This helps in revealing details that would otherwise be obscured in images of lower quality or contrast. On the contrary, longer exposures can cause the saturation of some pixels, leading to the formation of ring artifacts, thereby reducing image quality. In order to facilitate image segmentation, it is necessary to enhance tissue contrast and improve the effectiveness of edge detection. This should be done while paying attention to saturated pixels and, if necessary, employing a ring artifacts removal filter.

5.4 Effect Of Sample Orientation

As presented in Figure 4.3 of Chapter 4, the biocassettes employed in the clinical context are constituted by a plastic base with a block of paraffin containing the tissue. The plastic box has standard measures, and in the case of the smallest one is $4 \times 3 \times 0.5$ cm long, wide, and deep. With the paraffin block on top, the FFPE block can achieve typically a 1 cm depth, as illustrated in Figure 5.7(a). In consideration of this particular anisotropy size, a critical evaluation of the ideal scanning position is imperative. The necessity of this assessment is substantiated by the literature [137],

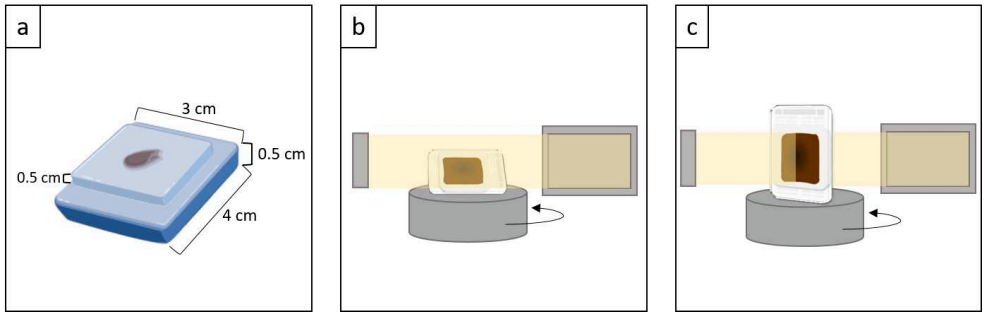

Figure 5.7. (a) Size of a typical FFPE block employed in clinical practice for biopsies. Then, a schematized XPCT setup, with an X-ray source on the left and the detector on the right, is represented with the same FFPE block considered both in horizontal (b) and vertical (c) orientations.

which describes attempts at various positions, including laminography, which is not a focus of this study. The objective is to distinguish between the two positions, designated as horizontal and vertical. In the horizontal position, as illustrated in Figure 5.7(b), the X-ray beam has to cross the sample in its most demanding size, which are the width (3 cm) and the length (4 cm). In contrast, employing the vertical configuration in Figure 5.7(c), the worst case scenario considers the width (3 cm) and depth (1 cm) of the sample. This is evident even considering the maximum sample thickness to be accommodated, which is the diagonal between these two sizes. In the horizontal scenario, this is the diagonal between the width and length of the sample,

while, in the vertical one, it is the diagonal between the width and the depth. As expressed in Table 5.1, the maximum sample thickness in the vertical orientation of the sample is less than that of the horizontal configuration. These findings have implications for photon starvation and the potential for artifacts in reconstruction. Moreover, the use of synchrotron light and PBI allows for an equal pixel size in all three directions, thereby enabling the evaluation of different sample placements on the rotator. After all these considerations, the same FFPE block was scanned via

	Horizontal Orientation	**Vertical Orientation**
Exposed Area	4.0×3.0 cm^2	3.0×1.0 cm^2
Maximum Thickness	5.0 cm	3.2 cm

Table 5.1. The measurements about the axial area and the maximum thickness of the sample that has to be traversed by the X-ray beam during the XPCT acquisition. The computations are derived based on the assumption that a typical FFPE block is irradiated in two distinct orientation positions: horizontal and vertical. The dimensions of the FFPE block are obtained from Figure 5.7(a).

XPCT in both vertical and horizontal orientations employing the same acquisition and reconstruction parameters. Results are illustrated in Figure 5.8 to visually assess the optimal configuration for image quality.

The two images in Figure 5.8(a) and 5.8(c) depict the same region, in which a blood vessel is visible surrounded by acinar pattern adenocarcinoma. The images in Figure 5.8(a) and 5.8(e) represents the reconstructed slice produced by the application of the horizontal configuration as in Figure 5.7(b). In contrast, the images in Figure 5.8(c) and 5.8(f) obtained by the employment of the vertical configuration (Figure 5.7(a)) is the result of the reorientation of the reconstructed slice along a plane parallel to the histological cutting. This indicates that these images were subjected to reslicing along the Z-axis for the purpose of visualizing their coronal section, which is consistent with the histological plane. The visual comparison of the two images reveals that the Figure 5.8(d) produced by the vertical configuration is more sharply delineated than that of Figure 5.8(b), thereby rendering the details more discernible and appreciable. To provide further clarification, the membranes of the glandular formations that are characteristic of the acinar pattern of the vertical configuration are more clearly delineated in comparison to those of the horizontal configuration. Furthermore, the horizontal configuration is more susceptible to beam hardening and scattering due to the intense density of the paraffin block. Additionally, the high absorptive materials present within the FFPE block, including the cartilage of the bronchi in Figure 5.8.(a) and 5.8(c), have the potential to induce significant artifacts due to photon starvation and beam hardening.

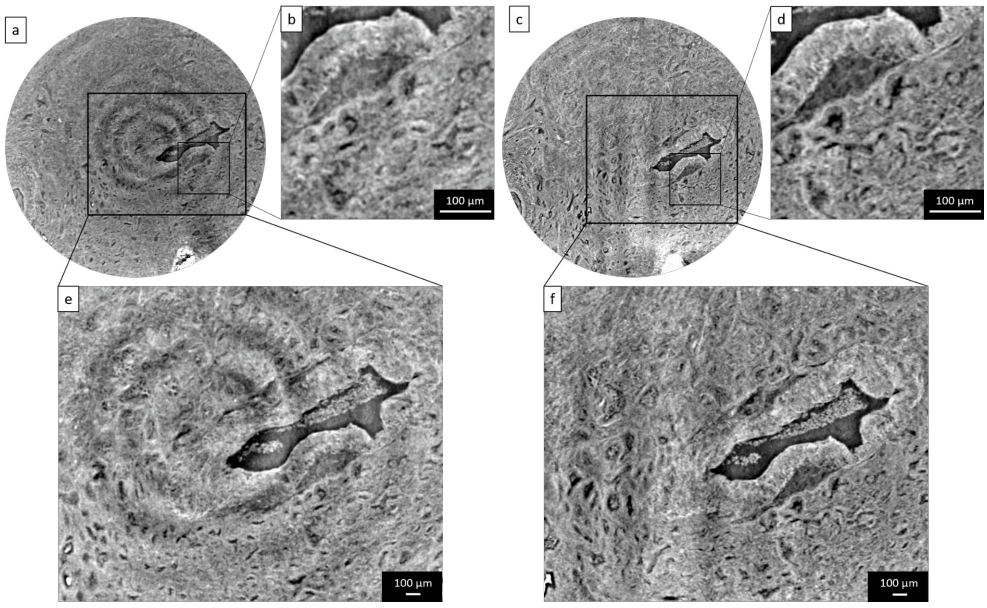

Figure 5.8. FFPE block investigated via XPCT both in horizontal (left) and vertical (right) orientations. The vertical configuration yields axial reconstructed slices that necessitate Z-reslicing for visualization of the coronal section, as depicted in (c), (d) and (f). This is essential for alignment with the histological sectioning plane. In contrast, the horizontal configuration directly produces the reconstructed image in (a), (b) and (e), as it represents the axial section of the sample. The FFPE block was acquired at the SYRMEP beamline of Elettra synchrotron (Trieste, Italy) employing the white beam configuration at 2.0 µm pixel size, 20 cm SDD, and average X-ray energy 21 keV.

5.5 Effect Of Pixel Size And Distances

Considering constant the δ over β ratio, the effect of the phase retrieval algorithm is modulated by three parameters: pixel size, sample-to-detector distance (SDD), and the average energy of the polychromatic X-ray spectrum. In this section, the impact of varying the SDD and pixel size was evaluated while maintaining a consistent mean number of counts per pixel across all configurations.

Figure 5.9, which considers a detail of an adenocarcinoma that has grown in proximity to a vein with a blood clot, can be interpreted in two ways. Firstly, it can be read horizontally to gain insight into the impact of distance at a fixed pixel size. Secondly, it can be read vertically to understand the influence of pixel size at a constant SDD.

The first key proposes that increasing the SDD at the same pixel size leads to less-defined borders and the appearance of black-white fringes between different materials. Furthermore, a greater distance also enhances contrast, thereby making low-

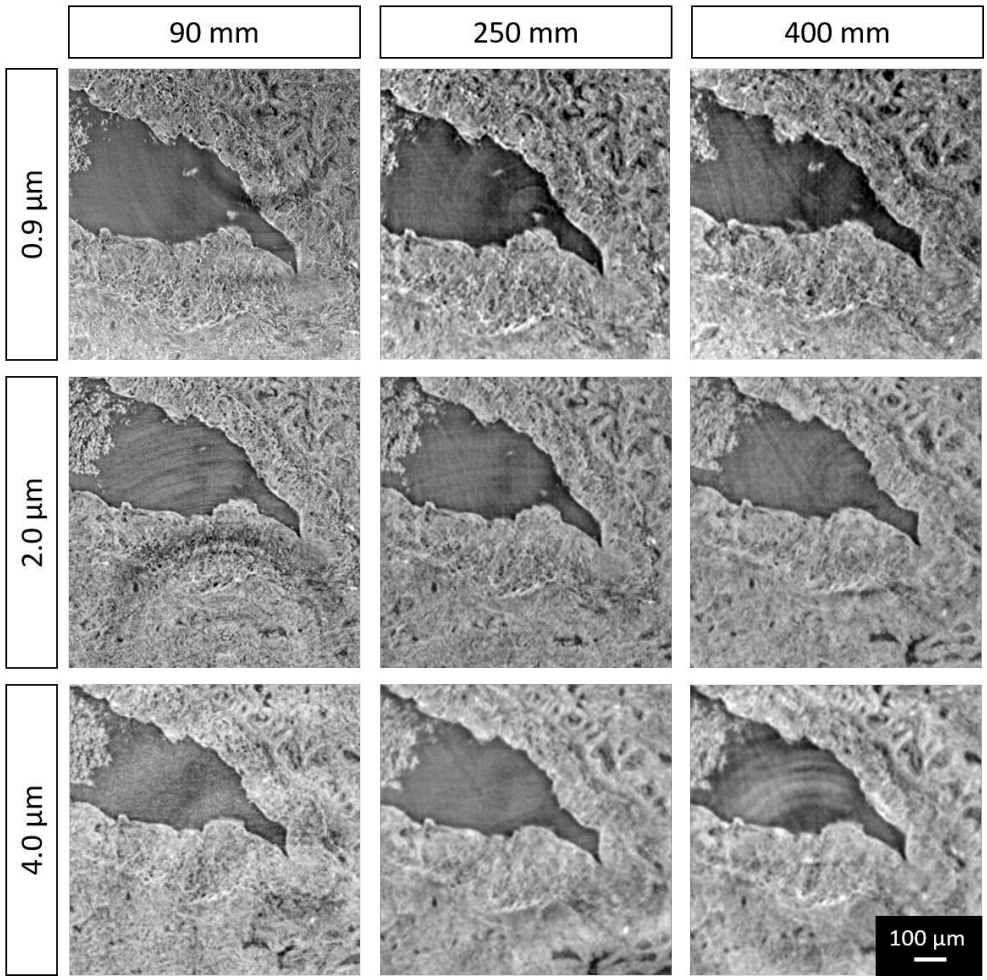

Figure 5.9. XVH images extracted from data acquired at varying sample-to-detector distances (e.g., 90 mm, 250 mm, and 400 mm), and at disparate pixel sizes (e.g., 0.9 µm, 2.0 µm, and 4.0 µm). A similar mean number of counts per pixel across all configurations was ensured by modifying the experimental parameters of exposure time and beam filtering, to guarantee a consistent photon flux per unit area despite the expansion of the field of view and the concomitant increase in pixel size. The FFPE block was acquired at the SYRMEP beamline of the Elettra synchrotron (Trieste, Italy) employing the white beam configuration.

absorption features and high-phase difference characteristics more visible. However, at very long distances (e.g., SDD 400 mm), excessive diffraction can result in image blurring when imaging at a small pixel size (e.g., 0.9 µm). Conversely, images captured at shorter distances exhibit greater sharpness but also reduced phase contrast and, in some cases, noise. This makes it more challenging to discern subtle refractive index variations and gives the image a greater resemblance to one of greater absorption.

Furthermore, the image can be analyzed vertically in order to observe the effect of different pixel sizes at the same distance. The use of smaller pixel sizes allows for more accurate phase contrast and the capture of intricate structures. However, this approach can also result in an increase in noise and necessitates more precise alignment and computational resources. Conversely, larger pixel sizes result in the smoothing out of subtle phase or absorption contrast variations, which is beneficial for imaging larger features but less effective for resolving fine details. Indeed, when the pixel size is fixed at 0.9 µm, the image acquired at the SDD of 90 mm exhibits greater detail and sharpness. As the distance between the object and the detector increases, the phase contrast effects become more pronounced, leading to an enhancement in image contrast. At a pixel size of 2.0 µm and an SDD of 90 mm, the image is sharp and noisy, while the image acquired at 400 mm is too smoothed. The image at 2.0 µm pixel size and 250 mm SDD represents an optimal compromise. When the pixel size is set to 4.0 µm, the image collected at the SDD of 90 mm is affected by noise, while that acquired at the SDD of 250 mm requires greater contrast. Notwithstanding the presence of a ring artifact that diminishes image quality, the image acquired at the SDD of 400 mm exhibits slighty enhanced contrast compared to the previously considered images.

The practical considerations reported in this chapter contribute to the definition of a reasonably optimal experimental configuration for X-ray virtual histology with the available hardware, with a focus on the enhancement of the overall image quality. As further explained, the ability to automatically segment the reconstructed images is the key aspect to be privileged when proposing a trade-off among image quality parameters (resolution, contrast, noise, and artifacts).

In the following chapter, the results presented above are used to explore one of the most intriguing biological applications of X-ray virtual histology in this thesis: the detailed analysis of skin tumors and melanoma. This provides deeper insights into the structure and pathology of these types of diseases.

CHAPTER 6

Results - Correlative Imaging Of Skin Tumors Via Synchrotron-Based X-ray Virtual Histology And Conventional Histology

This chapter explores the application of X-ray virtual histology in the study of skin tumors, with a particular focus on melanoma. Through correlative imaging techniques, this chapter will examine the most intriguing aspects of skin tumor morphology, highlighting how the integration of 3D imaging and traditional histology enhances our understanding of these lesions. The combination of high-resolution two-dimensional histological data with 3D XPCT imaging enables a comprehensive understanding of tumor morphology, spatial relationships, and microarchitectural features in intact tissue samples. All XPCT data were performed employing the PBI setup available at the SYRMEP beamline of the Elettra synchrotron (Trieste, Italy). The acquisitions were conducted in white beam (average X-ray energy: 21 keV), at an SDD of 20 cm and with an effective pixel size of 2 µm. All histologies reported in this chapter were scanned at a 0.25 µm pixel size resolution (×200 magnification).

6.1 Nevus And Seborrheic Keratosis

Two benign conditions of the skin, which are seborrheic keratosis and nevus, are reported in Figure 6.1. They are presented together as they have been frequently observed in clinical inspection, suggesting a correlation between the two lesions [138].

A nevus, or mole, is a benign neoplasm that arises from the proliferation of melanocytes. In most cases, it manifests as a circumscribed lesion in the epidermal layer, exhibiting uniformity in size and shape. Melanocytes organize in clusters, also referred to as nests, which are located at the dermo-epidermal junction and within the dermis. These nests form a central raised area, as illustrated in Figures 6.1(a), 6.1(d), and in Figures 6.1(b), 6.1(e). Although individual melanocytes are not discernible by XPCT, the melanocytic nests are visible as a dense uniform cellular pattern with a circular or ovoid shape circumscribed by junctional nests. The nevus case illustrated in Figures 6.1(a) and 6.1(d) facilitates the detection of such elements in XPCT images due to their high density and limited dimensions. In contrast, the histological image

in Figures 6.1(b) and 6.1(e) depicts extensive dense clusters of melanocytes, which appear as a compact solid pattern in the XPCT image. In both instances, the dermal architecture exhibits regular and demarcated epidermal layers, as well as a structured dermis. Moreover, seborrheic keratosis-like changes and more pigmented regions are frequently observed.

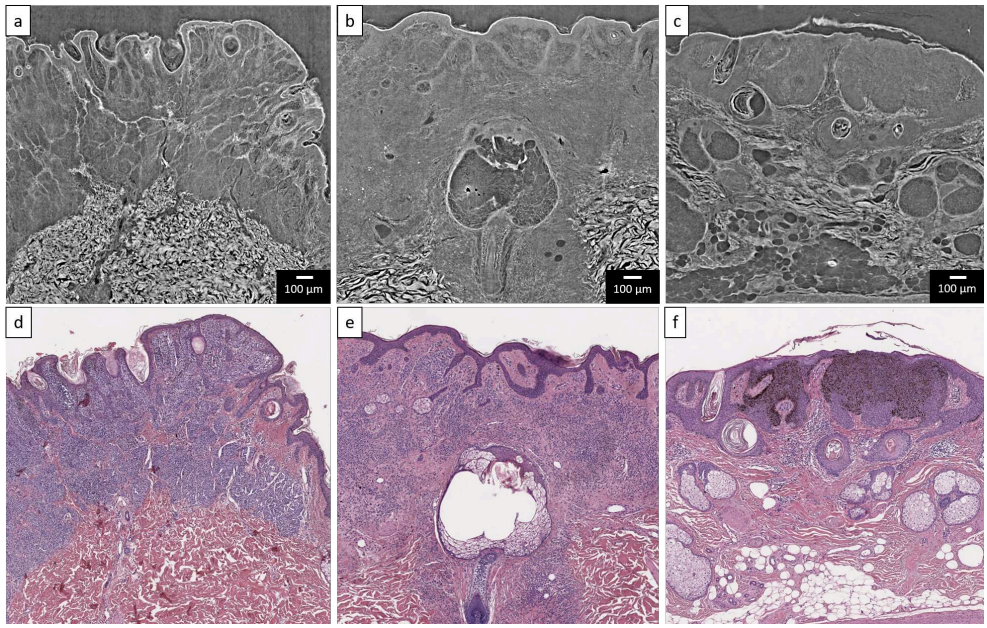

Figure 6.1. Correlative imaging of X-ray virtual histology and traditional histology of two benign lesions of the skin, thus nevi (a) and (d), (b) and (e) and a seborrheic keratoses (c) and (f). Experimental XPCT data: white beam, average X-ray energy: 21 keV, SDD: 20 cm, and effective pixel size: 2 µm. Histological information: H&E staining, ×200 magnification, 0.25 µm pixel size.

Seborrheic keratoses are common, pigmented, and benign skin conditions characterized by non-cancerous growths on the surface of the skin. Although seborrheic keratoses are tipically associated to a good overall prognosis, the large presence of this type of lesions can complicate the detection of other malignant skin lesions during the dermoscopic examination. This because seborrheic keratosis consists of a proliferation of basaloid epithelial cells that leads to a thickened epidermis, as appreciable in Figures 6.1(c) and 6.1(f). From the XPCT perspective, seborrheic keratoses are represented as a compact and well-defined proliferation of epidermal keranocytes, which form irregular and thicked structures. The void inside the keratin-filled cyst testifies how this element has well defined boundaries from the rest of epidermis. Keratin-based cysts are often present in benign melanocytic lesions, as reported in Figures 6.1(a) and 6.1(d). They maintain the basal layer of the epidermis intact,

growing slowly and irregularly inside the epidermal layer. These aspects emphasize not only the clear distinction between the benign tumor and the epidermis, but also its condition and distinction from other malignant lesions such as melanoma.

6.2 Basal Cell Carcinoma

Basal Cell Carcinoma (BCC) represents the most prevalent form of non-melanoma skin cancer. Figure 6.2 illustrates the correlative imaging of a basal cell carcinoma lesion.

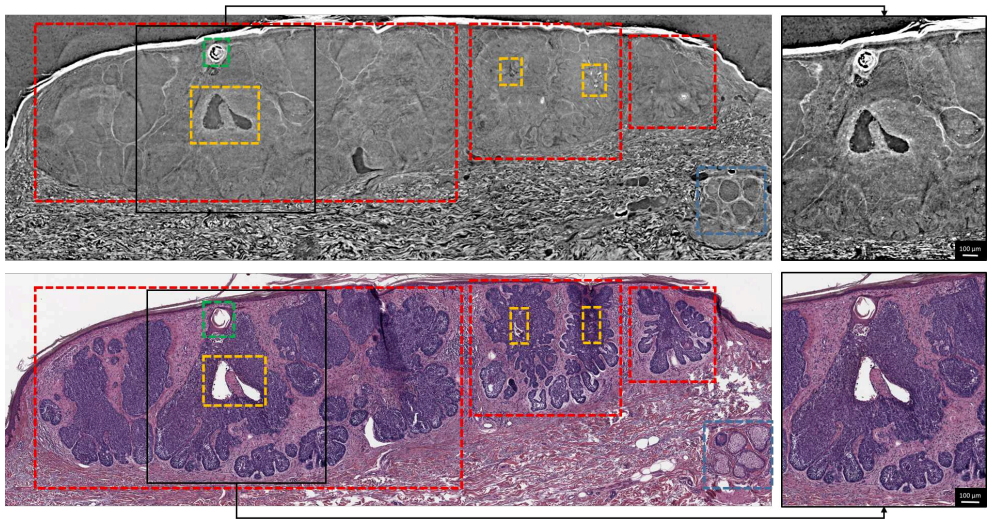

Figure 6.2. XVH and histological images of a basal cell carcinoma. Red areas, clusters of basaloid cells; yellow areas, central necrosis; green areas, seborrheic keratosis; blue areas, pilus glands. Experimental XPCT data: white beam, average X-ray energy: 21 keV, SDD: 20 cm, and effective pixel size: 2 µm. Histological information: H&E staining, ×200 magnification, 0.25 µm pixel size.

The red panels serve to highlight the presence of large nodular basaloid lobules with peripheral nuclear palisade development in the dermal layer. Such nodular clusters typically exhibit vertical growth, forming a compact structure derived from the basal cells of the epidermal layer. In this instance, the solid nodules are confined to the papillary dermis. However, they have the potential to become locally invasive, spreading and destroying the surrounding skin layers, tissues, and bones. Additionally, XPCT is capable of discerning the formation of central cysts, resulting from excessive mucin production, and the subsequent central necrosis, as evidenced by the yellow dotted panels. Such characteristics are frequently documented in the case description, along with details regarding the tumor size and the presence of lymphovascular invasion [139]. Furthermore, XPCT is able to identify seborrheic keratoses

originating within the lesion, as indicated by the green dotted regions. The panel on the left of Figure 6.2 illustrates the high-resolution appearance of some solid basaloid clusters. On closer examination, the XPCT technique is shown to be capable of detecting the peripheral borderline cell layers and the peritumoral clefting surrounding these nodules, thereby providing contrast to the borders of the tumor. Although XPCT is unable to discern individual basaloid cells, it can discern the morphological structure of such tumors. However, in the peripheral regions of these nodules, which are the least dense due to their slow growth, it is possible to discern the internal arrangement of basaloid cells as the tumor gradually dissolves collagen to expand through the dermis.

6.3 Melanoma

Melanoma can manifest in a variety of histological forms, even among cases within the same category. Figure 6.3 illustrates the diverse typology of melanoma histological characteristics.

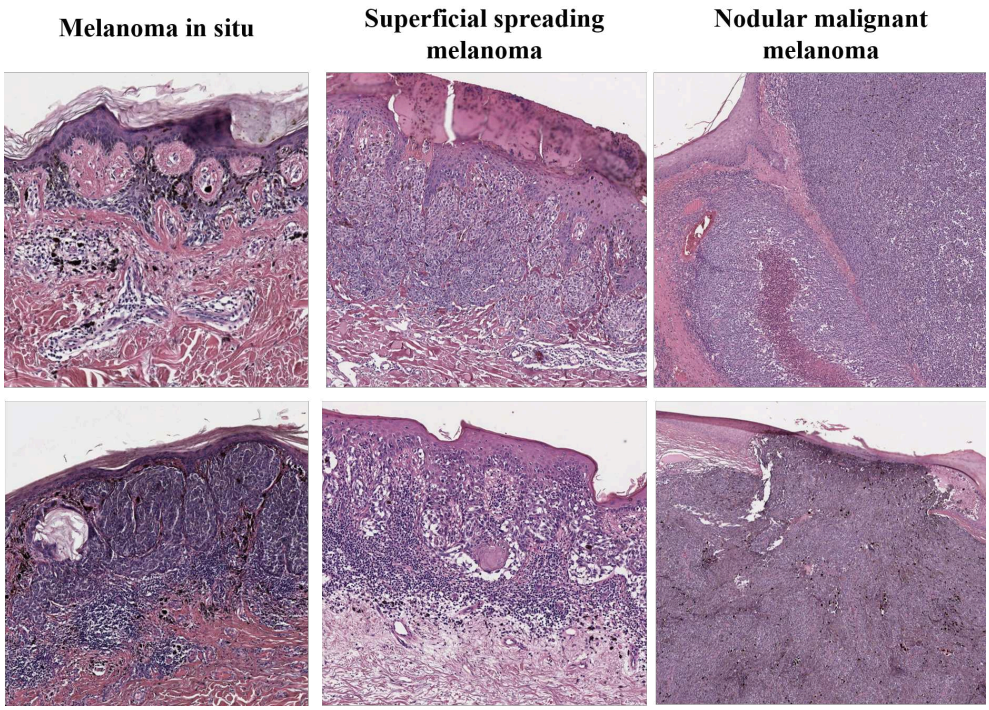

Figure 6.3. Histological images representing three types of melanoma: (left) melanoma in situ, (center) superficial spreading melanoma, and (right) nodular malignant melanoma. Histological information: H&E staining, ×200 magnification, 0.25 µm pixel size.

Some recurring patterns are discernible in all cases, including the formation of nested melanoma. The latter is visible as a purple dense clusters of atypical melanocytes. In contrast, other characteristics can serve to distinguish between the superficial spreading and the nodular type. Although the diagnosis necessitates a comprehensive visualization of the entire lesion at both cellular and macroscopic levels of resolution, as illustrated in [140], this study presents three types of melanoma, ordered by level of invasiveness, with a particular focus on the most intriguing aspect of the lesion.

6.3.1 Melanoma In Situ

Melanoma in situ represents stage 0 of melanoma, as the proliferation of neoplastic melanocytes is limited to the epidermal layer, which is the most external layer of the skin. As reported in [141], the criteria for histogical diagnosis of melanoma in situ include poor circumscription and asymmetry, as well as the predominance of individual melanocytes over nests. The case presented in Figure 6.4, which illustrates in the correlative imaging between XPCT (above panels) and histology (below panels), suggests the confirmation of the aforementioned criteria.

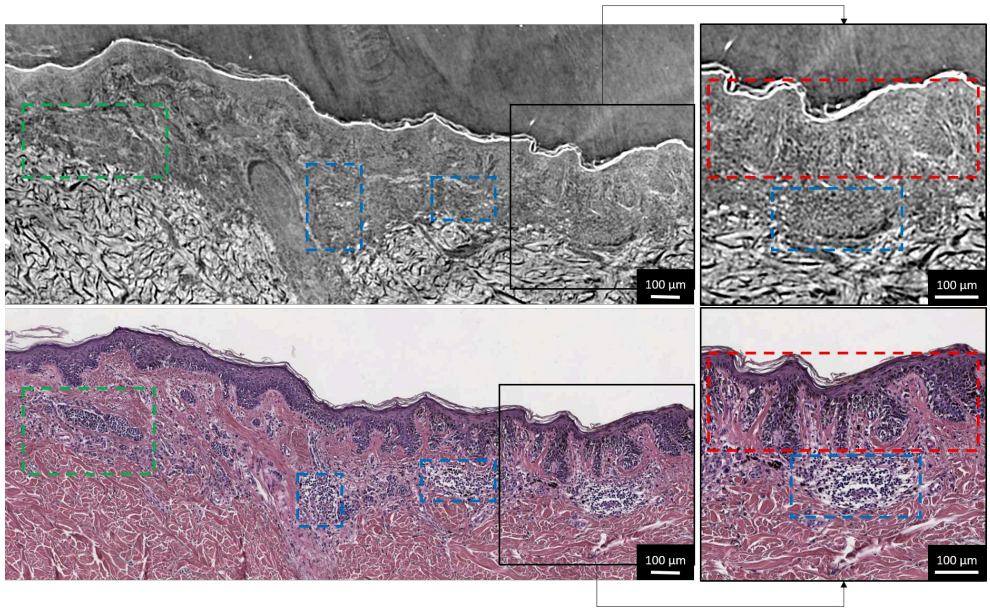

Figure 6.4. Correlative imaging techniques, namely X-ray phase-contrast tomography and histology, to examine a case of melanoma in situ. The green dotted area represents a group of benign melanocytes, the blue ones represent the lymphocytic infiltrate, and the red one outlines the area in which atypical melanocytes are present in the epidermis. Experimental XPCT data: white beam, average X-ray energy: 21 keV, SDD: 20 cm, and effective pixel size: 2 µm. Histological information: H&E staining, ×200 magnification, 0.25 µm pixel size.

Despite the absence of regular tissue organization, the dermoepidermal junction remains discernible, even in the presence of malignant melanocytes that are confluent and growing along it. The dermoepidermal junction is identifiable as the border between the epidermal (purple) and dermal (pink) layers in histology. In the XPCT image, this is discernible as an irregular white line bordering the epidermal layer. The light grey areas beneath the epidermis can be attribute to the presence of benign melanocytic (green dotted area) and lymphocytic (blue dotted area) cells. The occurrence of benign nested melanocytes can be attributed to the pre-existent nevus that subsequently developed into a melanoma, while the presence of a lymphocytic infiltration indicates the progression of the disease, whereby the expansion of atypical melanocytes is being restricted.

Additionally, the consumption of the epidermis is the result of the variability in shape and size of melanocytic nests and pagetoid scatter, which is defined as solitary and small groups of melanocytes situated in the superficial layers of the epidermis. These elements are illustrated in the red dotted panel of Figure 6.4.

6.3.2 Superficial Spreading Melanoma

Superficial spreading melanoma (SSM) is the most prevalent invasive variant, characterized by radial growth rather than vertical proliferation.

In its early stages, the disease is regarded as being in situ, which means it is confined to the epidermis. However, when malignant cells disseminate into dermal tissue, it is considered invasive. The penetration of dermis tissue by neoplastic invasion results in the development of a potentially aggressive form of skin cancer.

The differentiation between SSM and melanoma in situ represents a pivotal stage in the comprehension of the potential for progression. While melanoma in situ displays atypia and architectural disorder but does not breach the basement membrane, the lesion of an SSM is characterized by the presence of atypical melanocytes that have passed the epidermal-dermal junction, invading the dermis.

The histological features of SSM, as illustrated in Figure 6.5 by the red panels, include the presence of a pagetoid scatter of atypical melanocytes within the epidermis, as well as the diffusion of nested melanoma into the dermis. The pagetoid infiltration of the epidermis by melanocytes is readily discernible through the XVH technique, as illustrated in Figures 6.5(a) and 6.5(b). This is because these cells are often larger and more atypical than normal cells, as shown in Figures 6.5(c) and 6.5(d), exhibiting a propensity to diffuse along the basal layer of the epidermis. Moreover, the distinctive pleomorphism of neoplastic cells can be revealed by XVH imaging, thus enabling the precise detection of their spatial distribution in the tissue. Actually, melanoma nests can also be readily identified, despite the difficulty in distinguishing each malignant melanocyte within them.

In some areas indicated by the blue panels, clusters of lymphocytic infiltrates can be observed bordering the lesion, which appears to limit its diffusion. This is a consequence of the immune reaction of the host, which is a favourable prognostic

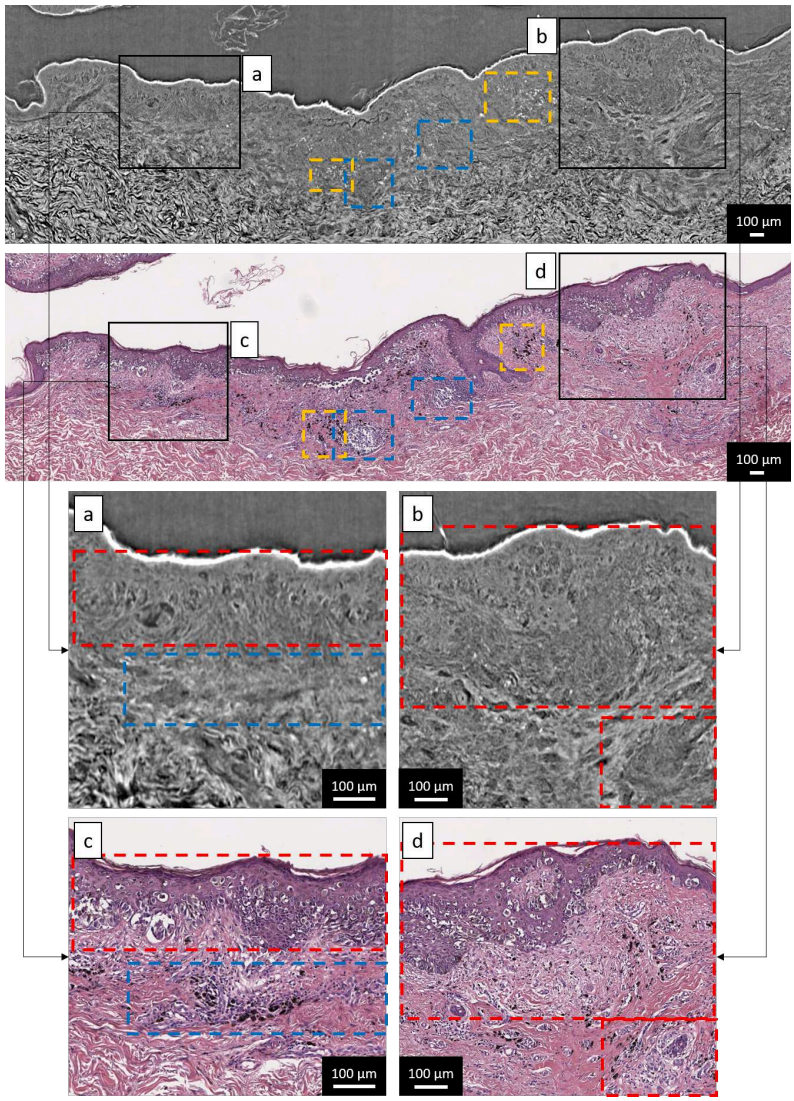

Figure 6.5. X-ray virtual histology and conventional histology images of a superficial spreading melanoma. The upper panels present an overview of the melanocytic lesion, while the lower panels, (a)(c) and (b)(d), provide a high-resolution image of the pagetoid diffusion and nests of atypical melanocytes. Experimental XPCT data: white beam, average X-ray energy: 21 keV, SDD: 20 cm, and effective pixel size: 2 µm. Histological information: H&E staining, ×200 magnification, 0.25 µm pixel size.

factor in predicting patient outcomes [142]. Finally, ulceration is sometimes present in SSM. As an adverse prognostic factor, the presence of ulceration, with identification of the exact position of loss of epidermis, leads to a more severe stage. In Figure 6.6, another case of SSM is reported zooming on the ulceration part.

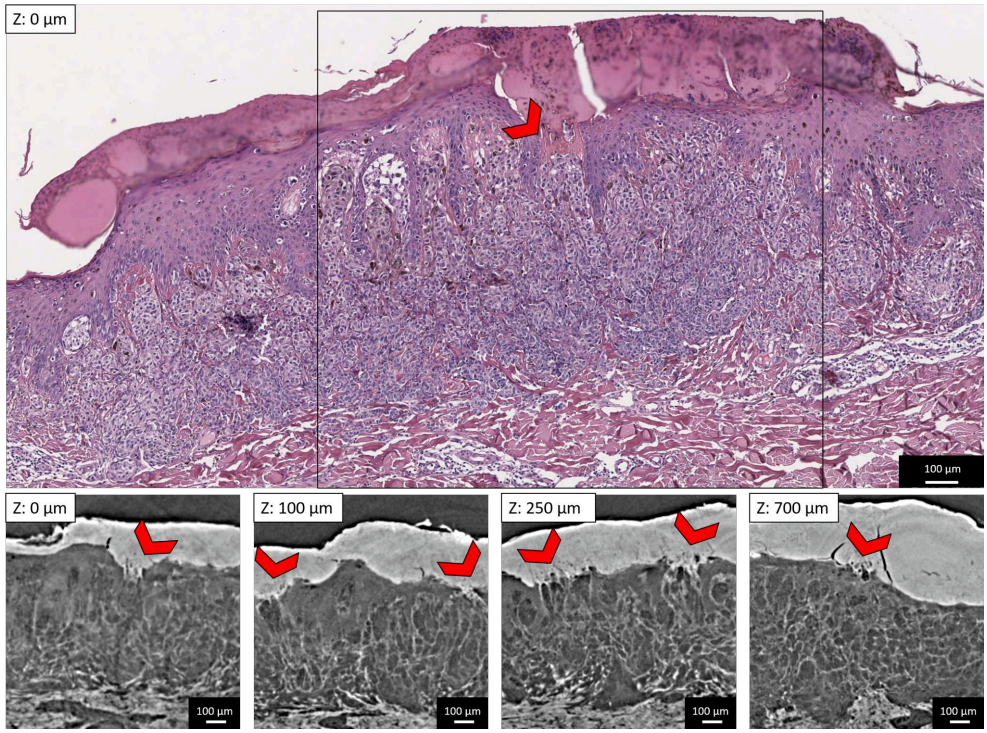

Figure 6.6. The images displayed are those of a close-up of an ulcerated superficial spreading melanoma. The top panel presents a histological image of the ulcerated melanocytic lesion, while the bottom panels show consecutive XVH-based images which present the loss of intactness of the epidermis at different levels of depth inside the FFPE block. These levels are 100 µm, 250 µm, and 700 µm from the level of the histological section which is considered to be the 0 µm depth level. Experimental XPCT data: white beam, average X-ray energy: 21 keV, SDD: 20 cm, and effective pixel size: 2 µm. Histological information: H&E staining, ×200 magnification, 0.25 µm pixel size.

As a two-dimensional technique, conventional histology may prove inadequate for accurately determining the precise location of full-thickness epidermal loss in the context of melanoma. However, an experienced pathologist is able to predict whether it is an ulceration or a blood clot even without the exact position of the epidermis rupture. In this instance, the histological section was fortuitous in its ability to assess the situation. Conversely, XVH was able to confirm the absence of an intact epidermis and the correlation between epidermal consumption and ulceration in a larger area

by virtually sectioning the entire volume. The examination revealed the presence of multiple points of rupture in the epidermal integrity, which served to augment the degree of severity and consequently result in a less favourable prognosis [143].

6.3.3 Nodular Malignant Melanoma

Nodular malignant melanoma is a highly aggressive subtype of invasive melanoma. It presents as a rapidly growing, raised lesion, characterized by a vertical growth phase without a preceding radial growth phase, distinguishing it from other melanoma types. NMM typically appears as a compact mass of dysplastic tumor cells with upward epidermal and dermal invasion. Nodular melanomas often show a dense infiltration of tumor cells into the deeper dermis or even subcutaneous fat, accompanied by a lack of symmetry as in case of Figure 6.7.

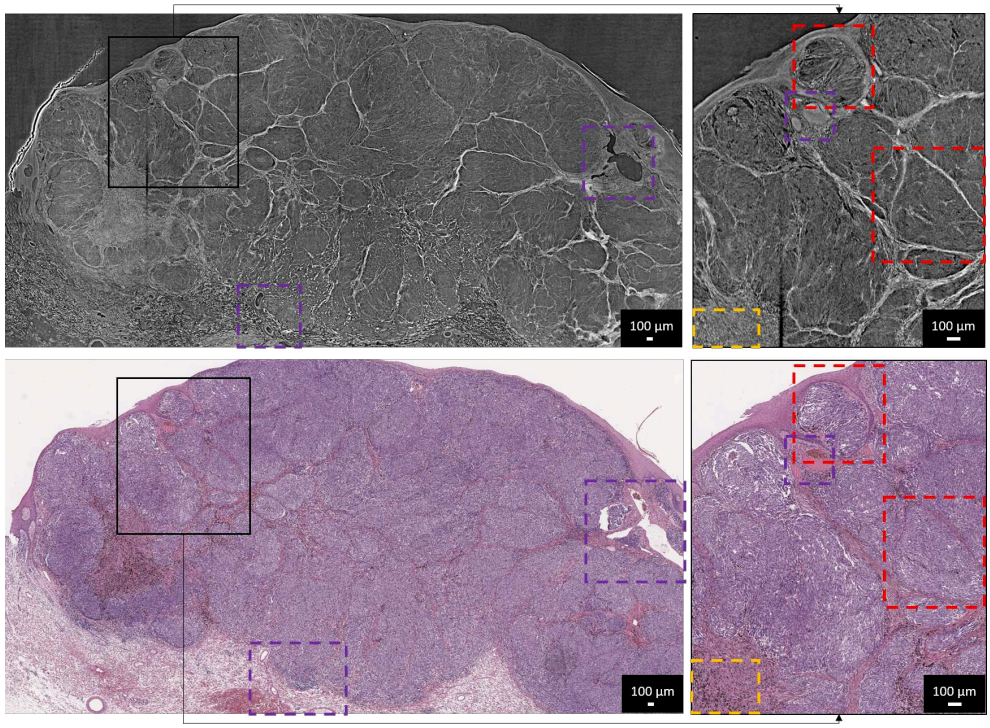

Figure 6.7. X-ray virtual histology (top panels) and conventional histology (bottom panels) images of nodular malignant melanoma. Red dotted areas mark some tumor cell nodules, purple areas highlight the presence of a lymphovascular network, and yellow ones are the part of tissue melanin pigmentated. Experimental XPCT data: white beam, average X-ray energy: 21 keV, SDD: 20 cm, and effective pixel size: 2 µm. Histological information: H&E staining, ×200 magnification, 0.25 µm pixel size.

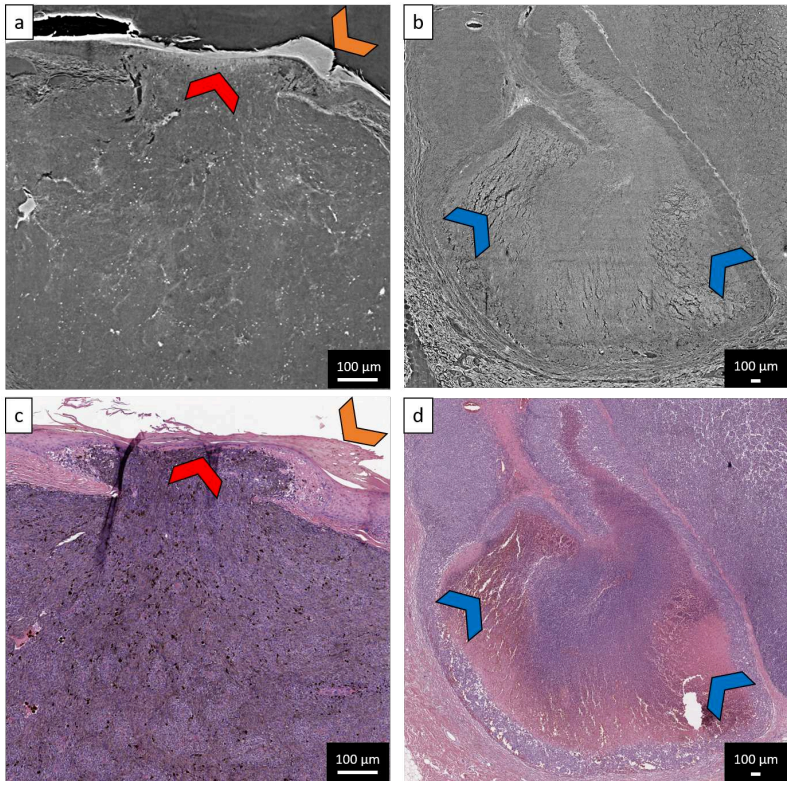

Figure 6.8. Close-up images presenting two nodular melanomas presenting ulceration (a)(c) and tumor necrosis (b)(d) investigated via X-ray virtual histology (a)(b) and traditional histology (c)(d). Experimental XPCT data: white beam, average X-ray energy: 21 keV, SDD: 20 cm, and effective pixel size: 2 µm. Histological information: H&E staining, ×200 magnification, 0.25 µm pixel size.

The tumor cells in nodular melanoma are often large and pleomorphic. Mitotic activity is frequently observed, indicating a rapid cell division and proliferation indicative of aggressive biological behavior. While this aspect can only be assessed via histology in Figure 6.7, XPCT can capture the overall tumor density organization in nodules. The high-resolution morphology of some of the clusters of highly atypical melanocytes is highlighted by the red dotted areas in the left panels of Figure 6.7. Furthermore, both imaging techniques demonstrate that the tumor mass is distinct and confined within its shell, with minimal epidermal spread compared to other subtypes of melanoma. Additionally, the lesion exhibits a high level of pigment production (yellow dotted areas), as well as a notable presence of lympho-vascularization internally and surrounding the melanoma (purple dotted areas). This indicates the invasive and potentially aggressive nature of nodular melanoma, as the vascular net-

work not only supplies nutrients to the tumor but also facilitates the migration of tumor cells through the vascular system. The presence of tumor necrosis and ulceration is nevertheless frequently observed in nodular melanomas. In the absence of these features in the previous case, Figure 6.8 illustrates two distinct types of nodular melanoma, as identified through XVH, which exhibit ulceration and tumor necrosis. Both Figures 6.8(a) and 6.8(c) demonstrate the presence of ulceration, indicated by an orange arrow, and the tumor below as the cause of this ulceration, indicated by a red arrow. The breakdown of the skin that overlies the melanoma lesion serves to illustrate the aggressive nature of this particular form of melanoma. Conversely, Figures 6.8(b) and 6.8(d) illustrate the presence of tumor necrosis, which indicates a high proliferation rate of tumor cells that exceed their blood supply, resulting in cell death and the potential for metastasis [144]. Both ulceration and tumor necrosis are significant histological features in nodular melanoma, as they frequently indicate aggressive tumor behavior, elevated risk of metastasis, and correlate with poorer clinical outcomes. In these cases, an analysis of the nearest lymph node, namely the sentinel node, is required to ensure that prompt intervention can be undertaken.

In conclusion, the use of correlative imaging of skin tissue and melanoma provides a more comprehensive view of the comparison of normal and cancerous tissues at multiple levels, from macroscopic features to microscopic details. This contributes to the improved detection and differentiation of malignant lesions.

The following chapter presents the application of a semantic segmentation model for the analysis of melanocytic lesions. This method enables the precise identification and categorization of regions of interest in medical images, facilitating the automated delineation of lesion boundaries and the assessment of their characteristics.

CHAPTER 7

Results - Semantic Segmentation Model For Melanocytic Lesion Detection In Synchrotron-Based X-ray Virtual Histology Images

In the previous chapter, the outcomes of integrating correlative imaging techniques, utilizing traditional histology and XPCT, for the analysis of skin tissues and skin tumors were presented. This chapter addresses the development of a deep learning model designed to automatically detect melanocytic lesions, offering a novel approach to enhance diagnostic accuracy and support early detection efforts in melanoma research. A semantic segmentation model for the assessment of melanoma in XVH images was constructed on the nnUNet architectural configuration. The methodology employed to create the skin tissue dataset, which comprises the training set and validation set, is fully detailed in Chapter 4. In this chapter, Section 7.1 describes the tuning of the parameters, with a particular focus on the testing of network parameters. Section 7.2 illustrates the performance results and the insights produced using the definitive semantic segmentation model on the XVH-based dataset of the skin tissues. Furthemore, the results of the inference process applied to the test set are presented. Subsequently, Section 7.3 depicts the results of the computation of the tumor thickness extension. To conclude, Section 7.4 presents additional three-dimensional computations derived from the same test set. All XPCT data were performed employing the PBI setup available at the SYRMEP beamline of the Elettra synchrotron (Trieste, Italy). The acquisitions were conducted in white beam (average X-ray energy: 21 keV), at a SDD of 20 cm and with a resulting effective pixel size of 2 µm.

7.1 Fine-Tuning nnUNet 2D Configurations

As the nnUNet is a semantic segmentation that automatically adapts its network parameters to the given dataset, a series of parameters based on the input data provided to the network (including image size, patch size, and batch size) have been subjected to testing. The outcomes of this process for the XVH-based dataset, which incorporates a range of skin tissue types, are presented in Table 7.1. No significant

changes were found when evaluating models' performances, except for reducing the dimensions of the input image.

	Dice-score	**IoU**	**Accuracy**	**Precision**	**Recall**
Image Size					
A	0.87 ± 0.09	0.80 ± 0.11	0.94 ± 0.02	0.91 ± 0.04	0.85 ± 0.12
B	0.84 ± 0.09	0.75 ± 0.11	0.91 ± 0.02	0.87 ± 0.05	0.83 ± 0.11
Patch Size					
D	0.92 ± 0.09	0.78 ± 0.10	0.93 ± 0.02	0.89 ± 0.05	0.85 ± 0.10
A	0.87 ± 0.09	0.80 ± 0.11	0.94 ± 0.02	0.91 ± 0.04	0.85 ± 0.12
E	0.87 ± 0.08	0.81 ± 0.01	0.94 ± 0.01	0.96 ± 0.02	0.86 ± 0.10
Batch Size					
F	0.86 ± 0.09	0.78 ± 0.10	0.93 ± 0.01	0.88 ± 0.05	0.85 ± 0.10
A	0.87 ± 0.09	0.80 ± 0.11	0.94 ± 0.02	0.91 ± 0.04	0.85 ± 0.12
G	0.87 ± 0.10	0.80 ± 0.12	0.94 ± 0.02	0.91 ± 0.04	0.86 ± 0.12
Image Norm.					
H	0.86 ± 0.10	0.79 ± 0.11	0.94 ± 0.02	0.90 ± 0.05	0.85 ± 0.12
A	0.87 ± 0.09	0.80 ± 0.11	0.94 ± 0.02	0.91 ± 0.04	0.85 ± 0.12
Data Norm.					
A	0.87 ± 0.09	0.80 ± 0.11	0.94 ± 0.02	0.91 ± 0.04	0.85 ± 0.12
I	0.85 ± 0.11	0.77 ± 0.12	0.93 ± 0.02	0.90 ± 0.04	0.83 ± 0.13

Table 7.1. Averaged metrics performance quantified considering all labels (melanocytic lesion, control tissue, background) in the five-folders cross-validation. 2D nnUNet configuration was considered varying parameters as follow: input image size, 1024×1024 (Config. A), and 512×512 (Config. B); patch size, 256×256 (Config. D), 512×512 (Config. A), and 768×768 (Config. E); batch size, 4 (Config. F), 12 (Config. A), and 20 (Config. G); image normalization, rescaling to [0,1] interval (Config. H), and z-score (Config. A); data normalization, instance normalization (Config. A), and batch normalization (Config. I). All parameters chosen are reported in Table 4.5.

In all metrics evaluations retrieved by the five-folders cross-validation of all models, as reported in Table 7.1, the dice-score coefficients demonstrate higher values than the IoU coefficients by a few percentage points. As these metrics penalize false positive predictions, they provide evidence of some inaccuracies in the recognition of certain features. Nevertheless, the outcomes for recall and dice-score are similar, indicating an overall balanced model. Conversely, all models demonstrate exceptional accuracy and precision, attesting to the comprehensive rigor employed in accurately segmenting melanocytic lesions and discerning the other components of the skin tissues.

The configuration that employs the nnUNet-selected default parameters, designated as Configuration A, produces the most intriguing validation outcomes. However, the results are suboptimal when the same whole-slide image, from which the ROIs were extracted, is subjected to inference, as visible in Figure 7.1(b).

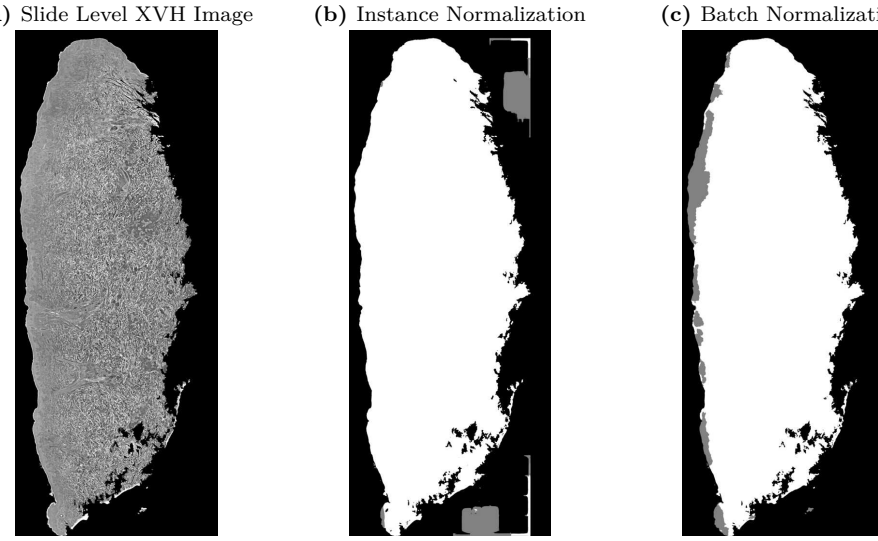

Figure 7.1. (a) The entire XVH image presented alongside two subsequent slide-level inference representations: (b) the former retrieved by employing instance normalization (Config. A of Table 7.1), and (c) the latter utilizing batch normalization (Config. I of Table 7.1).

As noted in [145], the issue was resolved by employing the batch normalization of Configuration I in Table 7.1, and the resulting outcome is illustrated in Figure 7.1(c). Although there is a slight decline in performance, as evidenced in Table 7.1, the application of batch normalization produces superior results, effectively eliminating the random patch artifacts that occur during the sliding window inference process across the entire XVH image.

7.2 Performance Outcomes And Key Results Of The nnUNet 2D Model

Following the interpretation of all metrics in Table 7.1 and the visualization of all validation and slide-level outcomes, a full five-fold cross-validation of Model I was conducted for 1000 epochs. The resulting performances are reported in Table 7.2.

Although both models demonstrate comparable performance concerning the metrics employed, training the model for 1000 epochs ensures superior visual outcomes

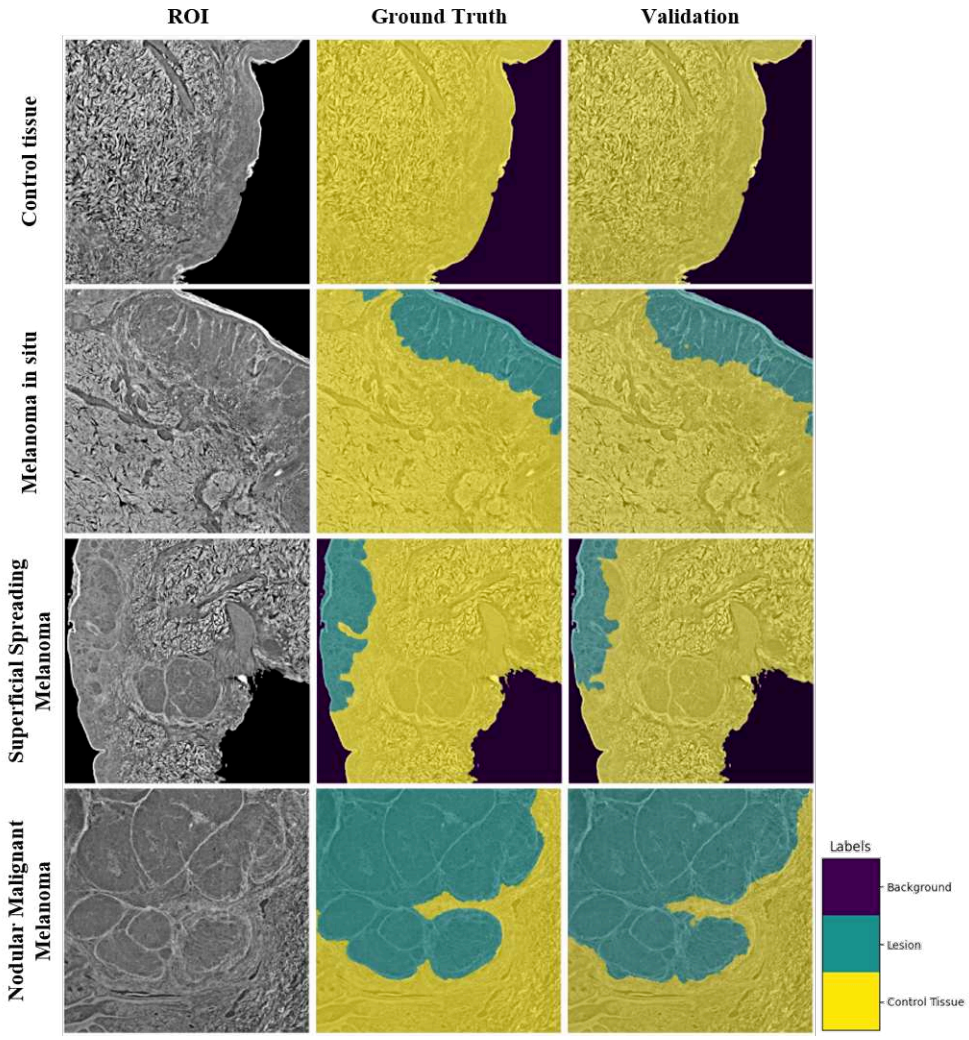

Figure 7.2. Patch-level validation produced employing full cross-validation. XPCT patches are of 1024×1024 pixels^2, resulting in a region of 2 mm $\times$ 2 mm.

when applying slide-level inference to both the validation, as shown in Figure 7.2, and test sets, as illustrated in Figure 7.4.

	Dice-score	IoU	Accuracy	Precision	Recall
2D U-Net	0.87 ± 0.10	0.81 ± 0.12	0.95 ± 0.02	0.93 ± 0.03	0.86 ± 0.12

Table 7.2. Metrics performance of full five-fold cross-validation for 2D U-Net configuration applied to ROIs using 1000 epochs.

Patch-level validation of Figure 7.2 demonstrates the model's remarkable adaptability to diverse types of skin. With regard to lesion predictions, the model exhibits a slight tendency to underestimate the borders visible in the ground truth images. However, it does not exhibit any confusion with the various structures that comprise the pilus or other components of the skin tissue. This result is consistent with the findings of the 5-fold validation metric performance analysis, as illustrated in Figure 7.3.

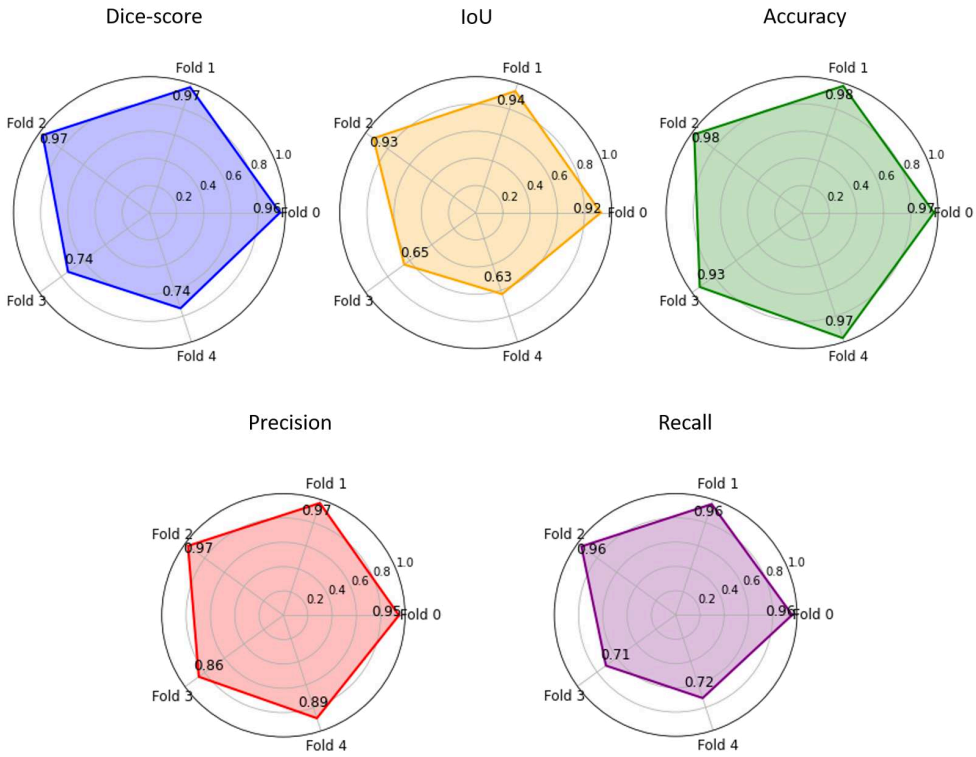

Figure 7.3. Metric performance for 5-fold validation of the 2D nnUNet model.

By averaging the metric performance of the classes of melanocytic lesion and

control tissue, it was found that the first three folders produced the best overall performance for the model in all categories. In contrast, the cases in folders 3 and 4 yielded the poorest results, likely due to the network's difficulty in discriminating between two highly similar cases with distinct tissue morphologies. One case was benign (Figures 6.1(a) and 6.1(d)), while the other was malignant (Figure 6.6). However, all models demonstrate consistent and reliable accuracy and precision, thereby ensuring the maintenance of high-performance results.

To assess the visual performance of the model, the inference process was conducted on entire XVH slices. As an example, the case presented in Figure 7.4 is a biopsy of a nodular malignant melanoma paired with a superficial spreading melanoma. This is one of the most intriguing datasets considered through XVH due to its distinctive morphological behavior, which was not observed in other datasets. This dataset was therefore included in the test set.

(a) Slide-Level XVH Image **(b)** Manual Annotation **(c)** Slide-Level Inference (100 epochs) **(d)** Slide-Level Inference (1000 epochs)

Figure 7.4. (a) Visual representation of an intriguing case of a nodular malignant melanoma and superficial spreading melanoma in the same skin excision by means of X-ray Virtual Histology. (b) Manual annotation performed on the same image not considered for training the semantic segmentation model. Slide-level inference using the same model trained with 100 epochs (c) and with 1000 epochs (d).

As illustrated in Figure 7.4(c), the nnUNet model trained for 100 epochs performed sparse segmentation, probably following the most dense parts, which characterizes the nodular structure and the superficial melanoma distribution. Conversely, the same model trained for 1000 epochs exhibited the capacity to discern the diffusion of the superficial spreading melanoma, the structural configuration of the nodular melanoma, and also the ulceration underlying it. This is evident in the comparison between the manual annotation image depicted in Figure 7.4(b) and the slide-level inference image presented in Figure 7.4(d). The model, whose performances are reported in Table

7.2, was used to infer XVH-based slices extracted from the same tissues. Figure 7.5 illustrated some 2D previews of the melanocytic lesions overlaying XVH images.

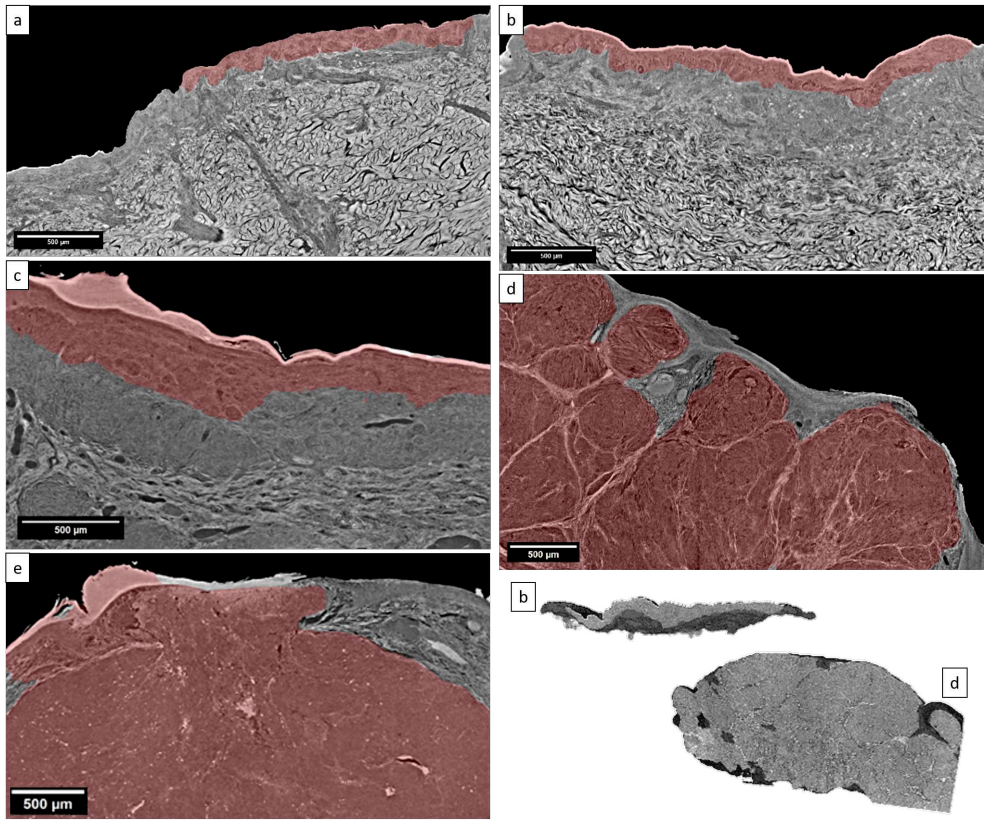

Figure 7.5. Whole-slide level inference applied to (a) a melanoma in situ, (c)(d) two superficial spreading melanoma, and (b)(d) two nodular malignant melanoma. The red overlay represents the melanocytic lesion. Volume rendered images of case (b) and (d) are also reported.

The semantic segmentation model successfully detects all melanocytic lesions in the test set group, from the in situ lesion (Figure 7.5(a)) to the nodular melanoma types (Figures 7.5(d) and 7.5(e)). It is impressive how the model was able to discriminate to exclude regular epidermis in nodular melanoma cases (Figures 7.5(d) and 7.5(e)) from the tumor-infiltrated ones superficial spreading melanoma (Figures 7.5(b) and 7.5(c)). Moreover, the melanocytic lesion assessment by means of the semantic segmentation model accurately identifies and marks the in situ melanoma confined to the epidermal layer, as illustrated in Figure 7.5(a). Furthermore, the ulceration above the melanocytic lesion in Figure 7.5(e) has been successfully assessed by the semantic segmentation model.

The results of the XVH analysis align with the melanoma classification determined through conventional histology. Furthermore, while the DL segmentation result produced by the DL model correctly identified melanoma in situ as the tumor area confined to the epidermis, all other cases were found to be invasive. Indeed, both cases (b) and (c) were classified as invasive SSM based on the histological examination. This is because the boundaries of the epidermis are not discernible, and the lesion invades the dermal layer, which is consistent with the results of the histological examination.

As illustrated in the 3D renderings of Figure 7.5, the dimensions of tissues decrease in size as they deepen into the FFPE block. This is due to the fact that the maximally extended surface is typically the most external, as in conventional histology it is common practice to bisect the entire skin tissue to observe the central part of the tumor. Conversely, three-dimensional insights of the spatial distribution of melanoma are easily retrieved by plotting the 3D volume of the tumors.

7.3 Three-Dimensional Estimation Of Breslow Thickness

As an important measure to define the staging to a melanoma together with ulceration, Breslow Thickness is computed 2D from conventional histology as the maximum depth of the deepest tumor cell into dermis from the epidermal layer. Such measurement was also performed in XVH images with the same modality, but considering 500 µm of skin tissue inside the FFPE block. A representative illustration per sample is presented in Figure 7.6.

For each sample illustrated in Figure 7.6, the tumor thickness was calculated based on volumes of 500 µm depth via XVH. The maximum values, which correspond to the Breslow thickness, were considered together with the average results. Although the specimen depicted in Figure 7.6(c) and 7.6(e) is the same, it contains two distinct melanomas, and thus two distinct measurements of Breslow thickness were performed. The Breslow thickness was not calculated via histology for cases (a) and (c) due to their lack of representativeness from a diagnostic perspective. This is because the former was diagnosed as MIS, thus there was no necessity for measuring the thickness of the tumor, as the tumor cells were confined to the epidermis. In the second case, the nodular melanoma was the primary factor in determining the staging, therefore the SSM was not included. Nevertheless, a quantitative assessment was conducted via XVH on case (c) for the purpose of comparison with the other measurements. These results are presented in Table 7.3 and compared to those obtained via conventional histology for diagnostic purposes.

The XVH measurements exhibited a slight discrepancy with the histological results utilized for the diagnosis. The discrepancy can be attributed to the fact that the histology on which the measurement was based was not included in the FFPE block. Instead, it was an external section that was processed prior to the XVH investigation. Furthermore, the measurement enabled the tumor staging to be determined

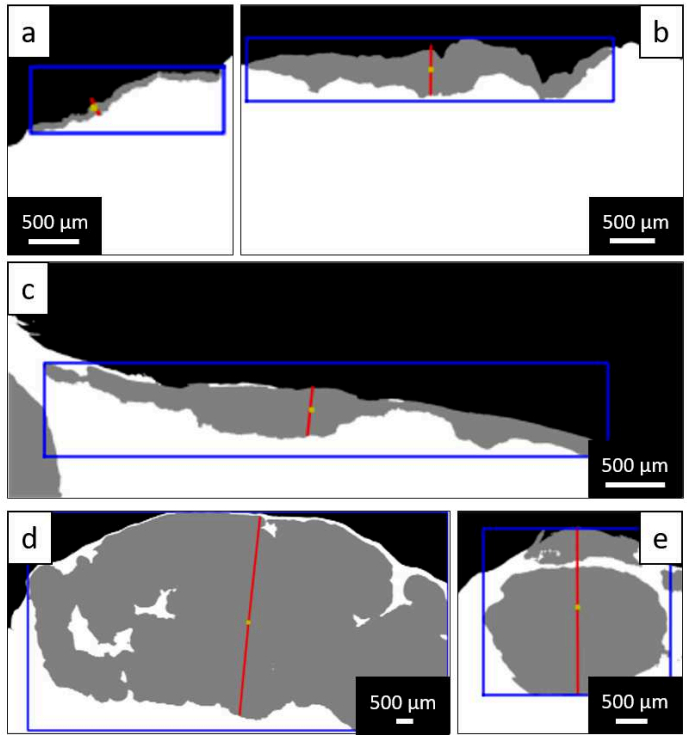

Figure 7.6. Visual representations on tumor thickness assessment for each sample: (a) melanoma in situ, (b)(c) superficial spreading melanoma, and (d)(e) nodular malignant melanoma. In each image, the blue rectangle represents the bounding box, which encloses the lesion area. The yellow point indicates the centroid of the lesion area, and the red line depicts the tumor extension of the melanocytic lesion.

		Via Histology		**Via X-ray Virtual Histology**	
	Type	Thickness	T Category	Thickness	T Category
a	MIS	-	Tis	-	Tis
b	SSM	0.9 mm	T1	0.6 mm	T1
c	SSM	-	-	1.3 mm	T2
d	NMM	3.8 mm	T3	3.1 mm	T3
e	NMM	6.5 mm	T4	5.7 mm	T4

Table 7.3. Computation of Breslow Thickness two-dimensionally, thus via Conventional Histology, and three-dimensionally, via X-ray Virtual Histology. Tumor thickness measurements are reported together with the associated T category of TNM staging. Legend: MIS, melanoma in situ; SSM, superficial spreading melanoma; NMM, nodular malignant melanoma.

according to the depth criterion in the TNM staging system, as detailed in 2.1 and referenced in [19, 20]. Finally, the T category assigned by the XVH results was found to align with the one derived from the histological diagnosis.

7.4 Quantitative Tumor Analysis

The same datasets from the test set, which were previously classified as melanoma via conventional histopathology and represented in Figure 7.5, were subjected to volumetric-retrieved measurements. These results are presented in Table 7.4.

	Type	**Average Tumor Volume** [mm^3]	**Average Tumor Area** [mm^2]	**Average Tumor Thickness** [mm]
a	MIS	0.42	0.41 ± 0.17	0.24 ± 0.06 mm
b	SSM	0.38	0.77 ± 0.14	0.47 ± 0.07 mm
c	SSM	0.76	1.53 ± 0.34	0.71 ± 0.25 mm
d	NMM	3.84	7.69 ± 1.29	2.73 ± 0.25 mm
e	NMM	35.92	51.17 ± 0.45	5.67 ± 0.03 mm

Table 7.4. X-ray Virtual Histology-retrieved averaged results, i.e., tumor volume, area, and thickness, used for melanocytic lesion quantification upon 250 consecutive slices (500 µm depth inside FFPE block).

Tumor areas were measured on each XVH image. The average and the standard deviation were calculated to assess variability in the tissue progression inside the FFPE block. The provision of both the maximum, illustrated in Table 7.3, and the average thickness measurement, in Table 7.4, allows for an understanding of the spatial distribution of the lesion within the skin tissue. It was observed that all tumor lesions exhibited a general decrease in size as they were traced into the depth of the FFPE block. This aspect is more prevalent in MIS and SSM cases than in NMM ones, as the latter were found to maintain their structural integrity due to their considerable dimensions. Finally, the potential of XVH is to provide not only the maximum measured tumor thickness, but also an estimation of the evolution of the tumor inside the FFPE block, including average and potentially other statistical data.

To conclude, this chapter demonstrates how a semantic segmentation model applied to XVH images can help in tumor assessment and analysis, while supported by histopathological validation. The subsequent chapter examines the use of correlative imaging to study invasive patterns in non-small cell lung cancer (NSCLC), focusing specifically on the combined insights provided by XVH and conventional histological techniques.

CHAPTER 8

Results - Non Small Cell Lung Cancers Investigation Via Synchrotron-Based X-ray Virtual Histology

This chapter explores the correlative imaging of invasive patterns in non-small cell lung cancer (NSCLC), with a particular focus on how X-ray virtual histology and traditional histology can provide valuable insights into tumor spread and tissue architecture. More into details, Section 8.1 will present the most common histological patterns of NSCLC through correlative imaging. Subsequently, Section 8.2 will examine some of the most significant patterns of invasion observed in NSCLC. These findings will demonstrate how these advanced computational techniques can enhance the precision and efficiency of tumor characterization and quantification. All XPCT data were performed employing the PBI setup available at the SYRMEP beamline of the Elettra synchrotron (Trieste, Italy). The acquisitions were conducted in white beam (average X-ray energy: 21 keV), at an SDD of 20 cm and with a resulting effective pixel size of 2 µm. All histologies, reported in this chapter, were scanned at a 0.27 µm pixel size resolution (×20 magnification).

8.1 Correlative Imaging Of Non-Small Cell Lung Cancers

The histological classification of non-small cell lung cancer is crucial because it directly impacts diagnosis, prognosis, and treatment decisions. NSCLC consists of various subtypes, including adenocarcinoma, squamous cell carcinoma, and large cell carcinoma, each with distinct biological behaviors, responses to treatment, and outcomes. This section presents a concise overview of the former two cases.

8.1.1 Adenocarcinoma

Following the most recent definitions set forth by the eighth edition of the WHO classification of lung cancers [1, 146], invasive non-mucinous lung adenocarcinoma

(Adk) can be classified into five patterns based on histological features: lepidic, acinar, papillary, micropapillary, and solid. In many instances, neoplasia manifests with mixed characteristics. The order in which the five subtypes of lung adenocarcinoma are reported reflects the increasing grade of poorer adverse clinical outcome [147,148].

8.1.1.1 Lepidic Adenocarcinoma

Lepidic predominant Adk is characterized by more thickened septa in response to the development of atypical and neoplastic cells along them. In fact, compared to intact lung parenchyma in the top parts of Figure 8.1, the growing of nonmucinous adenocarcinoma cells along the alveolar walls is mainly assessable in the histological image (Figure 8.1(b)), but still discernible as a thin light gray border on alveolar septa in XVH image (red arrows in Figure 8.1(a)).

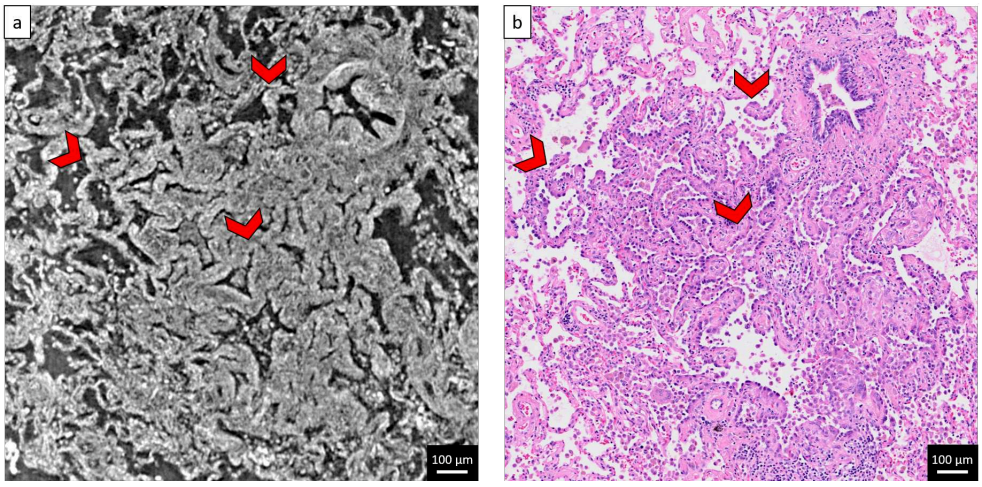

Figure 8.1. Detail of thickened septa, evidenced by red arrows, in a lepidic predominant adenocarcinoma considered through XVH and histology. Experimental XPCT data: white beam, average X-ray energy: 21 keV, SDD: 20 cm, and effective pixel size: 2 µm. Histological information: H&E staining, ×20 magnification, 0.27 µm pixel size.

8.1.1.2 Acinar Adenocarcinoma

Acinar predominant Adk shows more infiltrant properties than lepidic type. As illustrated by Figure 8.2, such invasive tumor is arranged in acini and small tubules, which can assume more complex irregular gland configurations. Histology demonstrates the composition of such acini in cuboidal or columnar cells, that resemble bronchial glands or bronchial-lining epithelial cells, as evidenced by red arrows in Figure 8.2(b). In Figure 8.2(a), the XVH image comprises two distinct phases: the brightest phase, which represents the inflammatory process, and the grayest phase, which denotes the

presence of acinar glands. The assessment of glandular tissue in XVH is feasible due to the localization of internal foci and the discernible arrangement of neoplastic cells.

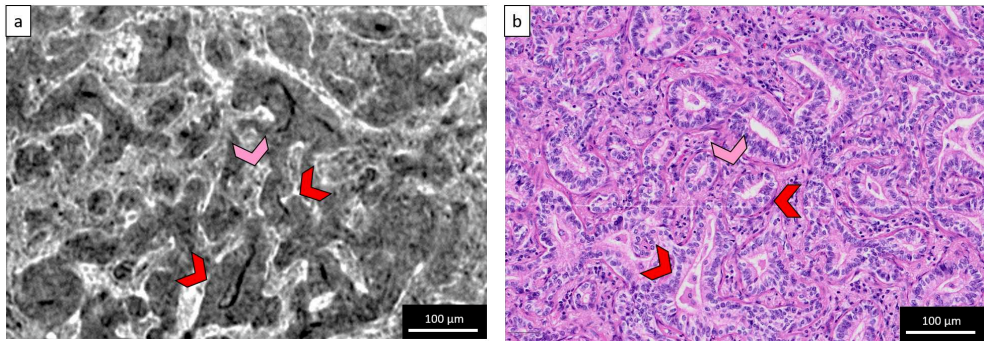

Figure 8.2. Acinar predominant adenocarcinoma considered via XVH-based and histological images. Red and pink arrows point at neoplastic glands arranged in acini and inflammation. Experimental XPCT data: white beam, average X-ray energy: 21 keV, SDD: 20 cm, and effective pixel size: 2 µm. Histological information: H&E staining, ×20 magnification, 0.27 µm pixel size.

8.1.1.3 Papillary Adenocarcinoma

The progression from acinar to the papillary pattern is characterized by the formation of papule and papillary structures, as evidenced by red arrows in Figure 8.3. These structures develop by neoplastic cells that line fibrovascular cores and alveolar thickened septa. As illustrated in Figure 8.3(b), tumor cells are moderately differentiated (G2) and associated with an intermediate prognosis. Figure 8.3(a) depicts the XVH image, which presents a virtual section situated at a depth of several micrometers below the histological one. The illustration demonstrates how the tumor panorama evolves at various levels of depth below while maintaining focus on the same region.

8.1.1.4 Micropapillary Adenocarcinoma

Micropapillary predominant Adk is mostly composed of small, tight clusters of tumor cells without showing a clear fibrovascular core, as in the papillary case. The presented typology illustrates the micropapillar superimposition of cells, which gives rise to the formation of dense structures, as well as a diminished presence of connective tissue. As evidenced by red arrows in Figure 8.4, micropapillae appear as small compact clusters of cells floating within alveoli and infiltrating the stroma. While histology can discern them as dense, irregular nests detached from the main inflammatory structure in Figure 8.4(b), XVH imaging can assess them as white pepitas floating within the glandular lumina in Figure 8.4(a). Furthermore, XVH is capable of visualizing

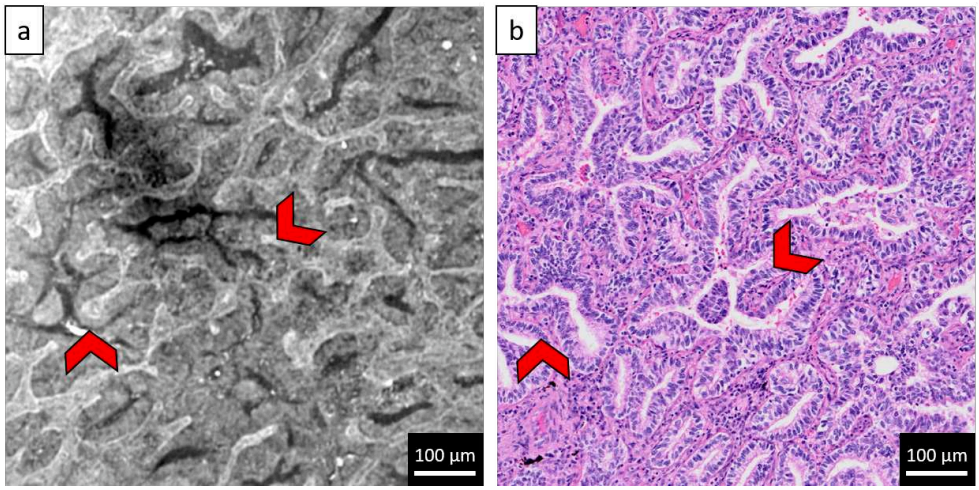

Figure 8.3. Papillary pulmonary adenocarcinoma details pointed by red arrows illustrated via XVH and histology. Experimental XPCT data: white beam, average X-ray energy: 21 keV, SDD: 20 cm, and effective pixel size: 2 µm. Histological information: H&E staining, ×20 magnification, 0.27 µm pixel size.

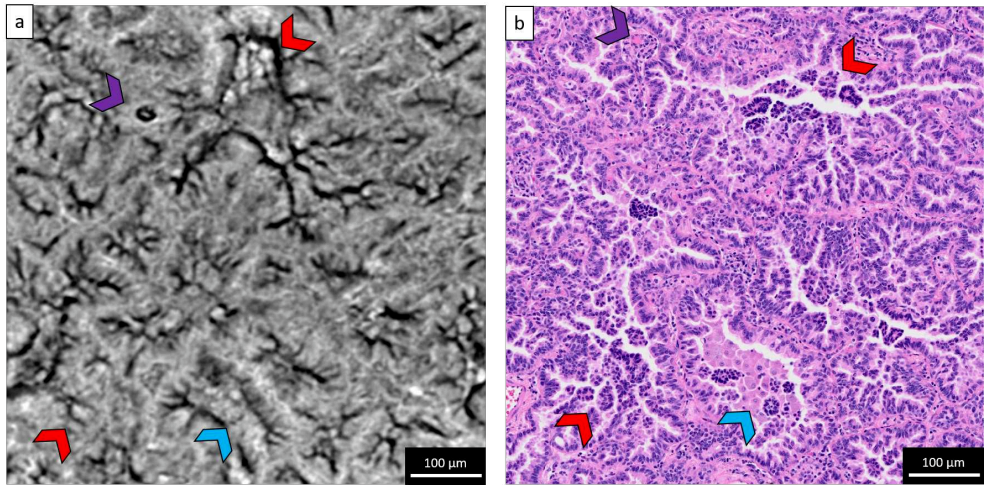

Figure 8.4. Micropapillary predominant adenocarcinoma in correlative imaging between XVH and histology. Red arrows point at small micropapillary structures, light blue ones at inflammation processes, and purple ones at blood vessels. Experimental XPCT data: white beam, average X-ray energy: 21 keV, SDD: 20 cm, and effective pixel size: 2 µm. Histological information: H&E staining, ×20 magnification, 0.27 µm pixel size.

the morphological structure created by the branched voids that are characteristic of micropapillary extremities.

8.1.1.5 Solid Adenocarcinoma

Solid predominant adenocarcinoma of the lung is characterized by the growth of tumor cells in solid sheets or nests. As the most aggressive subtype of pulmonary adenocarcinoma, solid Adk lacks significant glandular differentiation in the histological image depicted in Figure 8.5, thereby raising the question of whether it should be identified as an adenocarcinoma or a squamous cell carcinoma (presented in the next section). In this instance, immunohistochemical staining with TTF-1 served to corroborate the diagnosis of solid adk. Figure 8.5(a) evaluates the same regions of Figure 8.5(b) but at a depth of a few micrometers below the selected histological plane. The lymphocytic infiltrate, indicated by blue arrows, is the predominant feature within the solid tumor in XVH, whereas in the selected histological image, it is largely circumscribed by the solid sheets highlighted with red arrows. The vascular network is frequently observed (see purple arrows), surrounded by stroma and tumor nests.

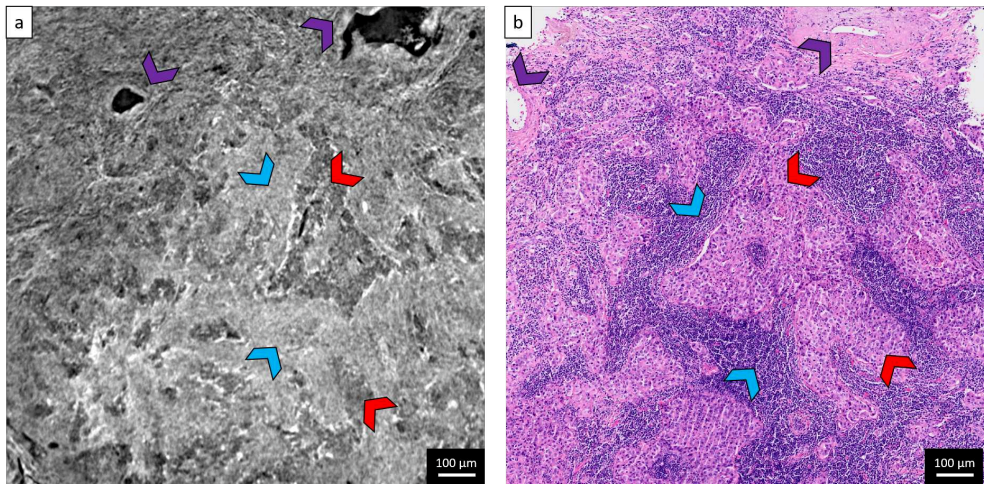

Figure 8.5. Solid predominant adenocarcinoma subtypes represented via (a) XVH and (b) histology. Red arrows point at solid tumor nests, light blue ones at lymphocytic infiltrate, and purple ones at blood vessels. Experimental XPCT data: white beam, average X-ray energy: 21 keV, SDD: 20 cm, and effective pixel size: 2 µm. Histological information: H&E staining, ×20 magnification, 0.27 µm pixel size.

8.1.2 Squamous Cell Carcinoma

Squamous cell carcinoma (SqCC) of the lung, also known as squamous cell lung cancer, originates from metaplastic squamous epithelia in the bronchial tree. Figure 8.6 displays a correlative imaging of a SqCC via XPCT and traditional histology. When examined under the microscope as in Figure 8.6(b), SqCC is composed of large pink cells that grow in groups called sheets or nests. Tumor cells inside them are usually larger than normal squamous cells and tend to be pleomorphic, as they show a range of shapes and sizes.

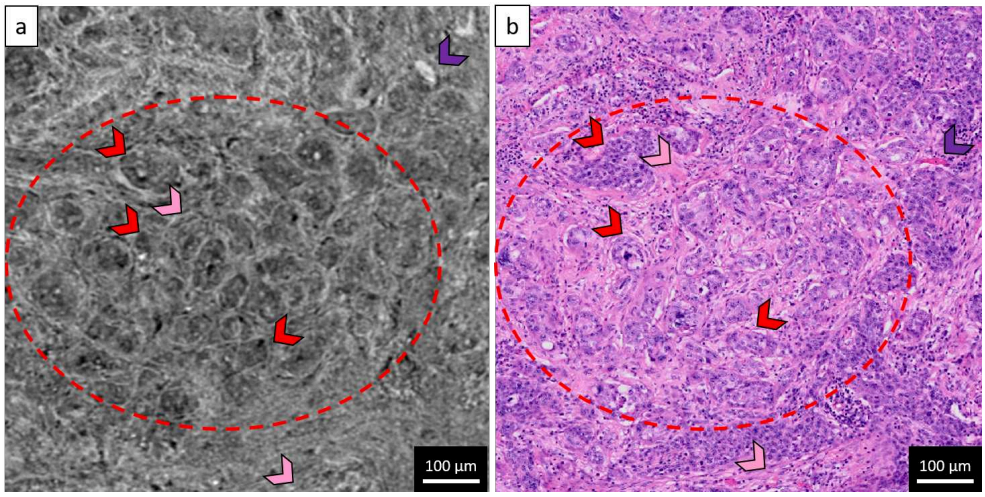

Figure 8.6. A case of squamous cell carcinoma (SqCC) analyzed via XPCT (a) and histology (b). The red dotted area highlights a great cluster of tumor nests, some of them pointed by red arrows. Purple arrows mark the presence of blood vessels, while pink arrows the inflammation surrounding tumor nests. Experimental XPCT data: white beam, average X-ray energy: 21 keV, SDD: 20 cm, and effective pixel size: 2 µm. Histological information: H&E staining, ×20 magnification, 0.27 µm pixel size.

XPCT in Figure 8.6(a) can appreciate the same tumor nests appearing in histological image. The stroma surrounding these clusters provides more contrast in distinguishing the cellular borders. The dark spots observed within the tumor nests in the XPCT image are indicative of pseudo-empty lacunae, which are presumed to correspond to regions of necrosis and apoptosis. As SqCC is defined by its variable degree of squamous differentiation, such as keratinization or intercellular bridging. The degree of squamous differentiation provides the basis for determining if the carcinoma is well, moderately or poorly differentiated. The SqCC case reported in Figure 8.6 was diagnosed as grade G3, meaning that tumor cells are poorly differentiated, leading to a more severe level of aggressiveness.

8.2 Invasive Cancer Properties In NSCLC

The preceding section was intended to provide an introduction to the application of XVH imaging to the most prevalent typology of NSCLC. In these samples, certain invasive phenotypes, including STAS, pleural invasion, and lymphovascular invasion, were identified through histological investigation and subsequently documented. The next section presents the results of the XPCT investigation applied to tumor invasion characteristics. This serves to provide the three-dimensional context and define a new method of investigating such characteristics.

8.2.1 STAS - Spread Through Air Spaces

In the histopathological images, tumor STAS features were predominantly observed within the air spaces of the lung parenchyma close to the main tumor, as illustrated in Figure 8.7.

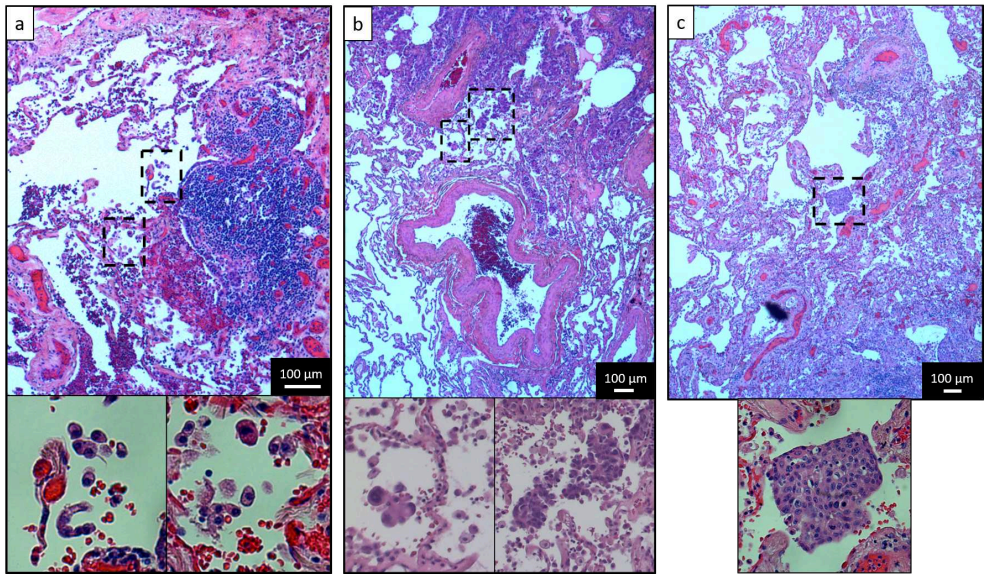

Figure 8.7. Spread through air spaces patterns in non-small cell lung cancers (NSCLC) histologies. a) Single-cell pattern STAS consisting of scattered discohesive single cells; b) floret Micropapillary pattern STAS floating in alveolar space; and c) Solid pattern STAS in lung parenchyma beyond the edge of the main tumor. Histological information: H&E staining, ×20 magnification, 0.27 µm pixel size.

The three morphological patterns, as considered in [1, 149], include sparse single cells scattered (Figure 8.7(a)), clusters and floret micropapillary (Figure 8.7(b)), and solid nests (Figure 8.7(c)), which are visible as free-floating structures within the air

	NSCLC tissue type	Grade	STAS pattern
A	Adk acinar, mucinous, and lepidic	G2	MIP
B	Adk acinar, and micropapillary	G2	MIP
C	Adk acinar, papillar, micropapillary, and solid	G2	single cells, MIP
D	Adk acinar, papillar, micropapillary, and solid	G2	single cells, MIP
E	Adk solid, and micropapillary	G2	single cells, MIP
F	SqCC	G3	SNs
G	SqCC	G3	single cells, MIP, SNs

Table 8.1. Specimen information regarding NSCLC type, tumor grade, and STAS pattern extracted from histological diagnosis. Legends: Adk, adenocarcinoma; SqCC, squamous cell carcinoma; MIP, micropapillary; SNs, solid nests.

spaces. The tumor STAS represented in Figure 8.7 were chosen to be considered due to their distance from the main tumor, even if they existed only in the first alveolar layer far from the tumor edge. STAS structures were found in seven cases out of nineteen by whole-slide image inspection. Table 8.1 reports the most interesting cases classifying STAS by pattern (single cells, micropapillary, solid nests) and lung cancer type (lung adenocarcinoma, squamous cell carcinoma). The visual inspection of histological slides found out that STAS as single cells and Micropapillary (MIP) clusters were mainly found in the external part of primary tumors of adenocarcinomas, while Solid Nest (SN)s STAS were only visible in squamous cell carcinoma.

8.2.1.1 Attachment Of Single Cells And Micropapillary STAS To The Main Tumor And Alveolar Walls

Single cells and micropapillary clusters are common typologies of STAS in NSCLC, in particular in those subtyped as adenocarcinoma. Figure 8.8 shows a comparison of the same area analyzed via traditional histology (a), and X-ray virtual histology (b)(c). Even though the characteristics of the histological image do not correspond perfectly to those appearing in the XVH image, Figure 8.8 considers the same region for both techniques. The alveolar area, as observed in Figure 8.8(a)(b), displays a multitude of floating single and clustered abnormal cells, which are indicated by red dotted circles. These elements form discrete groups attached to alveolar walls and blood vessels, which then attach to the primary tumor, as emerges in Figure 8.8(c). This image is the result of the application of the maximum intensity projection over a set of 5 consecutive slices (corresponding to 10 µm), which simplifies the three-dimensional stack into a two-dimensional image.

Figure 8.9 illustrates two types of adenocarcinoma with micropapillary STAS pattern at their margins highlighted by red dotted areas. Observing Figures 8.9(a) and 8.9(c), cancer cells of acinar-type tissue are arranged in acini and tubules while small

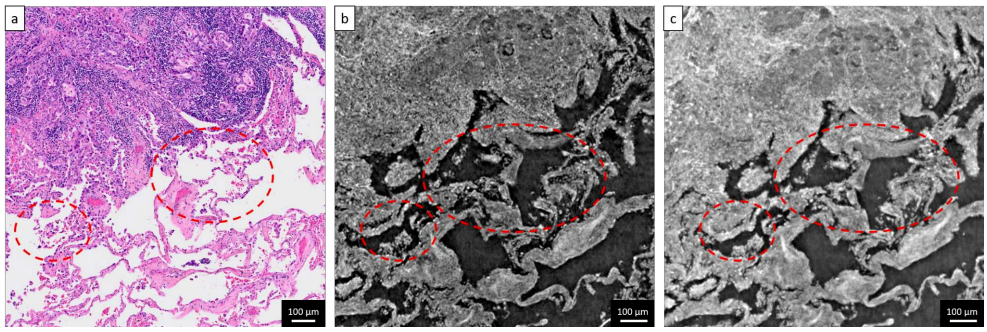

Figure 8.8. Same region of interest of single cells STAS in an adenocarcinoma tissue visualized via conventional histology (a) and XVH (b)(c). Single cells STAS appear as floating elements in the alveolar spaces in histological (a) and in XVH images (b). The same tumor cells are presented projecting the five consecutive XVH-based slices, thus performing a maximum intensity projection over a volume of 10 µm depth (c). Experimental XPCT data: white beam, average X-ray energy: 21 keV, SDD: 20 cm, and effective pixel size: 2 µm. Histological information: H&E staining, ×20 magnification, 0.27 µm pixel size.

rounded groups of tumor cells appears floating in the lung parenchima at different distances from the main tumor. In conventional histology, these are visible as purple ring-like structures containing pink stroma. The XPCT image illustrates the identical histological microarchitecture of MIP clusters, discernible as light grey dots, situated in close proximity to alveolar walls and blood vessels, as indicated by the purple arrows. Moreover, the micropapillary STAS clusters highlighted by the dotted areas in the histology are also visible in the XPCT image, demonstrating attachment to the neoplasm. A comparison of the two slides reveals that the XPCT approach provides a more detailed representation of the tumor structure. The histological technique, however, displays tumor areas that have been previously removed from the FFPE block, thereby rendering this structure inaccessible to XPCT investigation. The histological image displays a more extensive configuration of the tumor than that shown in the XPCT image, which has been taken with a depth of a few micrometres within the intact tissue situated within the FFPE block. The MIP clusters bordering the main tumor in the XPCT image represent the remaining tumor branch highlighted in the histological analysis. This suggests that the tumor has undergone a reduction in size within the FFPE block. Following the progression within the FFPE block with XPCT, the MIP STAS demonstrates to be the extremities of the tumor periphery, which has been sectioned transversally. Furthermore, these STAS pattern developed contingent to vascular networks, as evidences by purple arrows, with the aim of expanding the tumor while also seeking for structural support. As illustrated in Figures 8.9(b) and 8.9(d), MIP clusters are observed as fragmented clusters of tumor cells, exhibiting a floating behaviour within the alveolar spaces. In contrast with the preceding case, the tumor captured by histology is of a smaller size than that visible in the XPCT image. This indicates that the tumor is expanding. Similarly to the

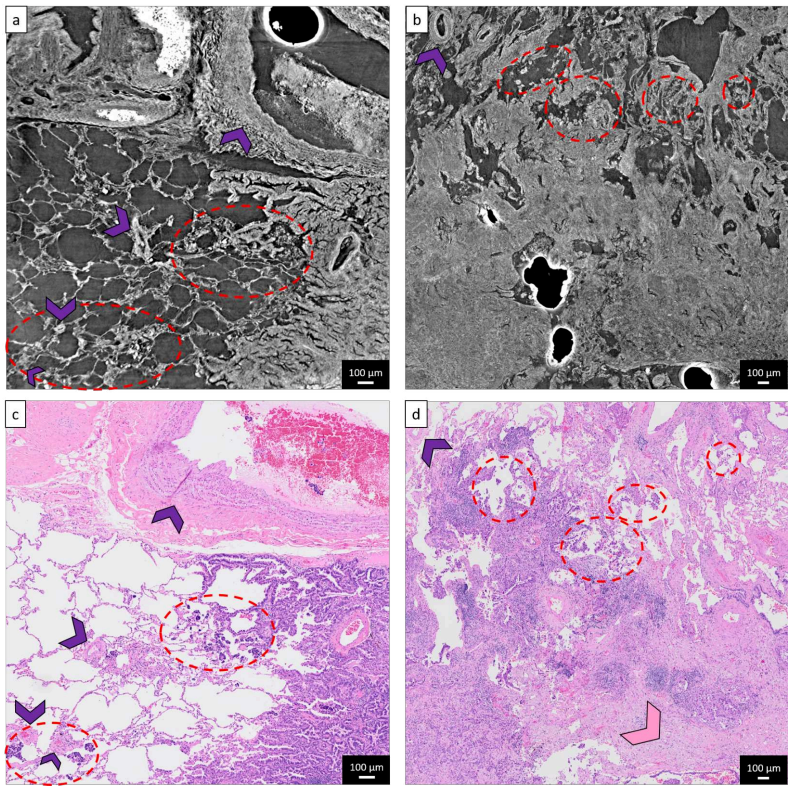

Figure 8.9. Two types of adenocarcinoma lung cancer with micropapillary (MIP) clusters highlighted by red dotted ovals investigated by means of XPCT (a)(c) and traditional histology (b)(d). Blood vessels in the lung parenchima is pointed by purple arrows. Experimental XPCT data: white beam, average X-ray energy: 21 keV, SDD: 20 cm, and effective pixel size: 2 µm. Histological information: H&E staining, ×20 magnification, 0.27 µm pixel size.

previous case, MIP clusters are particles that constitute the tumor, which are not discernible in histological sections.

8.2.1.2 Solid Nests STAS As Compact Papule Expanding From Primary Tumor

The final typology to be considered in the search for STAS presence is that of solid nests (SNs). Figures 8.10(c) and 8.10(d) illustrate the presence of multiple solid papule in close proximity to the main SqCC tumor. SNs can be observed either attached to the dense structure by a narrow neck, as illustrated in Figures 8.10(a), 8.10(c) and 8.10(b), 8.10(d), or detached, as illustrated in Figure 8.7(c). In both cases, solid STAS resemble clustered purple drops, with a distinct structure from the surrounding inflammation area. Using XPCT, these structures can be observed

as compact, ball-shaped clusters extending beyond the edge of the tumor into the surrounding alveolar spaces. Some internal observations can be seen in Figures 8.10(a) and8.10(b). It seems likely that these tumor clusters tend to propagate towards the alveolar walls in order to seek additional space and facilitate further expansion, while remaining attached to the main tumor in order to allow it to continue growing.

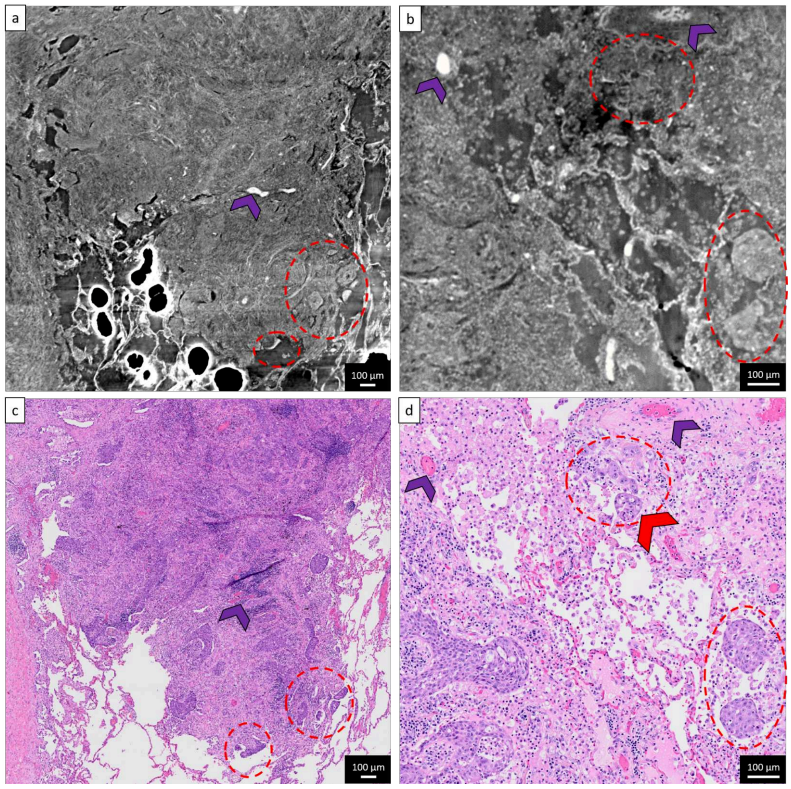

Figure 8.10. STAS pattern as Solid nests (SNs) in two types of lung cancer squamous cell carcinoma (SqCC) investigated via XPCT (a)(b) and histology (c)(d). Red dotted areas delineate the presence of SNs, while purple arrows mark the site of blood vessels. Experimental XPCT data: white beam, average X-ray energy: 21 keV, SDD: 20 cm, and effective pixel size: 2 µm. Histological information: H&E staining, ×20 magnification, 0.27 µm pixel size.

8.2.2 Pleural Invasion

Pleural invasion (Pl) in lung cancer refers to the tumor extending into the layers of the pleura, and it has important prognostic implications. The histological classification of Pl is based on how deep the tumor invades the pleura. Among the samples with

a NSCLC prognosis, thus excluding control tissues and neuroendocrine tumors, the presence of pleural invasion was assessed through histopathological examination and presented in Table 8.2. Figure 8.12 reports three stages of pleural invasion, from Pl0 to Pl2.

Pl	NSCLC tissue type	Grade	Numerosity
Pl0	Adk	G2	12
Pl0	SqCC	G3	2
Pl1	Adk	G2	3
Pl2	Adk	G2	1
Pl3	SqCC	G3	1
			19

Table 8.2. Specimen information regarding NSCLC type, tumor grade, and pleural invasion, represented here as Pl, extracted from histological diagnosis. Legends: Adk, adenocarcinoma; SqCC, squamous cell carcinoma.

The case reported in Figures 8.11(a) and 8.11(d) has no pleural invasion and this is noted by the fact that the tumor is confined within the lung parenchyma and has not reached the visceral pleura, which is the inner layer of the pleura. Elastic fibers maintain their integrity as they are easily visible as pink (for histology) and light gray (for XPCT) fibers adhere to visceral pleura. Pl1 stage of pleural invasion is represented in Figures 8.11(b) and 8.11(e), which evidences that the tumor has penetrated the visceral pleura but not beyond its elastic layer. The elastic fibers, that were easily assessable in Figures 8.11(a) and 8.11(c), are now difficult to assess as the tumor has invaded and destroyed them. Figures 8.11(c) and 8.11(f) present a case in which the elastic fibers are not intact, as pointed by red arrows, but the visceral pleura is not infiltrated. However, this case shows signs of ulceration on the pleural surface, leading to a more severe prognosis and raising the classification from Pl1 to Pl2. The presence of ulceration, highlighted by the purple dotted circle, means that the tumor has caused visible damage to the pleural tissue. This could result from the tumor's rapid growth, local inflammation, or necrosis on the pleural surface.

Figure 8.12 illustrates a Pl3 case, as shown in panels (a)(c). In this scenario, the figure is divided into two sections: one representing the pleural invaded region (Figures 8.12(a) and 8.12(c)) and the other representing the non-invaded region (Figures 8.12(b) and 8.12(d)). While the latter displays a distinct layer of adipose tissue between the parietal visceral pleura (PV) and the parietal pleura (PP), the invaded region illustrates the presence of inflammation replacing the virtual portion between the two regions. Figures 8.12(a) and 8.12(c) illustrate the extent of the tumor's invasion beyond the visceral pleura into the parietal pleura, which lines the chest wall. This is indicated by a red dotted circle. The blue dotted areas highlight the presence of a cluster of lymphocytic infiltrates, which may be associated with tumor invasion. Purple arrows indicate the presence of lymphovascular vessels.

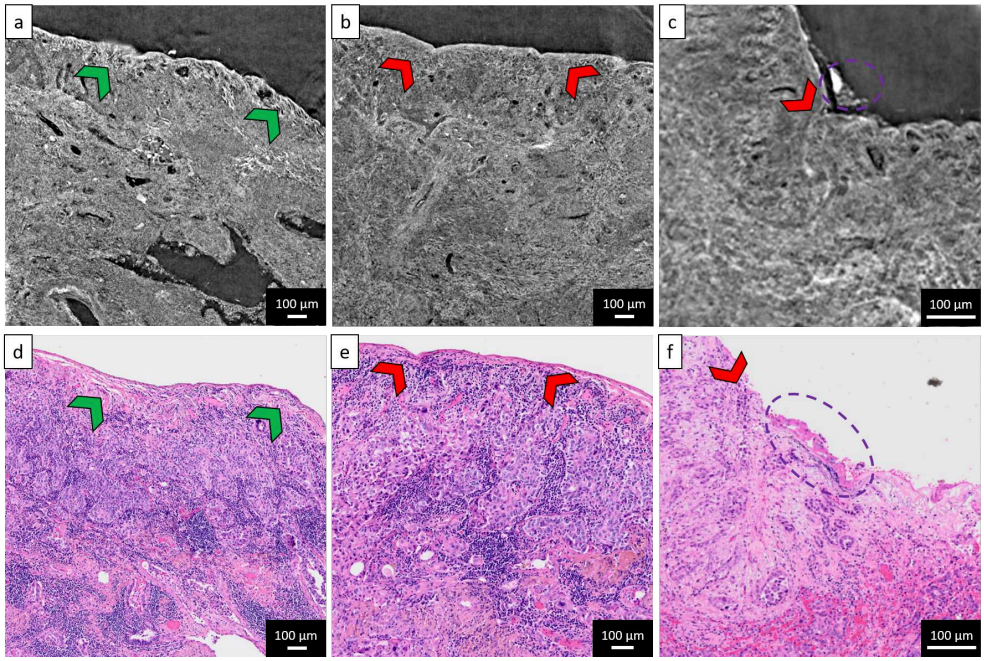

Figure 8.11. Three cases of pleural invasion (Pl) in non-small cell lung cancers via X-ray virtual histology (top panels) and traditional histology (bottom panels): (a)(d) no pleural invasion - Pl0; (b)(e) elastic fiber invasion - Pl1; (c)(f) elastic fibers invasion and signs of ulceration - Pl2. Purple dotted area highlights the ulceration. Experimental XPCT data: white beam, average X-ray energy: 21 keV, SDD: 20 cm, and effective pixel size: 2 µm. Histological information: H&E staining, ×20 magnification, 0.27 µm pixel size.

8.2.3 Lympho-Vascular Invasion

Lympho-vascular invasion (LVI) in NSCLC is an important prognostic factor that refers to the presence of cancer cells within the lymphatic system or blood vessels. In consideration of its prognostical importance, the LVI factor was subjected to examination in this study, with findings documented in NSCLC samples through histological analysis and presented in Table 8.3.

LVI definition discussed in Table 8.3, includes two types of LVI in NSCLC, which are distinguished by the involvement of the lymphatic or vascular system. Moreover, a case-of-study of neoplastic cells infiltrating into muscolar walls of an artery is presented as well. The following sections will present this classification through a discussion of a series of illustrative cases in XVH and histology correlative imaging.

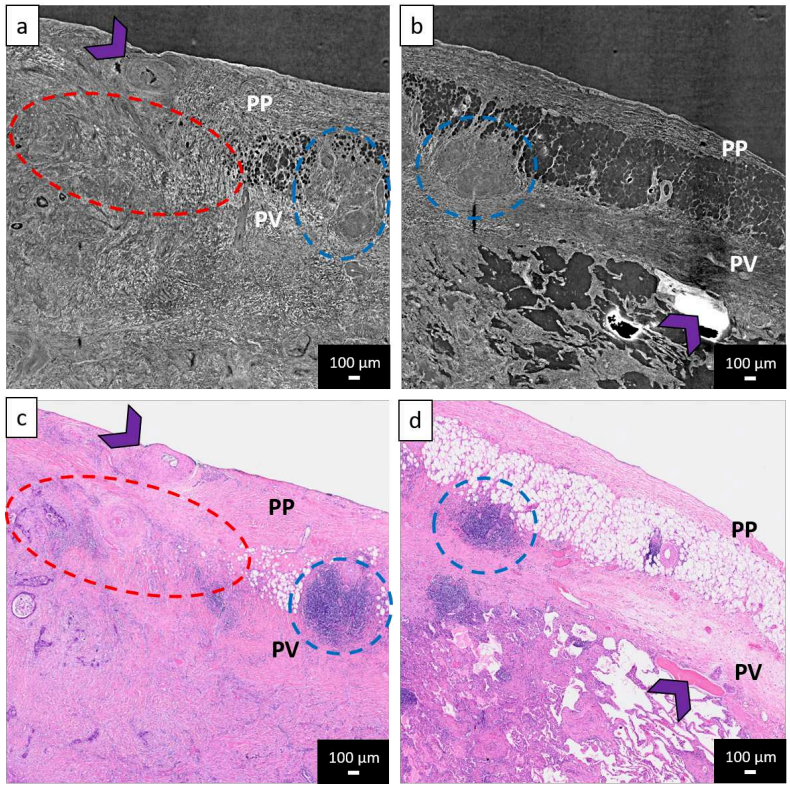

Figure 8.12. NSCLC case presenting parietal pleura invasion (Pl3) reported using X-ray virtual histology (top panels) and conventional histology (bottom panels). Modules (a) and (c) illustrate a region with visible inflammation underlined by the red dotted circle, while (b) and (d) present the region with pleural intactness. Experimental XPCT data: white beam, average X-ray energy: 21 keV, SDD: 20 cm, and effective pixel size: 2 µm. Histological information: H&E staining, ×20 magnification, 0.27 µm pixel size.

	Numerosity
LVI	6
No LVI	13
	19

Table 8.3. Specimen information regarding lymphovascular invasion, represented here as LVI, extracted from histological diagnosis. Legends: Adk, adenocarcinoma; SqCC, squamous cell carcinoma.

8.2.3.1 Lymphatic Embolism

Lymphatic invasion involves the presence of cancer cells into the lymphatic network. The Figure 8.13 presents a big artery whose lymphatic vessels are infiltrated by tumor cells. This aspect is presented by red dotted circles and arrows in Figure 8.13, where the histological section is presented alongside several serial XVH slices at different depth inside the FFPE block.

The lymphatic vessels play a pivotal role in the immune system, as they are responsible for draining lymph fluid from tissues and returning it to the bloodstream. The presence of tumor cells infiltrated into the lymphatic system is indicated by the red dotted areas, as demonstrated in the high-magnification panels extracted from the first row of images. The green circle in the XVH image at a depth of 50 µm serves to illustrate the capacity of the XVH technique to capture the valve leaflet within a lymphatic vessel. The remaining green areas indicate the presence of uninfiltrated lymphatic vessels. Indeed, as the virtual sectioning progresses to the most internal part of the tissue in the FFPE block, the lymphatic tubules appear to lack contents. This aspect is correlated with the reduction in inflammation observed at the most external level, which is accompanied by a corresponding decrease in the internal layers. The purple areas indicate the presence of a vascular network surrounding the major artery, which in some instances merges with it (see XVH images at depths 1480 and 1770 µm of Figure 8.13). Moreover, at these levels of depth, the influx of a peripheral tributary vessel into the main artery can be appreciably highlighted by the purple dotted areas and arrows. As previously mentioned, XVH is unable to ascertain with certainty whether the material in question is merely blood particles or if it contains tumor cells. Obtaining a histological image at this precise depth would definitely resolve this uncertainty. However, when considering the global tissutal context, the internal scenario appears to visibly differ from that observed in the images of the top rows of Figure 8.13. This suggests that the vessels are likely transporting standard fluids, rather than tumor cells, which would initiate an inflammatory response in the region.

Finally, from the histological perspective, the muscular composition in tunicae of the artery is highly distinguishable in XVH images, due to the property of phase-contrast to distinguish between different phases.

8.2.3.2 Vascular Invasion

Figure 8.14(b) and 8.14(d) reports two adenocarcinoma with vascular invasion in histology. The invasion of cancer cells into blood vessels testifies the facilitation of hematogenous spread, probably causing metastatis to distant lung districts and organs. Figure 8.14(d) illustrates the histological view of solid cluster of tumor cells in close proximity to blood cells and regions of inflammation. This scenario can be further analyzed in the XVH images of Figure 8.14(c) and 8.14(e), which have been captured at varying depth levels.

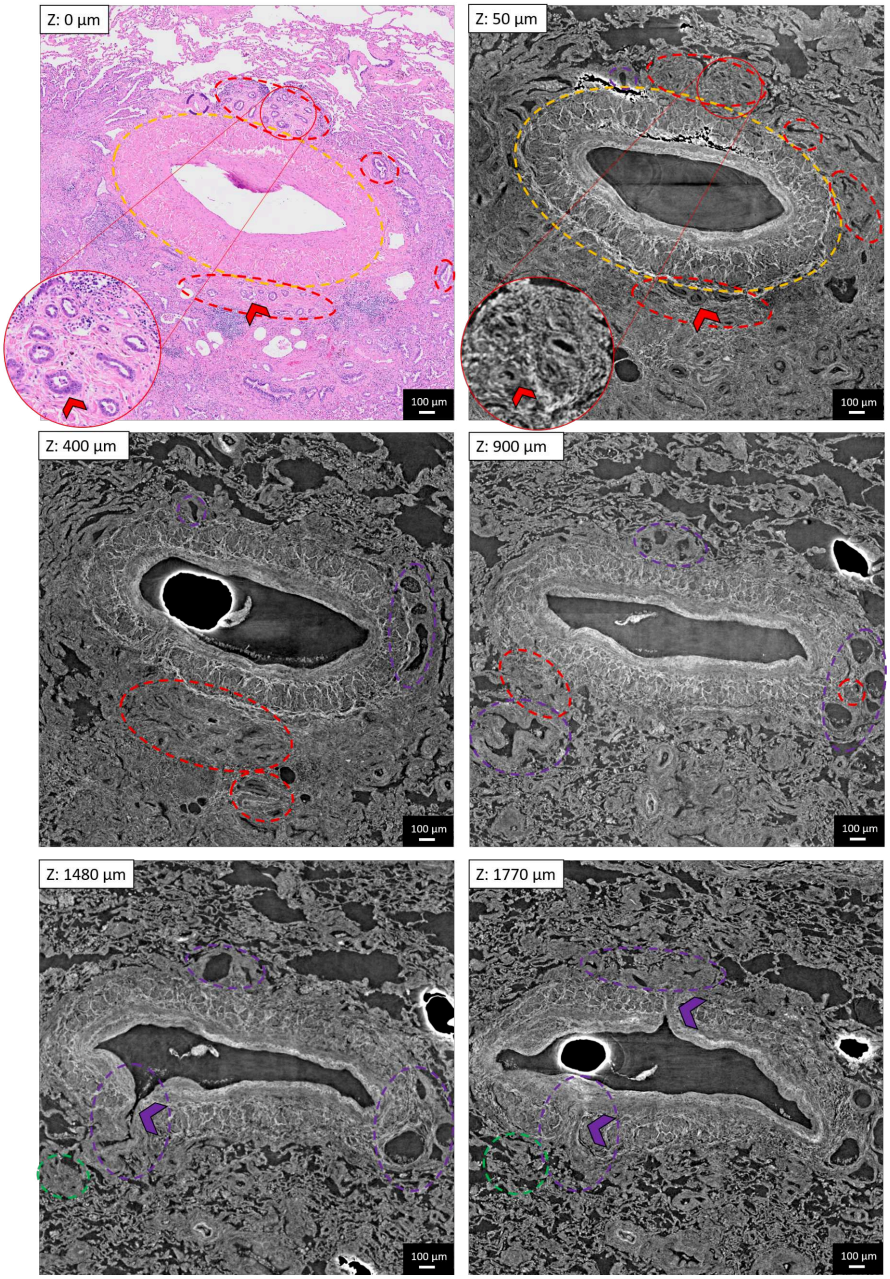

Figure 8.13. LVI as lymphatic embolism in a NSCLC adenocarcinoma. Legends of the colored areas: gold, the walls of the artery; red, lymphatic embolism in lymphatic network; green, uninfiltrated lymphatic vessels; purple, blood vessels. Experimental XPCT data: white beam, average X-ray energy: 21 keV, SDD: 20 cm, and effective pixel size: 2 µm. Histological information: H&E staining, ×20 magnification, 0.27 µm pixel size.

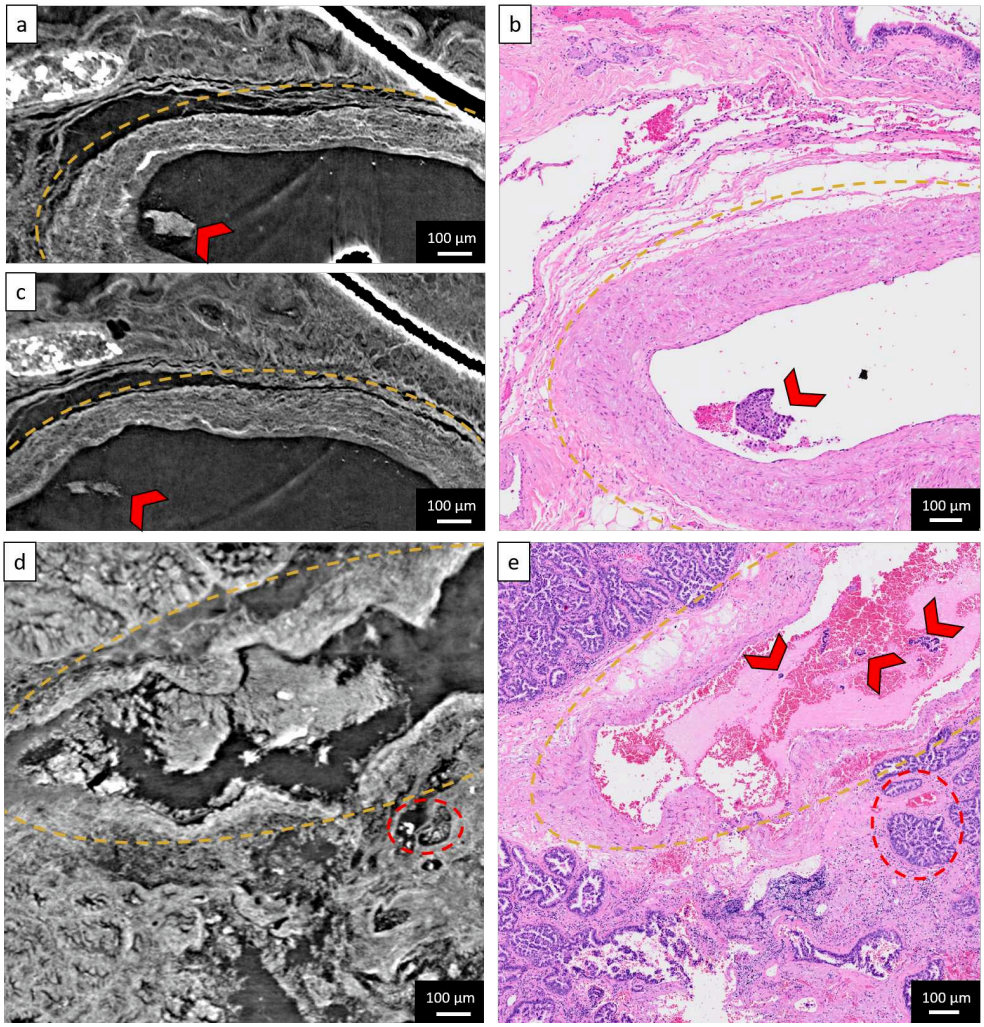

Figure 8.14. (a)(c)(d) XVH and (b)(e) histology correlative imaging ofmbolism in big veins (considered LVI) of two NSCLC cases. Gold dotted areas circle the walls of vein, while red arrows point at the presence of tumor cells within the vessels. Experimental XPCT data: white beam, average X-ray energy: 21 keV, SDD: 20 cm, and effective pixel size: 2 µm. Histological information: H&E staining, ×20 magnification, 0.27 µm pixel size.

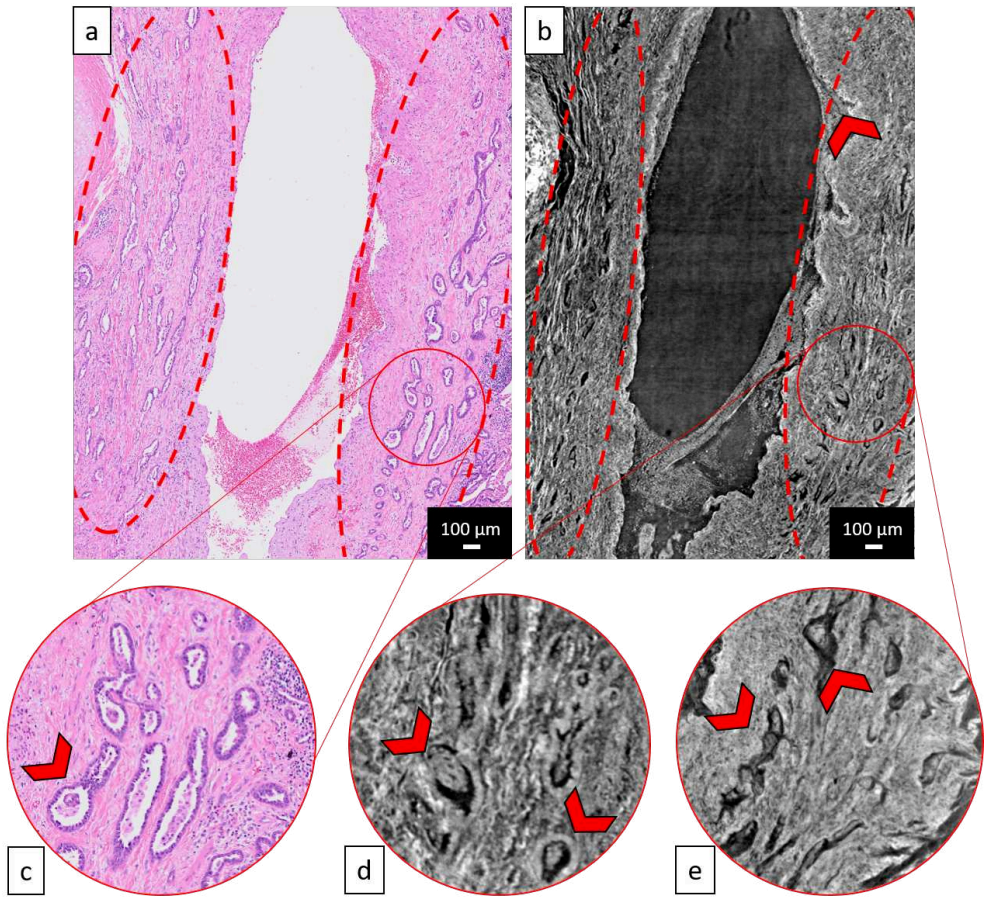

Figure 8.15. (a) Histology and (b) XVH correlative imaging of the tumor infiltration, marked by red arrows, of the muscular layer of the artery in a NSCLC case. The bottom panel shows some zoomed details of the arterial wall invasion via histology (c) and through minimum intensity projection over a volume of 50 µm depth (d)(e). Experimental XPCT data: white beam, average X-ray energy: 21 keV, SDD: 20 cm, and effective pixel size: 2 µm. Histological information: H&E staining, ×20 magnification, 0.27 µm pixel size.

The tumor cells are immersed in hemoglobin cells flow, which facilitates their diffusion through the bloodstream. Then, neoplastic embolism of micropapillary pattern in a big artery is pointed by red arrows in Figure 8.14(b). The XVH image in Figure 8.14(a), which depicts the Adk with LVI, is unable to differentiate between blood and tumor clusters. However, it does reveal the presence of high-contrast regions within the blood clots, which are likely deposits of hemosiderin, an iron-based pigment. Even though XVH lacks of cellular resolution, this example illustrates the aid of the 3D inspection. In fact, Figure 8.14(a) shows micropapillary cell clusters adjacent to a vessel that merges with a major artery exhibit thin boundaries, which facilitates the migration of these cells into the vascular network.

8.2.3.3 Arterial Walls Invasion

Neoplastic cells infiltrating the walls of an artery represent an advanced and aggressive form of LVI in all cancers, especially in NSCLC. When tumor cells penetrate the arterial wall, as in the case in Figure 8.15, it reflects the tumor's ability to breach this strong barrier, indicating an advanced capability for tissue destruction and invasion. The artery is identified by its distinctive thick wall structure, comprising several distinct layers, or tunicae, which are characteristic of this type of vessel. The most striking feature is the presence of malignant cells infiltrating through the arterial wall, resulting in disruption of the normal architectural structure, as illustrated by the red dotted panels in Figure 8.15. As displayed in Figure 8.15(c) and 8.15(d), the neoplastic cells are densely packed, forming clusters that extend into the muscular layer of the artery. However, Figure 8.15(e), which reports a minimum projection intensity obtained by an XVH volume of 50 µm depth to follow the tubular expansion in the arterial walls, demonstrates that the malignant cells do not reach the most internal epithelial layer.

This chapter presented the findings of X-ray Virtual Histology applied to invasive phenotypes of non-small cell lung cancer, including STAS, lympho-vascular invasion, and pleural invasion. These results underscore XVH's potential to enhance diagnostic accuracy and provide informative content in NSCLC. The next chapter will showcase preliminary lab-based XVH results on skin tissue preserved in FFPE blocks.

CHAPTER 9

Results - Advancements In Laboratory-Based X-ray Virtual Histology And Its Applications

Besides the synchrotron-based XVH applications previously presented, this chapter aims to explore a new way of performing X-ray virtual histology with X-ray laboratory setups.

It is evident that the times required for acquisition and total scanning in an X-ray laboratory are not directly comparable to those performed at the synchrotron. While the collection of a dataset is feasible in a few minutes at the SYRMEP beamline (Trieste, Italy), the same process is considerably more time-consuming at the OptImaTo laboratory (Trieste, Italy). Nevertheless, the ultimate goal is to make XVH accessible beyond the context of the synchrotron facility. To this end, it is necessary to conduct a comparison that will allow us to identify the factors that require improvement. Nevertheless, this chapter illustrates some initial findings from XVH applications, which underscore the necessity for further investigation in this research domain. Section 9.1 compares qualitative and quantitative data on the same melanoma tissue using two different approaches, namely lab-based PBI and synchrotron-based PBI methods. Subsequently, Section 9.2 proposes an XPCT investigation at OptImaTo laboratory to acquire multiple samples in two consecutive shots.

9.1 Comparison Of Laboratory-Based X-ray Virtual Histology Approaches

As already described in Section 4.4, this thesis employs a phase-contrast lab-based X-ray setup to explore the diagnostic potential for XVH beyond what has already been demonstrated with synchrotron light imaging. The same skin sample with a melanoma diagnosis underwent investigations in an X-ray laboratory using the PBI setup. From the reconstructed image stacks produced, a XPCT slice was extracted and matched via visual inspection, which is illustrated in Figure 9.1 together with the synchrotron image as a reference. Even though images are represented at different pixel sizes, the same tissue architecture can be appreciated.

As presented in Figure 9.1(a), the laboratory-based PBI image exhibits adequate spatial resolution and image quality. All the skin layers are readily distinguishable

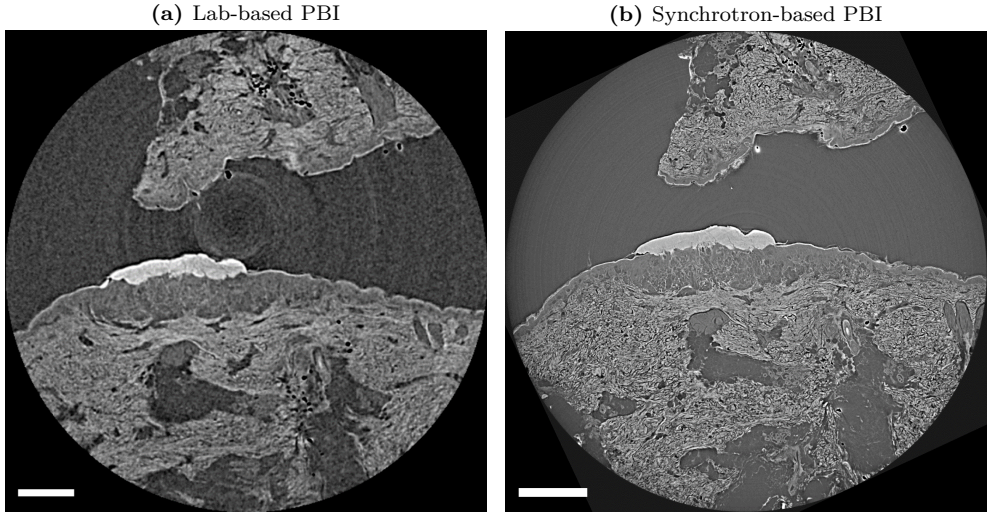

Figure 9.1. Same area of the melanoma tissue embedded in the paraffin block acquired with (a) a X-ray PBI laboratory setup at the OptImaTo lab (Trieste, Italy), and (b) by means of synchrotron based-XPCT at the SYRMEP beamline, which serves as a comparison. The scalebar is 1 mm. Experimental lab-based XPCT data: 70 kV, 3.57 mA, SSD: 38 cm, SDD: 228 cm, and effective pixel size: 12.5 µm. Experimental synchro-based XPCT data: white beam, average X-ray energy: 21 keV, SDD: 20 cm, and effective pixel size: 2.0 µm.

and a greater number of finer details are discernible. For instance, the papillary layer of the dermis, which is visible as a light gray mass, is clearly delineated as composed of connective tissue layers, such as collagen fibers. Furthermore, the lesion gains contrast and resolution, unveiling a dense melanocytic proliferation. While the dense region polluted with nests of melanocytes is readily assessable, its interpretation in diagnostic terms remains inconclusive. This is because this technique lacks the cellular resolution necessary to define the diagnostic potential.

Compared to the laboratory-based XPCT image, the synchrotron-based PBI slice in Figure 9.1(b) illustrates the unparallel spatial resolution and contrast. The collection of morphological and pathological aspects is facilitated by the micrometric level of detail, which allows for clear visualization of tumor morphology and tissue microarchitecture. All layers of the skin can be readily assessed, from the outermost thin white layer that is the stratum corneum, to the sweat glands immersed in the adipose tissue. While the cellular resolution is not discernible, the melanocytic lesion is unquestionably assessable as a symptom of carcinogenesis. This is because, at this level of resolution, the disorganized distribution of malignant melanocytic nests is discernible, and the exact area in which the lesion causes the rupture of the epidermis and provokes the ulceration can be precisely assessed. Moreover, precise assessment of tumor thickness is readily accomplished.

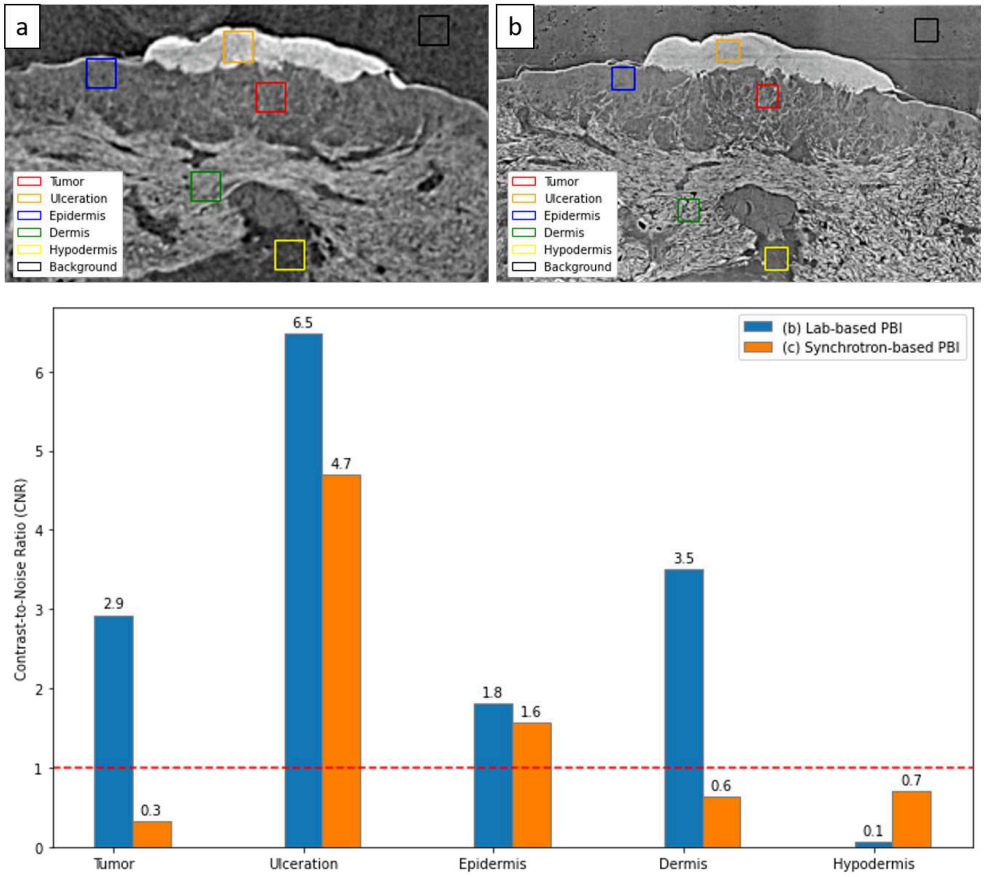

Figure 9.2. XVH images collected with a laboratory-based phase-contrast approach, (a) PBI, and compared to the synchrotron PBI approach (b). The contrast-to-noise ratio was calculated for the reported images, and the resulting values are presented in a grouped bar plot, organized by tissue region. Legend: CNR, contrast-to-noise ratio; PBI, propagation-based imaging.

As the collection of morphological and pathological aspects is critical for tissue diagnosis, CNR was computed on all laboratory- and synchrotron- based XVH images to assess tissue detectability. Results are illustrated in Figure 9.2. In general, the XVH image produced with laboratory PBI setup yields results above the unity, indicating an overall favorable appreciability of all layers of tissue. The CNR outputs of both laboratory techniques demonstrate high contrast for the dermal layer and the ulceration, due to their high pixel intensity values that are differentiate markedly distinct from the background. The tumor is clearly visible in the lab PBI method, resulting in a high degree of detail, as illustrated in Figure 9.2(a). The synchrotron results exhibited the lowest values across all categories, with the exception of hypodermis. Although the laboratory-based approach yields higher CNR values than the synchrotron-based one, this does not necessarily indicate a superior image definition. Indeed, the lowest CNR results were observed for both laboratory techniques in the hypodermal layer, which exhibited a similar noisy pattern as the reference background ROI. This is attributable to the high detectability of fine structural details in synchrotron-based images, which affects the CNR outputs.

9.2 Preliminary Results Of Lab-Based Prototype For X-ray Virtual Histology

The sandwich-like configuration employed allows to collect multiple samples in few exposures to the X-rays. Figure 9.3 illustrates the XVH reconstructed slices containing a nevus, seborrheic keratoses, a superficial spreading melanoma, and a nodular malignant melanoma.

The PBI technique provides excellent contrast for the discrimination of different skin tissue layers, from the epidermis to the dermis and hypodermis. The benign melanocytic lesion, illustrated in Figure 9.3(a), presents as a dense region of clustered melanocytes with well-defined boundaries against surrounding tissue. Furthermore, the packed skin excisions representing seborrheic keratoses demonstrate a thickened epidermis with keratin-filled structures, as indicated by the yellow arrows in Figure 9.3(b). In Figure 9.3(c), the SSM presents as an irregularly shaped lesion with heterogeneous internal structures, reflecting its invasive yet initially superficial growth pattern. Phase-contrast reveals subtle structural variations within the lesion, but elements as irregular pigment dispersion and cell density are challenging to trace. It is not possible to infer whether the lesion is benign or malignant due to the lack of cellular resolution. However, the absence of regular borders between the epidermal and dermal layers is indicative of the invasiveness pattern typical of this melanoma subtype. The nodular melanoma presented in Figure 9.3(d) is more invasive and appears as dense, rounded structures with irregular and poorly defined boundaries within the dermis. Due to their higher cellularity and tissue density, these lesions exhibit strong contrast, thereby revealing details of internal irregularity and possible disruptions to surrounding tissue. Despite the morphological information and the

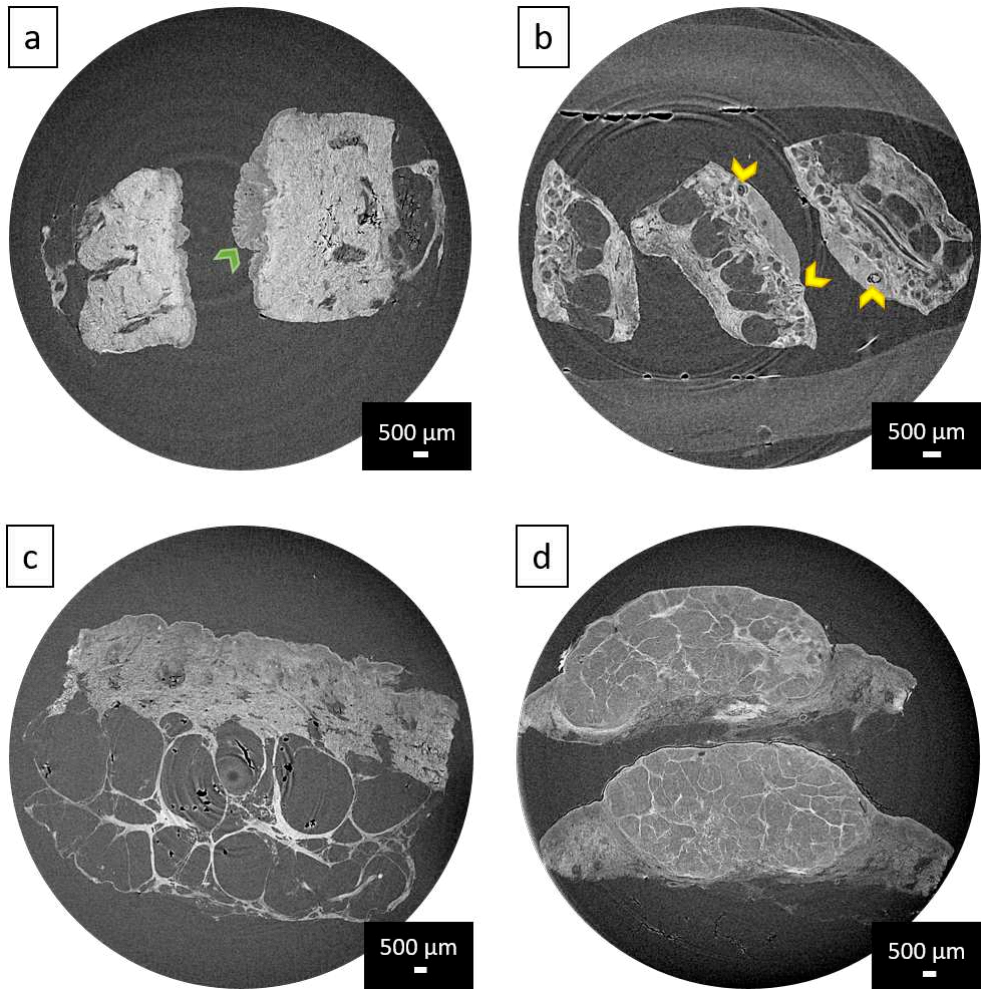

Figure 9.3. PBI lab-based XVH selected slices produced employing the sandwich configuration: (a) benign melanocytic lesions, (b) seborrheic keratoses, (c) superficial spreading melanoma, (d) nodular malignant melanoma. Experimental lab-based XPCT data: 70 kV, 3.57 mA, SSD: 38 cm, SDD: 228 cm, and effective pixel size: 12.5 µm.

high contrast for structural differences provided by this technique, the image does not provide definitive markers for distinguishing benign from malignant lesions.

The results from the lab-based XVH setup listed in this chapter have shown its ability to achieve high-resolution imaging of FFPE-preserved tissues, offering a non-destructive alternative to conventional histology and a more accessible solution beyond the constraints of synchrotron facilities. The subsequent chapter will address these findings, in conjunction with the previously obtained results, by providing a contextual framework for their significance, addressing any potential limitations, and exploring future directions for advancing imaging technologies in biomedical research.

CHAPTER 10

Discussion

The preceding chapters presented the findings of this thesis, which proposes the use of different applications of X-ray Virtual Histology in the context of specific diseases, including melanoma and NSCLC. Section 10.1 discusses the procedural improvements that facilitate enhanced visualization of tissue structures within the FFPE block. The insights gained from the methodology optimization for XVH focus on the refinement of the parameters that are typically adjusted by beamline users in order to optimize performance and provide enhanced imaging and analysis. Section 10.2 details a targeted analysis of invasive melanoma findings via XVH, from correlative imaging with histopathology to the application of a semantic segmentation model to detect melanoma in XVH images. Subsequently, Section 10.3 examines the the utility of the synchrotron-based technique in identifying characteristic patterns and invasive phenotypes in NSCLC specimens. Section 10.4 compares the XVH outcomes performed in laboratory contexts and addresses critical factors. Finally, Section 10.5 considers potential advancements and applications that could expand the role of XVH in medical research and clinical settings.

10.1 Optimization Of Methods For X-ray Virtual Histology

Chapter 5 presented the results of the tuning of the key experimental properties relevant to the optimization of the XVH technique in a synchrotron context, as conducted at the SYRMEP beamline. This section showcases a discussion of the optimization protocol, highlighting the technical adjustments made to improve image quality and also evaluating their effectiveness in overcoming common challenges such as signal attenuation and imaging artifacts.

10.1.1 Effects Of Embedding Soft Tissue In Agar And In Paraffin

Agar embedding offers the advantage of producing images with a more natural appearance, while also reducing tissue deformation. However, this method may be associated with lower contrast in comparison to more dense materials such as paraffin, and the presence of artifacts, such as air bubbles or motion artifacts. Nevertheless, it remains a valuable option for the preservation of fresh tissue, as it allows for the visualization of fine structures due to its similarity in refractive index to biological tissues.

Despite the potential of embedding fresh skin tissues in agar, the use of FFPE blocks has been shown to produce images with greater sharpness and contrast. Furthermore, it guarantees the preservation and stability of the tissue, while simultaneously reducing the occurrence of bubbles and void artifacts. Ultimately, utilizing FFPE blocks for XVH applications proves to be a more practical approach when employing correlative imaging, as it offers compatibility with the current practice in conventional histology as well as other techniques and protocols.

10.1.2 The Consequence Of Increasing Exposure Time In XPCT Experiment

As demonstrated in Section 5.3, increasing the exposure time in a synchrotron-based XPCT experiment enhances the contrast-to-noise ratio (CNR), leading to images of superior clarity. As expected, enhancing the exposure time has been demonstrated to result in higher contrast intensity, thereby rendering the image less susceptible to Poisson noise. Furthermore, as demonstrated in Section 5.3, increasing the exposure time per projection from 50 ms to 100 ms results in a significant enhancement in tumor visibility compared to the background, with a three-fold increase in CNR values.

Nevertheless, extended exposure also elevates the radiation dose, which must be meticulously managed to achieve a compromise between image quality and X-ray induced modifications in the tissue. However, upon repeating the histological sectioning procedure on the same samples used for XPCT investigation, no discernible morphological alterations were observed in the histological images in comparison to the previous one prepared for clinical diagnosis. This is due to the fact that the tissues are paraffin-embedded, and stored in blocks, thereby preserving their structural integrity. Since a very high photon flux is available at the synchrotron, heating might be a concern for prolonged measurements. However, no melting was observed in FFPE blocks, even when scans were conducted over an extended period of time. The results presented here demonstrate that XPCT does not affect the diagnostic accuracy of histology when used with tissue within FFPE blocks.

10.1.3 The Influence Of Sample Orientation In XVH Imaging

The results of an XPCT investigation of a tissue embedded in a paraffin block conducted in both vertical and horizontal orientations can have several implications in terms of image quality. The FFPE block is assumed to be composed of a rectangular or cuboidal dense layer of paraffin, which preserves the tissue inside it. Given that the X-ray beam must traverse the FFPE block to generate the projected image, it would be preferable to avoid X-rays passing through the full width and length of the sample while it rotates horizontally. On the contrary, the vertical configuration enables the X-ray beam to pass through the sample in both the lateral and axial directions. As a matter of fact, Section 5.4 demonstrates that the vertical orientation of the paraffin

block results in images of superior clarity and sharpness. Furthermore, image resolution is enhanced, enabling the capture of finer details of lung tissues, including the membrane of the acinar pattern in adenocarcinoma and the delineation of precise boundaries between tumor and healthy regions.

10.1.4 The Effect Of Distance And Pixel Size In X-ray Phase-Contrast Imaging

Two principal factors that affect the quality and characteristics of the images produced by X-ray propagation-based imaging are the propagation distance and the effective pixel size at the detector. The overall quality and effectiveness of propagation-based imaging are contingent upon an optimal combination of propagation distance and pixel size. The propagation distance controls the strength of the phase contrast and diffraction effects, while the pixel size determines the spatial resolution and the ability to sample fine details as well as the size of the FOV, thus requiring more acquisitions in a so-called "mosaic" configuration to cover the whole sample. Conversely, an overly large pixel size relative to propagation distance may fail to adequately sample diffraction patterns, leading to loss of contrast. Limited to the application of XVH at the SYRMEP beamline, the present study finds that the configuration at 2 µm pixel size and 25 cm propagation distance is a satisfactory compromise, achieving an adequate level of tissue detail while maintaining manageable data size and processing efficiency.

10.2 Evaluating Melanoma Using X-ray Virtual Histology: Interpretation Of Findings

X-ray Virtual Histology has been shown to be an effective mean of differentiating between various types of skin tumors, including melanoma, by identifying the most pertinent features. Furthermore, the non-destructive methodology proposed in this study allows for the generation of a comprehensive three-dimensional representation of the internal tissue structure, avoiding the necessity for conventional histological processing.

10.2.1 Accurate Differentiation Between Healthy And Cancerous Tissues

Chapter 6 showed that benign aspects can be investigated, such as seborrhoeic keratosis, which can be detected in the epidermal layer. More interestingly, basal cell carcinomas can be reconstructed three-dimensionally to understand their invasivity properties, and pagetoid distributions of neoplastic cells as well as nested melanoma

inside the skin layers can be investigated and analyzed three-dimensionally. Furthermore, XVH allows for the distinction between an ulceration and a simple clot resulting from sample preparation, which is of particular importance in the context of blood overlaying a tumor. Indeed, by virtually sectioning the entire XVH volume, it is possible to establish whether the epidermis is intact or compromised, thereby demonstrating the association between epidermal consumption and ulceration [150].

10.2.2 Automatic Segmentation Tool For Melanocytic Lesion Detection And Computation Of 3D Breslow Thickness

In chapter 7, the employment of deep learning-based networks for the detection of atypical melanocytic proliferation and the presence of ulceration in XVH volumes has been demonstrated to be beneficial in both feature extraction and analysis measurements.

Firstly, the automatic detection of melanocytic lesions offers insights into the spatial distribution of the tumor. The reconstruction of three-dimensional melanomas allows for the comprehension of their structural morphology, as it enables the segmentation of the most invasive properties of melanoma. For instance, melanomas that grow in a radial pattern were observed to exhibit an irregular superficial distribution due to the presence of nested melanoma and pagetoid diffusion, which spread horizontally but rarely vertically. Conversely, some nodular melanomas were found to be composed of multiple nodules growing in close proximity to one another, particularly in cases where one nodule undergoes necrosis, resulting in the formation of another nearby.

A second aspect meriting consideration is the assessment of XVH-retrieved measurements for the purpose of performing quantitative analysis, including the analysis of surfaces and volumes. It is of particular interest to consider the potential of XVH to perform a three-dimensional assessment of melanoma depth, leading to the so-called Breslow thickness. This measurement, which in conventional histology is derived from a single two-dimensional observation, was retrieved by considering the maximum extension of the deepest tumor cell to the epidermis in a skin volume with a depth of 0.5 mm inside the paraffin block. As melanocytic lesions exhibit considerable variation in shape, size, and pattern, the provision of a three-dimensional context in pathological tissue may facilitate the accurate assessment of the maximum extent of tumor depth. Nevertheless, although the use of previously dissected tissue was employed in this study to avoid any alteration to clinical diagnostic practice, the XVH method could be conducted prior to a fresh histopathological examination of excised skin tissue. This could facilitate the identification of atypical melanocytic lesions without the necessity for sectioning, or assist the pathologist in selecting the optimal slice for further molecular examination.

The relatively poor results obtained for the semantic segmentation model, particularly in terms of the dice score, may be attributed to the presence of imprecise manual annotations and a limited availability of data. While histology provides detailed visu-

alization of cellular and subcellular structures, XVH offers a broader understanding of the overall morphological characteristics of these elements. In the process of transferring the annotations from histology to XVH, there is a possibility that the manual annotations may have been imprecise in the delineation of nests of melanomas and atypical melanocyte borders. Nevertheless, the deep learning model demonstrated the capacity to discern patterns and to perform pixel-wise segmentation, effectively delineating the boundaries of atypical melanocytic lesions.

Ultimately, the data were selected for XVH in accordance with the allocated experimental time at the synchrotron. Nevertheless, this study illustrates the capacity of a well-balanced deep learning model to function effectively even when confronted with restricted data.

10.3 Key Findings Of X-ray Virtual Histology In The NSCLC Study

X-ray Virtual Histology has been demonstrated to be an effective technique that can be used as a support in the diagnosis of non-small cell lung cancers. It has the potential to fill the gap between the clinical explorative imaging made by CT or PET, and the diagnostical one of conventional histopathology in the diagnosis of lung cancer.

10.3.1 Discrimination Between Different Types Of Cancerous Tissues

Even though XVH cannot assess cellular resolution as histology does, it demonstrates to be a valid tool in distinguish different NSCLC types, from adenocarcinoma types to squamous cell carcinoma. As a result, the infiltrative properties of Adk types and SqCC can be assessed through the observation of its microarchitecture. Moreover, the morphological perspective provided by XVH helps to define the stage of the progression of the tumor from the thickening of the alveolar walls to the progressively growing and diffusing of singular and clustered neoplastic cells. XVH approach provides great contrast in the discrimination between the inflammation and the tumor area. Moreover, vascular and lymphatic networks are greatly assessable.

10.3.2 Assessment Of Invasive Properties In NSCLC

As significant invasive properties in NSCLC that markedly influence prognosis and treatment strategies, XVH investigation has been utilized to examine the spread through air spaces (STAS), pleural invasion, and lympho-vascular invasion (LVI).

Collectively, these characteristics serve as crucial pathological indicators, elucidating the invasive propensity of the tumor and informing therapeutic decisions in the management of lung cancer.

Spread Trough Air Spaces STAS is a recently identified invasive pattern in histopathology [146]. It occurs when tumor cells detach and spread within the alveolar spaces of the lung, without direct invasion of blood vessels or lymphatics.

Although some types of STAS appear as floating structures in two-dimensional histological sections, they merely represent the margins of the tumor mass in three-dimensional virtual histology as reported in Section 8.2.1. Other floating STAS observed in the histological image were found to be attached to adjacent vessels or alveolar walls through virtual XPCT sectioning, which enables the tracking of such tumor cells adhering to these structures.

Synchrotron XVH permits three-dimensional non-destructive visualization of biological elements, thereby facilitating the reconstruction of tumor morphology and the tracking of STAS attachment to other supporting structures, including primary tumors, alveolar walls, and blood vessels.

These findings lend support to the opinions proposed by [151–153] that the prognostic significance of STAS requires careful evaluation, given that all floating STAS were ultimately found to be connected to one or more supporting structures, including alveolar walls and lympho-vascular vessels. In the majority of cases, these structures were also connected to the primary tumor.

Pleural Invasion Pleural invasion is defined as the penetration of tumor cells into the layers of the pleura, which is indicative of the tumor's progressive and aggressive behavior as it spreads through the pleural layers.

Section 8.2.2 describes how synchrotron X-ray imaging facilitated the identification of structural alterations, including the thickening of the visceral pleura or disruption of the typical pleural architecture, which points to tumor invasion. Furthermore, the visualization of elastic fibers is more readily assessable via X-ray virtual histology, as these structures exhibit greater contrast than those in histology. Conversely, the distinction between type Pl0 and Pl1 is relatively straightforward.

Finally, a three-dimensional investigation can reveal the evolution of the tumor mass in proximity to the pleura, thus facilitating the determination of whether a deeper invasion is present. Indeed, the ability to virtually section tissue using XPCT allows for the examination of larger regions and the delineation of the progression of invasion into resected lung tissue.

Lympho-Vascular Invasion Lympho-vascular invasion (LVI) is defined as the presence of tumor cells within the lymphatic or blood vessels. This facilitates the spread of cancer to regional lymph nodes and distant organs, and is associated with an elevated risk of recurrence and metastasis.

Although XVH is a highly detailed imaging technique, it is not typically employed for the direct diagnosis of LVI in NSCLC. This is because, as previously underlined in Section 8.2.3, XVH can provide high-resolution images of tissue architecture and can be useful for assessing tumor structure and vascular features. However, it lacks the cellular resolution needed to definitively identify cancer cells within lymphatic or blood vessels, which is required to diagnose LVI. In particular, the most challenging aspect is the discrimination between erythrocytes, blood particles, inflammatory fluids, and tumor clusters or cells. Nevertheless, even though XVH offers insight into gross anatomical features, it is instrumental in the analysis of tumor vasculature and the mapping of its three-dimensional structure.

10.4 Assessment Of Image Quality In Laboratory-Based X-ray Virtual Histology

Chapter 9 proposed an investigation employing a laboratory X-ray imaging source to perform X-ray Virtual Histology, and correlate them with synchrotron XVH imaging. The lab-based PBI technique offers a range of advantages, contingent upon the specific research and diagnostic objectives. As evidenced by the findings detailed in Section 9.1, lab-based PBI is particularly adept at providing contrast-enhanced visualization of soft tissue, showcasing a remarkable level of tissue detail for a laboratory instrumentation. Conversely, synchrotron-based imaging is distinguished by its exceptional resolution and contrast, particularly for in-depth melanoma tissue analysis, though its use is restricted to specialized facilities. The comparison of these two imaging techniques allows for the identification of shortcomings that require further investigation and potential improvement. One is the enhancement of image spatial resolution, which would facilitate the assessment of diagnoses. Together, these imaging modalities provide a comprehensive multi-scale toolkit approach for non-invasive XVH, allowing researchers to tailor their approach based on the level of detail and resources available.

The “sandwich”-based approach considers a potential configuration to use in the clinical context to scan more samples at the same time. FFPE blocks, that do not show any X-ray alterations, were internally inspected producing intriguing three-dimensional insights of the pathology. Despite the inability to obtain a complete clinical diagnosis due to the modest spatial resolution, the results can be effectively integrated with histopathology to examine the internal tumor spread within the FFPE block. While this technique provides excellent contrast for observing tissue structures, borders, and internal heterogeneity, it lacks the specificity needed to distinguish benign from malignant lesions definitively. This limitation arises because malignancy is determined by cellular and molecular characteristics not visualized purely by structural contrast.

10.5 Future Perspectives Of X-ray Virtual Histology

X-ray virtual histology is expected to achieve even greater spatial resolution, approaching the level of traditional microscopy, and allowing for the visualization of cellular and subcellular structures without needing tissue excision. This is not only in synchrotron facilities, in which the nanoscale resolution can be achieved, but also in laboratory settings.

The future perspective of XVH holds significant promise for advancing diagnostic capabilities, where non-invasive high-resolution imaging is critical for assessing tumor characteristics and invasiveness. As this technology evolves, several key advancements and potential applications can be proposed, from non-invasive histopathology support to real-time tumor assessment.

Moreover, efforts to miniaturize high-resolution X-ray imaging systems could lead to more accessible and cost-effective solutions, enabling wider adoption in clinical diagnostics. Technological advancement is progressing towards the integration of high-resolution detectors and X-ray metal-jet sources, while the refinement of phase-contrast imaging modalities is demonstrating promising applications. Moreover, the subsequent phase of advancement in XVH will necessitate the formulation of standardized protocols for the acquisition and analysis of XVH images, in addition to the development of robust algorithms for data interpretation.

Another interesting aspect is to consider the integration of cutting-edge technologies such as DL and ML tools in XVH, that can have a significant impact in data processing and analysis. They have the potential to automate key steps in image analysis, such as tissue segmentation and pattern recognition, allowing for faster and more accurate interpretation of complex 3D datasets.

Another promising direction is the development of multimodal imaging approaches that combine XVH with techniques like MRI or Optical Coherence Tomography (OCT), providing a comprehensive view of tissue structure and function.

10.5.1 Towards The Inclusion Of X-ray Virtual Histology Into Computational Pathology?

The integration of XVH into computational pathology represents a significant advancement in the diagnostic and analytical capabilities of medical imaging. XVH provides high-resolution imaging that delivers detailed structural and compositional information about tissues, enabling pathologists to visualize and analyze specimens without traditional histological preparation. Incorporating XVH into computational pathology not only facilitates the assessment of tumor microenvironments but also supports more accurate diagnoses and treatment planning. This approach enhances the characterization of various tumors, including melanoma, by offering valuable three-dimensional insights into tumor architecture, cellularity, and vascularization, thereby complementing conventional histology.

However, unlike traditional histology, which allows for the examination of individual cells and their specific morphologies, state-of-the-art XVH cannot assess cellular details critical for accurate diagnosis and characterization of diseases, such as identifying subtle changes in cellular morphology or distinguishing between closely related cell types. Therefore, while XVH is a powerful tool for visualizing tissue properties, it is often used alongside other imaging modalities or histological techniques to provide a more comprehensive understanding of tissue pathology.

These aspects have the potential of facilitating the dissemination of XVH technology through the implementation of transparent and open access protocols, thereby enabling simplified integration within the domain of clinical pathology.

CHAPTER 11

Conclusion

This thesis presents the development of methods for XVH of biological samples using XPCT in both synchrotron and laboratory settings. A broad range of synchrotron-based XVH applications has been presented, where the acquisition, reconstruction, and data processing have been optimized for each sample. Specifically, imaging has been conducted on unstained samples, employing phase-contrast imaging to augment contrast for weakly attenuating materials, especially soft tissue.

The technique has demonstrated particular promise for the study of melanoma and NSCLC, where detailed tissue visualization can enhance diagnostic accuracy, improve treatment monitoring, and facilitate a more comprehensive understanding of tumor progression and the tumor microenvironment. By providing non-destructive high-resolution three-dimensional imaging, this technology has the potential of transforming the study of complex cancers, such as melanoma and NSCLC, by capturing both tissue architecture and molecular details. In particular, while clinical CT scans may lack the requisite resolution to detect subtle tissue changes (e.g., those associated with tumor invasion in melanoma and with pleural invasion in NSCLC), XVH can serve as an intermediate step in providing more detailed structural information that is complementary to that provided by histology.

Although the results are not as comprehensive as those produced by synchrotron facilities, laboratory-based XVH has been effectively utilized to examine distinct skin tumors, with the objective of defining the early progression of melanoma and assessing potential diagnostic modalities. In particular, laboratory-based XVH offers a promising and accessible alternative for broader application, thereby accelerating research on the progression of the disease. Furthermore, as technology progresses, it is expected that the role of XVH in cancer diagnosis and research will become increasingly prominent, ultimately contributing to the advancement of clinical diagnostics and cancer research.

Bibliography

[1] A. G. Nicholson, M. S. Tsao, M. B. Beasley, A. C. Borczuk, E. Brambilla, W. A. Cooper, S. Dacic, D. Jain, K. M. Kerr, S. Lantuejoul, M. Noguchi, M. Papotti, N. Rekhtman, G. Scagliotti, P. van Schil, L. Sholl, Y. Yatabe, A. Yoshida, and W. D. Travis, "The 2021 who classification of lung tumors: Impact of advances since 2015," *Journal of Thoracic Oncology*, vol. 17, 2022.

[2] P. A. Jones and S. B. Baylin, "The epigenomics of cancer," *Cell*, vol. 128, no. 4, pp. 683–692, 2007.

[3] A. M. Lewandowska, M. Rudzki, S. Rudzki, T. Lewandowski, and B. Laskowska, "Environmental risk factors for cancer-review paper," *Annals of Agricultural and Environmental Medicine*, vol. 26, no. 1, pp. 1–7, 2018.

[4] D. Xiang, S. Hu, T. Mai, X. Zhang, L. Zhang, S. Wang, K. Jin, and J. Huang, "Worldwide cancer statistics of adults over 75 years old in 2019: a systematic analysis of the global burden of disease study 2019," *BMC Public Health*, vol. 22, 2022.

[5] R. L. Siegel, K. D. Miller, H. E. Fuchs, and A. Jemal, "Cancer statistics, 2022," *CA: A Cancer Journal for Clinicians*, vol. 72, no. 1, pp. 7–33, 2022.

[6] M. Wong, X. Lao, K. Ho, W. B. Goggins, and S. L. A. Tse, "Incidence and mortality of lung cancer: global trends and association with socioeconomic status," *Scientific Reports*, vol. 7, 2017.

[7] X. Ji, J. Chen, J. Ye, S. Xu, B. Lin, and K. Hou, "Epidemiological analysis of global and regional lung cancer mortality: Based on 30-year data analysis of global burden disease database," *Healthcare*, vol. 11, no. 22, 2023.

[8] A. Jamil and A. Kasi, *Lung Metastasis*, ch. Etiology. Treasure Island (FL): StatPearls Publishing, 2024.

[9] N. H. Matthews, W.-Q. Li, A. A. Qureshi, M. A. Weinstock, and E. Cho, "Epidemiology of melanoma," *Cutaneous Melanoma: Etiology and Therapy*, 2017.

[10] A. C. Geller and G. D. Annas, "Epidemiology of melanoma and nonmelanoma skin cancer," *Seminars in oncology nursing*, 2003.

[11] H. Sung, J. Ferlay, R. L. Siegel, M. Laversanne, I. Soerjomataram, A. Jemal, and F. Bray, "Global cancer statistics 2020: Globocan estimates of incidence and mortality worldwide for 36 cancers in 185 countries," *CA: A Cancer Journal for Clinicians*, vol. 71, no. 3, pp. 209–249, 2021.

[12] D. L. Narayanan, R. N. Saladi, and J. L. Fox, "Review: Ultraviolet radiation and skin cancer," *International Journal of Dermatology*, vol. 49, no. 9, pp. 978–986, 2010.

[13] M.-F. Demierre, "Epidemiology and prevention of cutaneous melanoma," *Current Treatment Options in Oncology*, vol. 7, 2006.

[14] K. Kaidbey, "The photoprotective potential of the new superpotent sunscreens," *J Am Acad Dermatol*, vol. 22, 1990.

[15] R. Scolyer, R. Rawson, J. Gershenwald, P. Ferguson, and V. Prieto, "Melanoma pathology reporting and staging," *Modern Pathology*, 2020.

[16] J. E. Gershenwald, R. A. Scolyer, K. R. Hess, V. K. Sondak, G. V. Long, M. I. Ross, A. J. Lazar, M. B. Faries, J. M. Kirkwood, G. A. McArthur, L. E. Haydu, A. M. M. Eggermont, K. T. Flaherty, C. M. Balch, J. F. Thompson, and for members of the American Joint Committee on Cancer Melanoma Expert Panel and the International Melanoma Database and Discovery Platform , "Melanoma staging: Evidence-based changes in the american joint committee on cancer eighth edition cancer staging manual," *CA: A Cancer Journal for Clinicians*, vol. 67, no. 6, pp. 472–492, 2017.

[17] M. A. Jafry, S. Peacock, A. C. Radick, H. L. Shucard, L. M. Reisch, M. W. Piepkorn, S. R. Knezevich, M. A. Weinstock, R. L. Barnhill, D. E. Elder, K. F. Kerr, and J. G. Elmore, "Pathologists' agreement on treatment suggestions for melanocytic skin lesions," *Journal of the American Academy of Dermatology*, vol. 82, no. 6, pp. 1435–1444, 2020.

[18] J. G. Elmore, D. E. Elder, R. L. Barnhill, S. R. Knezevich, G. M. Longton, L. J. Titus, M. A. Weinstock, M. S. Pepe, H. D. Nelson, L. M. Reisch, A. C. Radick, and M. W. Piepkorn, "Concordance and reproducibility of melanoma staging according to the 7th vs 8th edition of the ajcc cancer staging manual," *JAMA Network Open*, vol. 1, pp. e180083–e180083, 05 2018.

[19] E. Z. Keung and J. E. Gershenwald, "The eighth edition american joint committee on cancer (ajcc) melanoma staging system: Implications for melanoma treatment and care," *Expert Review of Anticancer Therapy*, 2018.

[20] S. Pathak and P. Zito, "Clinical guidelines for the staging, diagnosis, and management of cutaneous malignant melanoma," *StatPearls Publishing*, 2024.

[21] C. R. UK, "Melanoma stages." `https://www.cancerresearchuk.org/about-cancer/melanoma/stages-types/tnm-staging`. [Online; Accessed October-06-2024].

[22] A. Cherobin, A. Wainstein, E. Colosimo, E. Goulart, and F. Bittencourt, "Prognostic factors for metastasis in cutaneous melanoma," *An Bras Dermatol*, 2018.

[23] Z. Barricklow, M. DiVincenzo, C. Angell, and W. Carson, "Ulcerated cutaneous melanoma: A review of the clinical, histologic, and molecular features associated with a clinically aggressive histologic phenotype," *Clin Cosmet Investig Dermatol*, 2022.

[24] M. L. Bønnelykke-Behrndtz, H. Schmidt, I. J. Christensen, T. E. Damsgaard, H. J. Møller, L. Bastholt, P. H. Nørgaard, and T. Steiniche, "Prognostic Stratification of Ulcerated Melanoma: Not Only the Extent Matters," *American Journal of Clinical Pathology*, vol. 142, pp. 845–856, 12 2014.

[25] E. C. Paver, T. Ahmed, H. Burke, R. P. M. Saw, J. R. Stretch, A. J. Spillane, K. F. Shannon, I. A. Vergara, D. E. Elder, S. N. Lo, J. F. Thompson, and R. A. Scolyer, "Prognostic Significance of Incipient Ulceration in Primary Cutaneous Melanoma," *JAMA Dermatology*, vol. 159, pp. 1359–1367, 12 2023.

[26] L. M. Duncan, "The classification of cutaneous melanoma," *Hematology/Oncology Clinics of North America*, vol. 23, no. 3, pp. 501–513, 2009. Advances in Melanoma.

[27] S. N. Lo, R. A. Scolyer, and J. F. Thompson, "Long-term survival of patients with thin (t1) cutaneous melanomas: A breslow thickness cut point of 0.8 mm separates higher-risk and lower-risk tumors," *Ann Surg Oncol*, 2018.

[28] S. N. Leilabadi, A. Chen, S. Tsai, V. Soundararajan, H. Silberman, and A. K. Wong, "Update and review on the surgical management of primary cutaneous melanoma," *Healthcare*, vol. 2, no. 2, pp. 234–249, 2014.

[29] D. Ogata, K. Namikawa, A. Takahashi, and N. Yamazaki, "A review of the AJCC melanoma staging system in the TNM classification (eighth edition)," *Japanese Journal of Clinical Oncology*, vol. 51, pp. 671–674, 03 2021.

[30] L. M. Duncan, M. Berwick, J. A. Bruijn, H. R. Byers, M. C. Mihm, and R. L. Barnhill, "Histopathologic recognition and grading of dysplastic melanocytic nevi: An interobserver agreement study," *Journal of Investigative Dermatology*, vol. 100, no. 3, Supplement, pp. S318–S321, 1993.

[31] D. E. Elder, M. W. Piepkorn, R. L. Barnhill, G. M. Longton, H. D. Nelson, S. R. Knezevich, M. S. Pepe, P. A. Carney, L. J. Titus, T. Onega, A. N. Tosteson, M. A. Weinstock, and J. G. Elmore, "Pathologist characteristics associated with accuracy and reproducibility of melanocytic skin lesion interpretation," *Journal of the American Academy of Dermatology*, vol. 79, no. 1, pp. 52–59.e5, 2018.

[32] K. F. Kerr, D. E. Elder, M. W. Piepkorn, S. R. Knezevich, M. M. Eguchi, H. L. Shucard, L. M. Reisch, J. G. Elmore, and R. L. Barnhill, "Pathologist characteristics associated with rendering higher-grade diagnoses for melanocytic lesions," *JAMA Dermatology*, vol. 159, pp. 1315–1322, 12 2023.

[33] G. W. Warren and K. M. Cummings, "Tobacco and lung cancer: Risks, trends, and outcomes in patients with cancer," *American Society of Clinical Oncology Educational Book*, no. 33, pp. 359–364, 2013.

[34] T. Walser, X. Cui, J. Yanagawa, J. M. Lee, E. Heinrich, G. Lee, S. Sharma, and S. M. Dubinett, "Smoking and lung cancer," *Proceedings of the American Thoracic Society*, vol. 5, no. 8, pp. 811–815, 2008.

[35] M. J. Thun, C. A. Lally, E. E. Calle, J. Heath, Clark W., J. T. Flannery, and W. D. Flanders, "Cigarette Smoking and Changes in the Histopathology of Lung Cancer," *JNCI: Journal of the National Cancer Institute*, vol. 89, pp. 1580–1586, 11 1997.

[36] C.-H. Tseng, C.-J. Chiang, J.-S. Tseng, T.-Y. Yang, K.-H. Hsu, K.-C. Chen, C.-L. Wang, C.-Y. Chen, S.-H. Yen, C.-M. Tsai, M.-S. Huang, C.-C. Ho, C.-J. Yu, Y.-H. Tsai, J.-S. Chen, T.-Y. Chou, M.-H. Tsai, H.-Y. Chen, K.-Y. Su, J. J. Chen, H.-W. Chen, S.-L. Yu, T.-W. Liu, and G.-C. Chang, "Egfr mutation, smoking, and gender in advanced lung adenocarcinoma," *Oncotarget*, vol. 8, no. 58, pp. 98384–98393, 2017.

[37] J. M. Samet, "Carcinogenesis and lung cancer: 70 years of progress and more to come," *Carcinogenesis*, vol. 41, pp. 1309–1317, 09 2020.

[38] J. Malhotra, M. Malvezzi, E. Negri, C. La Vecchia, and P. Boffetta, "Risk factors for lung cancer worldwide," *European Respiratory Journal*, vol. 48, no. 3, pp. 889–902, 2016.

[39] S. Feng and S. Yang, "The new 8th tnm staging system of lung cancer and its potential imaging interpretation pitfalls and limitations with ct image demonstrations," *Diagn Interv Radiol*, vol. 25, no. 4, pp. 270–279, 2019.

[40] F. C. Detterbeck, D. J. Boffa, and L. T. Tanoue, "The new lung cancer staging system," *Chest*, vol. 136, no. 1, pp. 260–271, 2009.

[41] P.-K. Hsu, H.-C. Huang, C.-C. Hsieh, H.-S. Hsu, Y.-C. Wu, M.-H. Huang, and W.-H. Hsu, "Effect of formalin fixation on tumor size determination in stage i non-small cell lung cancer," *The Annals of Thoracic Surgery*, vol. 84, no. 6, pp. 1825–1829, 2007.

[42] G. A. Woodard, K. D. Jones, and D. M. Jablons, *Lung Cancer Staging and Prognosis*, pp. 47–75. Cham: Springer International Publishing, 2016.

[43] M. Yasukawa, N. Sawabata, T. Kawaguchi, N. Kawai, T. Nakai, C. Ohbayashi, and S. Taniguchi, "Histological grade: Analysis of prognosis of non-small cell lung cancer after complete resection," *In Vivo*, vol. 32, no. 6, pp. 1505–1512, 2018.

[44] C. F. Mountain, D. T. Carr, and W. A. D. Anderson, "A system for the clinical staging of lung cancer," *American Journal of Roentgenology*, vol. 120, no. 1, pp. 130–138, 1974. Publisher: American Roentgen Ray Society.

[45] T. Osaki, A. Nagashima, T. Yoshimatsu, S. Yamada, and K. Yasumoto, "Visceral pleural involvement in nonsmall cell lung cancer: prognostic significance," *The Annals of Thoracic Surgery*, vol. 77, no. 5, pp. 1769–1773, 2004. Publisher: Elsevier.

[46] A. Kawase, J. Yoshida, E. Miyaoka, H. Asamura, Y. Fujii, Y. Nakanishi, K. Eguchi, M. Mori, N. Sawabata, M. Okumura, and K. Yokoi, "Visceral pleural invasion classification in non–small-cell lung cancer in the 7th edition of the tumor, node, metastasis classification for lung cancer: Validation analysis based on a large-scale nationwide database," *Journal of Thoracic Oncology*, vol. 8, no. 5, pp. 606–611, 2013. Publisher: Elsevier.

[47] S. P. Hammar, *Pleural Diseases*, pp. 1463–1579. New York, NY: Springer New York, 1994.

[48] P. Goldstraw, J. Crowley, K. Chansky, D. J. Giroux, P. A. Groome, R. Rami-Porta, P. E. Postmus, V. Rusch, and L. Sobin, "The iaslc lung cancer staging project: Proposals for the revision of the tnm stage groupings in the forthcoming (seventh) edition of the tnm classification of malignant tumours," *Journal of Thoracic Oncology*, 2007.

[49] C. C. Compton, D. R. Byrd, J. Garcia-Aguilar, S. H. Kurtzman, A. Olawaiye, and M. K. Washington, *Lung*, pp. 311–328. New York, NY: Springer New York, 2012.

[50] S. Lu, K. S. Tan, K. Kadota, T. Eguchi, S. Bains, N. Rekhtman, P. S. Adusumilli, and W. D. Travis, "Spread through air spaces (stas) is an independent predictor of recurrence and lung cancer - specific death in squamous cell carcinoma," *Journal of Thoracic Oncology*, 2017.

[51] Y. Han, H. Kim, and M. Mino-Kenudson, "Tumor spread through air spaces (stas): prognostic significance of grading in non-small cell lung cancer," *Modern Pathology*, 2020.

[52] A. Warth, "Spread through air spaces (stas): prognostic impact of a semi-quantitative assessment," *Journal of Thoracic Disease*, vol. 9, no. 7, 2017.

[53] A. Sedlis, B. N. Bundy, M. Z. Rotman, S. S. Lentz, L. I. Muderspach, and R. J. Zaino, "A randomized trial of pelvic radiation therapy versus no further therapy in selected patients with stage IB carcinoma of the cervix after radical hysterectomy and pelvic lymphadenectomy: A gynecologic oncology group study," *Gynecologic Oncology*, vol. 73, no. 2, pp. 177–183, 1999.

[54] T.-Y. Huang, L.-P. Hsu, Y.-H. Wen, T.-T. Huang, Y.-F. Chou, C.-F. Lee, M.-C. Yang, Y.-K. Chang, and P.-R. Chen, "Predictors of locoregional recurrence in early stage oral cavity cancer with free surgical margins," *Oral Oncology*, vol. 46, no. 1, pp. 49–55, 2010.

[55] C.-P. Hsu, J.-Y. Hsia, G.-C. Chang, C.-Y. Chuang, S.-E. Shai, S.-S. Yang, M.-C. Lee, and P.-C. Kwan, "Surgical–pathologic factors affect long-term outcomes in stage IB (pT2 n0 m0) non–small cell lung cancer: A heterogeneous disease," *The Journal of Thoracic and Cardiovascular Surgery*, vol. 138, no. 2, pp. 426–433, 2009.

[56] P. Giraud, M. Antoine, A. Larrouy, B. Milleron, P. Callard, Y. D. Rycke, M.-F. Carette, J.-C. Rosenwald, J.-M. Cosset, M. Housset, and E. Touboul, "Evaluation of microscopic tumor extension in non–small-cell lung cancer for three-dimensional conformal radiotherapy planning," *International Journal of Radiation Oncology, Biology, Physics*, vol. 48, no. 4, pp. 1015–1024, 2000. Publisher: Elsevier.

[57] S. Krauss, C. Perez, S. Lowenbraun, T. Sonoda, A. Bartolucci, and R. Buchanan, "Combined modality treatment of localized small-cell lung carcinoma. a randomized prospective study of the southeastern cancer study group," *Cancer Clinical Trials*, vol. 3, no. 4, pp. 297–305, 1980.

[58] F. L. Meyskens, E. B. Berglund, D. F. Saxe, B. B. Fuller, L. Z. Pacelli, J. D. Hall, and C. G. Ray, "Biological and biochemical properties of a human uveal melanocyte-derived cell line," *In Vitro*, vol. 16, no. 9, pp. 775–780, 1980.

[59] S. Shiono, M. Abiko, and T. Sato, "Positron emission tomography/computed tomography and lymphovascular invasion predict recurrence in stage i lung cancers," *Journal of Thoracic Oncology*, vol. 6, no. 1, pp. 43–47, 2011.

[60] K. A. Higgins, J. P. Chino, N. Ready, T. A. D'Amico, M. F. Berry, T. Sporn, J. Boyd, and C. R. Kelsey, "Lymphovascular invasion in non–small-cell lung cancer: Implications for staging and adjuvant therapy," *Journal of Thoracic Oncology*, vol. 7, no. 7, pp. 1141–1147, 2012.

[61] M. G. Oser, M. J. Niederst, L. V. Sequist, and J. A. Engelman, "Transformation from non-small-cell lung cancer to small-cell lung cancer: molecular drivers and cells of origin," *The Lancet Oncology*, vol. 16, no. 4, pp. e165–e172, 2015.

[62] M. Sánchez-Ortega, A. C. Carrera, and A. Garrido, "Role of nrf2 in lung cancer," *Cells*, vol. 10, no. 8, 2021.

[63] N. Basumallik and M. Agarwal, *Small Cell Lung Cancer*, ch. History and Physical. Treasure Island (FL): StatPearls Publishing, 2023.

[64] C. Gridelli, A. Rossi, and D. Carbone, "Non-small-cell lung cancer," *Nature Reviews Disease Primers*, 2015.

[65] S. Couraud, G. Zalcman, B. Milleron, F. Morin, and P.-J. Souquet, "Lung cancer in never smokers – a review," *European Journal of Cancer*, vol. 48, no. 9, pp. 1299–1311, 2012.

[66] B. Sabbula, D. Gasalberti, and S. Mukkamalla, *Squamous Cell Lung Cancer*, ch. Pathophysiology. Treasure Island (FL): StatPearls Publishing, 2024.

[67] J. Dusingize, M. Law, and M. Seviiri, "Genetic variants for smoking behaviour and risk of skin cancer," *Scientific Reports*, vol. 13, 2023.

[68] A. Arafa, A. Mostafa, and A. Navarini, "The association between smoking and risk of skin cancer: a meta-analysis of cohort studies," *Cancer Causes Control*, vol. 31, p. 787–794, 2020.

[69] Z. Fan and R. Schraeder, "The changing pathology of lung cancer," *Surgical Oncology Clinics of North America*, vol. 20, no. 4, pp. 637–653, 2011. Lung Cancer.

[70] J. Van Der Laak, G. Litjens, and F. Ciompi, "Deep learning in histopathology: the path to the clinic," *Nature Medicine*, vol. 27, pp. 775–784, 2021.

[71] H. Bečulić, E. Begagić, A. Džidić-Krivić, R. Pugonja, N. Softić, B. Bašić, S. Balogun, A. Nuhović, E. Softić, A. Ljevaković, H. Sefo, S. Šegalo, R. Skomorac, and M. Pojskić, "Sensitivity and specificity of machine learning and deep learning algorithms in the diagnosis of thoracolumbar injuries resulting in vertebral fractures: A systematic review and meta-analysis," *Brain and Spine*, vol. 4, p. 102809, 2024.

[72] E. Provenzano, O. J. Driskell, D. J. O'Connor, M. Rodriguez-Justo, J. McDermott, N. Wong, T. Kendall, Y. Z. Zhang, M. Robinson, K. M. Kurian, R. Pell, and A. M. Shaaban, "The important role of the histopathologist in clinical trials: challenges and approaches to tackle them," *Histopathology*, vol. 76, no. 7, pp. 942–949, 2020.

[73] R. Pell, K. Oien, M. Robinson, H. Pitman, N. Rajpoot, J. Rittscher, D. Snead, C. Verrill, and on behalf of the UK National Cancer Research Institute (NCRI) Cellular-Molecular Pathology (CM-Path) quality assurance working group, "The use of digital pathology and image analysis in clinical trials," *The Journal of Pathology: Clinical Research*, vol. 5, no. 2, pp. 81–90, 2019.

[74] N. Hashimoto, P. A. Bautista, H. Haneishi, M. Snuderl, and Y. Yagi, "Development of a 2D Image Reconstruction and Viewing System for Histological Images from Multiple Tissue Blocks: Towards High-Resolution Whole-Organ 3D Histological Images," *Pathobiology*, vol. 83, pp. 127–139, 04 2016.

[75] S. Chatterjee, "Artefacts in histopathology," *Journal of Oral and Maxillofacial Pathology*, vol. 18, 2014.

[76] S. A. Taqi, S. A. Sami, L. B. Sami, and S. A. Zaki, "A review of artifacts in histopathology," *Journal of Oral and Maxillofacial Pathology*, vol. 22, no. 2, 2018.

[77] G. Smit, F. Ciompi, M. Cigéhn, A. Bodén, J. van der Laak, and C. Mercan, "Quality control of whole-slide images through multi-class semantic segmentation of artifacts," in *Medical Imaging with Deep Learning*, 2021.

[78] S. Banerji and S. Mitra, "Deep learning in histopathology: A review," *WIREs Data Mining and Knowledge Discovery*, vol. 12, no. 1, p. e1439, 2022.

[79] Villarraga-Gómez, Herminso, Kotwal, Naomi, and Zarnetta, Robert, "Extending the measurement capabilities of 3d x-ray microscopy to dimensional metrology," *Int. J. Metrol. Qual. Eng.*, vol. 15, p. 5, 2024.

[80] S. Pacilè and G. Tromba, *Introduction to X-Ray Micro-tomography*, pp. 19–39. Cham: Springer International Publishing, 2018.

[81] M. Endrizzi, "X-ray phase-contrast imaging," *Nuclear Instruments and Methods in Physics Research Section A: Accelerators, Spectrometers, Detectors and Associated Equipment*, vol. 878, pp. 88–98, 2018. Radiation Imaging Techniques and Applications.

[82] S.-A. Zhou and A. Brahme, "Development of phase-contrast x-ray imaging techniques and potential medical applications," *Physica Medica*, vol. 24, no. 3, pp. 129–148, 2008.

[83] A. Rack, S. Zabler, B. Müller, H. Riesemeier, G. Weidemann, A. Lange, J. Goebbels, M. Hentschel, and W. Görner, "High resolution synchrotron-based radiography and tomography using hard x-rays at the bamline (bessy ii)," *Nuclear Instruments and Methods in Physics Research Section A: Accelerators, Spectrometers, Detectors and Associated Equipment*, vol. 586, no. 2, pp. 327–344, 2008.

[84] A. Peterzol, A. Olivo, L. Rigon, S. Pani, and D. Dreossi, "The effects of the imaging system on the validity limits of the ray-optical approach to phase contrast imaging," *Medical Physics*, vol. 32, no. 12, pp. 3617–3627, 2005.

[85] D. Paganin, S. C. Mayo, T. E. Gureyev, P. R. Miller, and S. W. Wilkins, "Simultaneous phase and amplitude extraction from a single defocused image of a homogeneous object," *Journal of Microscopy*, vol. 206, no. 1, pp. 33–40, 2002.

[86] P. Willmott, *Synchrotron Physics*, ch. 3, pp. 39–86. John Wiley & Sons, Ltd, 2011.

[87] O. Taubmann, M. Berger, M. Bögel, Y. Xia, M. Balda, and A. Maier, *Medical Imaging Systems: An Introductory Guide*, ch. Chapter 8 - Computed Tomography. Springer, 2018.

[88] M. Töpperwien, *3d virtual histology of neuronal tissue by propagation-based x-ray phase-contrast tomography*. Göttingen University Press, 2018.

[89] M. Eckermann, F. van der Meer, P. Cloetens, T. Ruhwedel, W. Möbius, C. Stadelmann, and T. Salditt, "Three-dimensional virtual histology of the cerebral cortex based on phase-contrast x-ray tomography," *Biomed. Opt. Express*, vol. 12, pp. 7582–7598, Dec 2021.

[90] M. Fratini, I. Bukreeva, G. Campi, F. Brun, G. Tromba, P. Modregger, D. Bucci, G. Battaglia, R. Spanò, M. Mastrogiacomo, H. Requardt, F. Giove, A. Bravin, and A. Cedola, "Simultaneous submicrometric 3d imaging of the micro-vascular network and the neuronal system in a mouse spinal cord," *Scientific Reports*, 2015.

[91] F. Palermo, N. Pieroni, A. Sanna, B. Parodi, C. Venturi, G. Begani Provinciali, L. Massimi, L. Maugeri, G. P. Marra, E. Longo, L. D'Amico, G. Saccomano, J. Perrin, G. Tromba, I. Bukreeva, M. Fratini, G. Gigli, N. Kerlero de Rosbo, and A. Cedola, "Multilevel x-ray imaging approach to assess the sequential evolution of multi-organ damage in multiple sclerosis," *Communications Physics*, 2022.

[92] A. Cedola, A. Bravin, I. Bukreeva, M. Fratini, A. Pacureanu, A. Mittone, L. Massimi, P. Cloetens, P. Coan, G. Campi, R. Spanò, F. Brun, V. Grigoryev, V. Petrosino, C. Venturi, M. Mastrogiacomo, N. Kerlero de Rosbo, and A. Uccelli, "X-ray phase contrast tomography reveals early vascular alterations and neuronal loss in a multiple sclerosis model," *Scientific Reports*, 2017.

[93] L. Massimi, I. Bukreeva, G. Santamaria, M. Fratini, A. Corbelli, F. Brun, S. Fumagalli, L. Maugeri, A. Pacureanu, P. Cloetens, N. Pieroni, F. Fiordaliso, G. Forloni, A. Uccelli, N. Kerlero de Rosbo, C. Balducci, and A. Cedola, "Exploring alzheimer's disease mouse brain through x-ray phase contrast tomography: From the cell to the organ," *NeuroImage*, vol. 184, pp. 490–495, 2019.

[94] J. Reichmann, S. E. Verleden, M. Kühnel, J. C. Kamp, C. Werlein, L. Neubert, J.-H. Müller, T. Q. Bui, M. Ackermann, D. Jonigk, and T. Salditt, "Human lung virtual histology by multi-scale x-ray phase-contrast computed tomography," *Physics in Medicine & Biology*, vol. 68, p. 115014, may 2023.

[95] M. Romano, A. Bravin, M. D. Wright, L. Jacques, A. Miettinen, R. Hlushchuk, J. Dinkel, S. Bartzsch, J. A. Laissue, V. Djonov, and P. Coan, "X-ray phase contrast 3d virtual histology: Evaluation of lung alterations after microbeam irradiation," *International journal of radiation oncology, biology, physics*, vol. 112, p. 818—830, March 2022.

[96] J. Albers, M. A. Markus, F. Alves, and C. Dullin, "X-ray based virtual histology allows guided sectioning of heavy ion stained murine lungs for histological analysis," *Scientific reports*, vol. 8, p. 7712, May 2018.

[97] R. P. Xian, C. L. Walsh, S. E. Verleden, W. L. Wagner, A. Bellier, S. Marussi, M. Ackermann, D. D. Jonigk, J. Jacob, P. D. Lee, and P. Tafforeau, "A multiscale x-ray phase-contrast tomography dataset of a whole human left lung," *Scientific Data*, 2022.

[98] C. L. Walsh, P. Tafforeau, W. L. Wagner, D. J. Jafree, A. Bellier, C. Werlein, M. P. Kühnel, E. Boller, S. Walker-Samuel, J. L. Robertus, D. A. Long, J. Jacob, S. Marussi, E. Brown, N. Holroyd, D. D. Jonigk, M. Ackermann, and P. D. Lee, "Imaging intact human organs with local resolution of cellular structures using hierarchical phase-contrast tomography," *Nature Methods*, 2021.

[99] M. Eckermann, J. Frohn, M. Reichardt, M. Osterhoff, M. Sprung, F. Westermeier, A. Tzankov, C. Werlein, M. Kühnel, D. Jonigk, and T. Salditt, "3d virtual pathohistology of lung tissue from covid-19 patients based on phase contrast x-ray tomography," *eLife*, vol. 9, p. e60408, aug 2020.

[100] L. D'Amico, A. Svetlove, E. Longo, R. Meyer, B. Senigagliesi, G. Saccomano, P. Nolte, W. L. Wagner, M. O. Wielpütz, D. H. Leitz, J. Duerr, M. A. Mall, L. Casalis, S. Köster, F. Alves, G. Tromba, and C. Dullin, "Characterization of transient and progressive pulmonary fibrosis by spatially correlated phase contrast microct, classical histopathology and atomic force microscopy," *Computers in Biology and Medicine*, vol. 169, p. 107947, 2024.

[101] M. D. Wong, A. E. Dorr, J. R. Walls, J. P. Lerch, and R. M. Henkelman, "A novel 3D mouse embryo atlas based on micro-CT," *Development*, vol. 139, pp. 3248–3256, 09 2012.

[102] B. Metscher, "Microct for comparative morphology: simple staining methods allow high-contrast 3d imaging of diverse non-mineralized animal tissues," *BMC Physiol*, vol. 9, 2009.

[103] T. H. Jensen, M. Bech, T. Binderup, A. Böttiger, C. David, T. Weitkamp, I. Zanette, E. Reznikova, J. Mohr, F. Rank, R. Feidenhans'l, A. Kjær, L. Højgaard, and F. Pfeiffer, "Imaging of metastatic lymph nodes by x-ray phase-contrast micro-tomography," *PLOS ONE*, vol. 8, pp. 1–5, 01 2013.

[104] X. Li, Z. Chen, L. Zhang, X. Zhu, S. Wang, and W. Peng, "Quantitative characterization of ex vivo breast tissue via x-ray phase-contrast tomography," *Journal of X-Ray Science and Technology*, 2019.

[105] T. E. Gureyev, Y. I. Nesterets, P. M. Baran, S. T. Taba, S. C. Mayo, D. Thompson, B. Arhatari, A. Mihocic, B. Abbey, D. Lockie, J. Fox, B. Kumar, Z. Prodanovic, D. Hausermann, A. Maksimenko, C. Hall, A. G. Peele, M. Dimmock, K. M. Pavlov, M. Cholewa, S. Lewis, G. Tromba, H. M. Quiney, and P. C. Brennan, "Propagation-based x-ray phase-contrast tomography of mastectomy samples using synchrotron radiation," *Medical Physics*, vol. 46, no. 12, pp. 5478–5487, 2019.

[106] S. Donato, L. M. Arana Peña, F. Arfelli, L. Brombal, L. Colmo, R. Longo, F. Martellani, G. Tromba, F. Zanconati, and D. Bonazza, "Integrating x-ray phase-contrast imaging and histology for comparative evaluation of breast tissue malignancies in virtual histology analysis," *Scientific Reports*, vol. 14, no. 1, p. 5831, 2024.

[107] S. Donato, R. Agostino, L. Arana Peña, F. Arfelli, L. Brombal, R. Longo, F. Martellani, A. Romano, I. Rosano, G. Saccomano, G. Tromba, and D. Bonazza, "Unveiling tumor invasiveness: enhancing cancer diagnosis with phase-contrast microtomography for 3d virtual histology," *Eur. Phys. J. Plus*, vol. 139, 2024.

[108] L. Arana Peña, S. Donato, D. Bonazza, L. Brombal, F. Martellani, F. Arfelli, G. Tromba, and R. Longo, "Multiscale x-ray phase-contrast tomography: From breast ct to micro-ct for virtual histology," *Physica Medica*, vol. 112, p. 102640, 2023.

[109] J. Frohn, D. Pinkert-Leetsch, J. Missbach-Güntner, M. Reichardt, M. Osterhoff, F. Alves, and T. Salditt, "3D virtual histology of human pancreatic tissue by multiscale phase-contrast X-ray tomography," *Journal of Synchrotron Radiation*, vol. 27, pp. 1707–1719, Nov 2020.

[110] D. Pinkert-Leetsch, J. Frohn, and P. Ströbel, "Three-dimensional analysis of human pancreatic cancer specimens by phase-contrast based x-ray tomography – the next dimension of diagnosis," *Cancer Imaging*, vol. 23, 2023.

[111] M. Saccomano, J. Albers, G. Tromba, M. Dobrivojević Radmilović, S. Gajović, F. Alves, and C. Dullin, "Synchrotron inline phase contrast μCT enables detailed virtual histology of embedded soft-tissue samples with and without staining," *Journal of Synchrotron Radiation*, vol. 25, pp. 1153–1161, Jul 2018.

[112] G. A. Salg, V. Steinle, J. Labode, W. Wagner, A. Studier-Fischer, J. Reiser, E. Farjallah, M. Guettlein, J. Albers, T. Hilgenfeld, N. A. Giese, W. Stiller, F. Nickel, M. Loos, C. W. Michalski, H.-U. Kauczor, T. Hackert, C. Dullin, P. Mayer, and H. G. Kenngott, "Multiscale and multimodal imaging for three-dimensional vascular and histomorphological organ structure analysis of the pancreas," *Scientific Reports*, 2024.

[113] J. Novo Matos, P. Garcia-Canadilla, I. C. Simcock, J. C. Hutchinson, M. Dobromylskyj, A. Guy, O. J. Arthurs, A. C. Cook, and V. Luis Fuentes, "Micro-computed tomography (micro-ct) for the assessment of myocardial disarray, fibrosis and ventricular mass in a feline model of hypertrophic cardiomyopathy," *Scientific Reports*, 2020.

[114] M. Reichardt, P. Moller Jensen, V. Andersen Dahl, A. Bjorholm Dahl, M. Ackermann, H. Shah, F. Länger, C. Werlein, M. P. Kuehnel, D. Jonigk, and T. Salditt, "3d virtual histopathology of cardiac tissue from covid-19 patients based on phase-contrast x-ray tomography," *eLife*, vol. 10, p. e71359, dec 2021.

[115] M. Chourrout, H. Rositi, E. Ong, V. Hubert, A. Paccalet, L. Foucault, A. Autret, B. Fayard, C. Olivier, R. Bolbos, F. Peyrin, C. C. da Silva, D. Meyronet, O. Raineteau, H. Elleaume, E. Brun, F. Chauveau, and M. Wiart, "Brain virtual histology with x-ray phase-contrast tomography part i: whole-brain myelin mapping in white-matter injury models," *Biomed. Opt. Express*, vol. 13, pp. 1620–1639, Mar 2022.

[116] J. Y. Lee, S. Donato, A. F. Mack, U. Mattheus, G. Tromba, E. Longo, L. D'Amico, S. Mueller, T. Shiozawa, J. Bause, K. Scheffler, R. Longo, and G. E. Hagberg, "Protocol for 3d virtual histology of unstained human brain tissue using synchrotron radiation phase-contrast microtomography," *Frontiers in Physics*, vol. 11, 2024.

[117] G. Litjens, T. Kooi, B. E. Bejnordi, A. A. A. Setio, F. Ciompi, M. Ghafoorian, J. A. van der Laak, B. van Ginneken, and C. I. Sánchez, "A survey on deep learning in medical image analysis," *Medical Image Analysis*, vol. 42, pp. 60–88, 2017.

[118] Y. Mo, Y. Wu, X. Yang, F. Liu, and Y. Liao, "Review the state-of-the-art technologies of semantic segmentation based on deep learning," *Neurocomputing*, vol. 493, pp. 626–646, 2022.

[119] B. Emek Soylu, M. S. Guzel, G. E. Bostanci, F. Ekinci, T. Asuroglu, and K. Acici, "Deep-learning-based approaches for semantic segmentation of natural scene images: A review," *Electronics*, vol. 12, no. 12, 2023.

[120] C. L. Srinidhi, O. Ciga, and A. L. Martel, "Deep neural network models for computational histopathology: A survey," *Medical Image Analysis*, vol. 67, p. 101813, 2021.

[121] S. Wang, D. M. Yang, R. Rong, X. Zhan, and G. Xiao, "Pathology image analysis using segmentation deep learning algorithms," *The American Journal of Pathology*, vol. 189, no. 9, pp. 1686–1698, 2019.

[122] Mathworks, "Convolutional neural network." `https://it.mathworks.com/discovery/convolutional-neural-network.html`. [Online; Accessed September-20-2024].

[123] E. Longo, A. Contillo, L. D'Amico, M. Prasek, G. Saccomano, N. Sodini, C. Dullin, D. Dreossi, and G. Tromba, "Syrmep beamline: state of the art, upgrades and future prospects," *Eur. Phys. J. Plus*, vol. 139, 2024.

[124] F. Brun, L. Massimi, and M. Fratini, "Syrmep tomo project: a graphical user interface for customizing ct reconstruction workflows," *Adv Struct Chem Imag*, 2017.

[125] F. Brun, G. Kourousias, D. Dreossi, and L. Mancini, "An improved method for ring artifacts removing in reconstructed tomographic images," in *World Congress on Medical Physics and Biomedical Engineering, September 7 - 12, 2009, Munich, Germany* (O. Dössel and W. C. Schlegel, eds.), (Berlin, Heidelberg), pp. 926–929, Springer Berlin Heidelberg, 2010.

[126] M. Berger, J. Hubbell, S. Seltzer, J. Chang, J. Coursey, R. Sukumar, D. Zucker, and K. Olsen, "Xcom: Photon cross sections database. nist standard reference database 8 (xgam)," *NIST, PML, Radiation Physics Division*, 2010.

[127] F. Isensee, P. F. Jaeger, S. A. Kohl, J. Petersen, and K. H. Maier-Hein, "nnu-net: a self-configuring method for deep learning-based biomedical image segmentation," *Nature methods*, vol. 18, no. 2, pp. 203–211, 2021.

[128] S. van der Walt, J. L. Schönberger, J. Nunez-Iglesias, F. Boulogne, J. D. Warner, N. Yager, E. Gouillart, T. Yu, and the scikit-image contributors, "scikit-image: image processing in python," *PeerJ*, vol. 2, p. e453, jun 2014.

[129] J. D. Hunter, "Matplotlib: A 2d graphics environment," *Computing in Science & Engineering*, vol. 9, no. 3, pp. 90–95, 2007.

[130] K. Martinez and J. Cupitt, "Vips - a highly tuned image processing software architecture," in *IEEE International Conference on Image Processing 2005*, vol. 2, pp. II–574, 2005.

[131] P. Bankhead, M. Loughrey, and J. Fernández, "Qupath: Open source software for digital pathology image analysis," *Sci Rep*, vol. 7, 2017.

[132] C. Studholme, D. Hill, and D. Hawkes, "An overlap invariant entropy measure of 3d medical image alignment," *Pattern Recognition*, vol. 32, no. 1, pp. 71–86, 1999.

[133] V. D. Trapani, S. Savatović, F. D. Marco, G. Lautizi, M. Margini, and P. Thibault, "Speckle-based imaging (sbi) applications with spectral photon counting detectors at the newly established optimato (optimal imaging and tomography) laboratory," *Journal of Instrumentation*, vol. 19, p. C01018, jan 2024.

[134] A. Biguri, M. Dosanjh, S. Hancock, and M. Soleimani, "Tigre: a matlab-gpu toolbox for cbct image reconstruction," *Biomedical Physics & Engineering Express*, vol. 2, p. 055010, sep 2016.

[135] S. Donato, L. A. Peña, D. Bonazza, V. Formoso, R. Longo, G. Tromba, and L. Brombal, "Optimization of pixel size and propagation distance in x-ray phase-contrast virtual histology," *Journal of Instrumentation*, vol. 17, p. C05021, may 2022.

[136] E. De Martino, C. Medeot, L. D'Amico, G. Stanta, and S. Bonin, "Impact of standardization in tissue processing: the performance of different fixatives," *New Biotechnology*, vol. 71, pp. 30–36, 2022.

[137] K. Tajbakhsh, A. Neels, E. Fadeeva, J. C. Larsson, O. Stanowska, A. Perren, and R. Zboray, "A comprehensive study of laboratory-based micro-ct for 3d virtual histology of human ffpe tissue blocks," *IEEE Access*, vol. 12, pp. 78304–78316, 2024.

[138] J. DeFazio, I. Zalaudek, K. J. Busam, C. Cota, and A. Marghoob, "Association between melanocytic neoplasms and seborrheic keratosis: more than a coincidental collision," *Dermatology Practical & Conceptual*, p. 35–41, 2012.

[139] M. J. Welsch, B. M. Troiani, L. Hale, J. DelTondo, K. F. Helm, and L. E. Clarke, "Basal cell carcinoma characteristics as predictors of depth of invasion," *Journal of the American Academy of Dermatology*, vol. 67, no. 1, pp. 47–53, 2012.

[140] G. Saccomano, M. Pinamonti, E. Longo, T. Marcuzzo, G. Tromba, D. Dreossi, and F. Brun, "The potential of x-ray virtual histology in the diagnosis of skin tumors," *Skin Research and Technology*, vol. 30, no. 10, p. e13801, 2024.

[141] H. W. Higgins, K. C. Lee, A. Galan, and D. J. Leffell, "Melanoma in situ: Part ii. histopathology, treatment, and clinical management," *Journal of the American Academy of Dermatology*, vol. 73, no. 2, pp. 193–203, 2015.

[142] M. Garutti, R. Bruno, J. Polesel, M. A. Pizzichetta, and F. Puglisi, "Role of tumor-infiltrating lymphocytes in melanoma prognosis and treatment strategies: A systematic review and meta-analysis," *Heliyon*, vol. 10, no. 12, p. e32433, 2024.

[143] M. Bønnelykke-Behrndtz and T. Steiniche, *Cutaneous Melanoma: Etiology and Therapy*, ch. Ulcerated Melanoma: Aspects and Prognostic Impact. Brisbane (AU): Codon Publications, 2017.

[144] R. G. Ladstein, I. M. Bachmann, O. Straume, and L. A. Akslen, "Tumor necrosis is a prognostic factor in thick cutaneous melanoma," *The American Journal of Surgical Pathology*, 2012.

[145] J. Spronck, T. Gelton, L. van Eekelen, J. Bogaerts, L. Tessier, M. van Rijthoven, L. van der Woude, M. van den Heuvel, W. Theelen, J. van der Laak, and F. Ciompi, "nnunet meets pathology: Bridging the gap for application to whole slide images and computational biomarkers," in *Medical Imaging with Deep Learning*, vol. 227 of *Proceedings of Machine Learning Research*, pp. 1859–1874, PMLR, 10–12 Jul 2024.

[146] W. D. Travis, E. Brambilla, A. G. Nicholson, Y. Yatabe, J. H. M. Austin, M. B. Beasley, L. R. Chirieac, S. Dacic, E. Duhig, D. B. Flieder, K. Geisinger, F. R. Hirsch, Y. Ishikawa, K. M. Kerr, M. Noguchi, G. Pelosi, C. A. Powell, M. S. Tsao, and I. Wistuba, "The 2015 world health organization classification of lung tumors: Impact of genetic, clinical and radiologic advances since the 2004 classification," *Journal of Thoracic Oncology*, vol. 10, no. 9, pp. 1243–1260, 2015. Publisher: Elsevier.

[147] E. Kuhn, P. Morbini, A. Cancellieri, S. Damiani, A. Cavazza, and C. Comin, "Adenocarcinoma classification: patterns and prognosis," *Pathologica*, vol. 110, pp. 5–11, 2018.

[148] L. Solis, C. Behrens, M. Raso, H. Lin, H. Kadara, P. Yuan, H. Galindo, X. Tang, J. Lee, N. Kalhor, I. Wistuba, and C. Moran, "Histologic patterns and molecular characteristics of lung adenocarcinoma associated with clinical outcome," *Cancer*, vol. 118, pp. 2889–2899, 2012.

[149] K. Kadota, J. ichi Nitadori, C. S. Sima, H. Ujiie, N. P. Rizk, D. R. Jones, P. S. Adusumilli, and W. D. Travis, "Tumor spread through air spaces is an important pattern of invasion and impacts the frequency and location of recurrences after limited resection for small stage i lung adenocarcinomas," *Journal of Thoracic Oncology*, vol. 10, no. 5, pp. 806–814, 2015.

[150] R. F. Walters, P. A. Groben, K. Busam, R. C. Millikan, H. Rabinovitz, A. Cognetta, M. C. J. Mihm, V. G. Prieto, P. B. Googe, R. King, D. Moore, J. Woosley, and N. E. Thomas, "Consumption of the epidermis: A criterion in the differential diagnosis of melanoma and dysplastic nevi that is associated with increasing breslow depth and ulceration," *The American Journal of Dermatopathology*, vol. 29, pp. 527–533, 2007.

[151] M. L. Onozato, V. E. Klepeis, Y. Yagi, and M. Mino-Kenudson, "A role of three-dimensional (3d) reconstruction in the classification of lung adenocarcinoma," *Studies in health technology and informatics*, vol. 179, pp. 250–256, 2012.

[152] M. L. Onozato, A. E. Kovach, B. Y. Yeap, V. Morales-Oyarvide, V. E. Klepeis, S. Tammireddy, R. S. Heist, E. J. Mark, D. Dias-Santagata, A. J. Iafrate, and M. Yagi, Yukako and; Mino-Kenudson, "Tumor islands in resected early-stage lung adenocarcinomas are associated with unique clinicopathologic and molecular characteristics and worse prognosis," *The American Journal of Surgical Pathology*, vol. 37, pp. 287–294, 2013.

[153] Y. Yagi, R. G. Aly, K. Tabata, A. Barlas, N. Rekhtman, T. Eguchi, J. Montecalvo, M. Hameed, K. Manova-Todorova, P. S. Adusumilli, and W. D. Travis, "Three-dimensional histologic, immunohistochemical, and multiplex immunofluorescence analyses of dynamic vessel co-option of spread through air spaces in lung adenocarcinoma," *Journal of Thoracic Oncology*, vol. 15, 2020.

Acknowledgements

The first person I would like to thank is the one who guided me during this amazing and complex journey. He encouraged me to pursue the PhD and was there for me every step of the way with precise and good mentorship. We had “fun and science” around Europe, and I am confident that new adventures will come. Thank you to being my mentor, Prof. Francesco Brun.

I would also like to express my gratitude to Prof. Francesco Ciompi for accepting me into your group during my traineeship abroad. Your advices were essential in developing a portion of my PhD project and providing new and innovative research ideas. I also want to thank you for believing in our collaboration, and I am certain that we will maintain it in the future.

I would like to extend my sincerest thanks to MD Maurizio Pinamonti, who provided me with invaluable assistance and guidance on medical matters throughout these three years.

I would acknowledge the group established by MD Elisa Baratella, MD Stefano Lovadina, and MD Fulvia Martellani. I am grateful for your enthusiasm and kind assistance in this project.

I am proud to thank the entire SYRMEP group for these intense years together. I would like to thank Dr. Diego Dreossi for assisting me at the SYRMEP beamline and laboratories. I am grateful for your guidance in learning the fundamentals of X-rays and micro-Tomography, as well as for introducing me to new challenges in this field. To Dr. Giuliana Tromba, for your enthusiasm and for always believing in the potential of the Young Syrmep group. Thanks to Dr. Lorenzo D’Amico for being PhD student buddies in all these years. To the amazing Postdoc researchers - Dr. Elena Longo, Dr. Marko Kudrna Prasek and Dr. Simone Lemmers - for your precious support while I was pursuing my PhD. And finally, to Dr. Nicola Sodini and Dr. Adriano Contillo for your rapid and constant encouragement.

I am pleased to thank Prof. Pierre Thibault and Dr. Luca Brombal for the collaboration established at the OptImaTo and PEPI laboratories, respectively. A great thanks also to Dr. Vittorio Di Trapani for your dedicated and intense work in this research.

I would also like to thank all the colleagues I met at Radboudumc for all your kindness and enthusiasm, as well as for sharing your knowledge with me. A particular thank to Giulia Nicoletti for being a great friend and colleague there and providing invaluable decision-making support.

Un sentito ringraziamento va soprattutto alla mia famiglia: mamma Antonella e papà Lorenzo, i quali mi hanno sempre supportato in ogni scelta e in ogni modo, e mia sorella Mara, la prima Dr. Saccomano della famiglia, la cui carriera accademica

è stata per me grande fonte di ispirazione. Ti ringrazio tantissimo per tutti i consigli e il confronto costante.

Ci tengo a ringraziare di cuore il mio ragazzo Riccardo per avermi motivato costantemente con entusiasmo durante l'intero percorso di dottorato e per l'enorme aiuto come correttore di bozze. Ti ringrazio nel credere fortemente nelle mie potenzialità.

In ultimo, ma non meno importanti, un pensiero va al resto della mia famiglia e tutti i miei amici (ormai sparsi per il mondo) per essere sempre al mio fianco.

List of Publications

- **G. Saccomano**, M. Pinamonti, F. Ciompi, and F. Brun, "3D Breslow Thickness estimation of melanocytic lesion", manuscript in preparation, 2024.
- **G. Saccomano**, F. Martellani, S. Lovadina, M. A. Cova, F. Brun, and E. Baratella, "Spread-Through Air Spaces (STAS) investigation in NSCLC employing X-ray Virtual Histology", manuscript in preparation, 2024.
- **G. Saccomano**, M. Pinamonti, F. Ciompi, D. Dreossi, and F. Brun, "Precise 3D invasiveness detection for skin tumors diagnosis using X-ray Virtual Histology", in 36th European Congress of Pathology – Abstracts, Virchows Archive, 485 (Suppl 1), pp. 119, 2024. https://doi.org/10.1007/s00428-024-03880-y
- **G. Saccomano**, M. Pinamonti, T. Marcuzzo, E. Longo, G. Tromba, D. Dreossi, and F. Brun, "The potential of X-ray Virtual Histology in the diagnosis of skin tumors", Skin Research and Technology, 2024. https://doi.org/10.1111/srt.138012024
- T. Sepperer †, **G. Saccomano** †, D. E. Bedolla †, R.J.F. Berger, P. Šket, E. Longo, D. Dreossi, L. Vaccari, M. Musso, and F. D'Amico, "Chemical and structural characterization of tannin-furanic foams using x-ray Phase contrast Computed micro-Tomography, Nuclear Magnetic Resonance, Fourier-Transformed Infrared imaging and UV Resonant Raman scattering", submitted to Materials & Design, 2024. https://doi.org/10.1016/j.matdes.2024.113538
- A. G. Zippo, V. Rodriguez-Menendez, E.Pozzi, A. Canta, Alessia Chiorazzi, E. Ballarini, L. Monza, P. Alberti, C. Meregalli, A. Bravin, P. Coan, E. Longo, **G. Saccomano**, K. Paiva, G. Tromba, G. Cavaletti, V. Carozzi, "Paclitaxel alters the microvascular network in the central and peripheral nervous system of rats with chemotherapy-induced painful peripheral neuropathy", Journal of the Peripheral Nervous System, 2024. https://doi.org/10.1111/jns.12660
- V. Carozzi, V. Rodriguez-Menendez, E. Pozzi, A. Canta, A. Chiorazzi, N. Cordani, P. Alberti, C. Meregalli, E. Longo, **G. Saccomano**, G. Tromba, E. Donà, G. Cavaletti, and A. Zippo, "Central and peripheral microvascular network is abnormal in rats with painful-chemotherapy induced neuropathy: new pathophysiological mechanisms over the horizon?", Journal of the Peripheral Nervous System, 2024. https://doi.org/10.1111/jns.12627

- F. Palermo, A. Sanna, Consuelo Venturi, L. Massimi, L. Maugeri, E. Longo, L. D'Amico, **G. Saccomano**, J. Perrin, G. Tromba, I. Bukreeva, M. Fratini, G. P. Marra, G. Gigli, N. Kerlero de Rosbo, and A. Cedola, "Multilevel x-ray imaging approach to assess the sequential evolution of multi-organ damage in neurodegenerative diseases", Proc. SPIE 13152, Developments in X-Ray Tomography XV, 2024. https://doi.org/10.1117/12.3027596

- E. Longo, A. Contillo, L. D'Amico, M. Prasek, **G. Saccomano**, N. Sodini, C. Dullin, D. Dreossi, and G. Tromba, "SYRMEP beamline: state of the art, upgrades and future prospects", European Physics Journal Plus, 139, 880, 2024. https://doi.org/10.1140/epjp/s13360-024-05489-1

- S. Donato, R.G. Agostino, L.M. Arana Peña, F. Arfelli, L. Brombal, R. Longo, F. Martellani, A. Romano, I. Rosano, **G. Saccomano**, G. Tromba, and D. Bonazza, "Unveiling tumor invasiveness: enhancing cancer diagnosis with phase-contrast microtomography for 3D virtual histology", European Physics Journal Plus, 139: 413, 2024. https://doi.org/10.1140/epjp/s13360-024-05188-x

- L. D'Amico, A. Svetlove, E. Longo, R. Meyer, B. Senigagliesi, **G. Saccomano**, P. Nolte, W. L. Wagner, M. O. Wielpütz, D. H. Leitz, J. Duerr, M. A. Mall, L. Casalis, S. Köster, F. Alves, G. Tromba, and C. Dullin, "Characterization of transient and progressive pulmonary fibrosis by spatially correlated phase contrast microct, classical histopathology and atomic force microscopy", Computers in Biology and Medicine, 169, 2024. https://doi.org/10.1016/j.compbiomed.2024.107947

- **G. Saccomano**, L. Brombal, D. Dreossi, M. Pinamonti, G. Tromba, and F. Brun, "Towards 3d virtual histology of melanoma tissue by means of lab-based x-ray phase contrast computed micro-tomography", in Eighth National Congress of Bioengineering proceedings, pp. 617–620, 2023. http://gnb2023.it/assets/img/proceedings_gnb2023.pdf

- C. Dullin, L. D'Amico, **G. Saccomano**, E. Longo, W. L. Wagner, J. Reiser, A. Svetlove, J. Albers, A. Contillo, A. Abrami, L. Sturari, G. Tromba, N. Sodini, and D. Dreossi, "Novel setup for rapid phase contrast ct imaging of heavy and bulky specimens", Journal of Synchrotron Radiation, 30(3), pp. 650–654, 2023. https://doi.org/10.1107/S1600577523001649

- L. D'Andrea, D. Gastaldi, F. Baino, E. Verné, **G. Saccomano**, L. D'Amico, E. Longo, M. Schwentenwein, and P. Vena, "Mechanical characterization of miniaturized 3d-printed hydroxyapatite parts obtained through vat photopolymerization: an experimental study", Journal of the Mechanical Behavior of Biomedical Materials, 141, 2023. https://doi.org/10.1016/j.jmbbm.2023.105760

- D. H. Ebner †, M. Tortora †, D. E. Bedolla †, **G. Saccomano** †, L. Vaccari, M.-C. Barbu, J. Grzybek, and T. Schnabel, "Comparative investigation of

chemical and structural properties of charred fir wood samples by raman and ftir spectroscopy as well as x-ray-micro-ct technology", Holzforschung, 77(9), pp. 734-742, 2023. https://doi.org/10.1515/hf-2023-0024

- F. Palermo, N. Pieroni, A. Sanna, B. Parodi, C. Venturi, G. Begani Provinciali,L. Massimi, L. Maugeri, G. P. Marra, E. Longo, L. D'Amico, **G. Saccomano**, J. Perrin, G. Tromba, I. Bukreeva, M. Fratini, G. Gigli, N. Kerlero de Rosbo, and A. Cedola, "Multilevel x-ray imaging approach to assess the sequential evolution of multi-organ damage in multiple sclerosis", Communications Physics, 5, 290, 2022. https://doi.org/10.1038/s42005-022-01070-32022

- K. Hickman-Lewis, B. Cavalazzi, K. Giannoukos, L. D'Amico, S. Vrbaski, **G. Saccomano**, D. Dreossi, G. Tromba, F. Foucher, W. Brownscombe, C. Smith, and F. Westall, "Advanced two- and three-dimensional insights into Earth's oldest stromatolites (ca. 3.5 Ga): Prospects for the search for life on Mars", Geology, 51(1), pp. 33-38, 2022. https://doi.org/10.1130/G50390.1

- J. Torres-Rodriguez, D. E. Bedolla, F. D'Amico, A.-K. Koopmann, L. Vaccari, **G. Saccomano**, R. Kohns, and N. Huesing, "Polyvinylidene fluoride aerogels with tailorable crystalline phase composition", Gels, 8(11), 727, 2022. https://doi.org/10.3390/gels8110727

- **G. Saccomano**, V. Di Trapani, P. Delogu, and F. Brun, "No-reference evaluation of the reconstructed images in single-shot K-Edge Subtraction X-ray Computed Tomography", in Seventh National Congress of Bioengineering proceedings, 7, pp. 383-386, 2020.https://www.grupponazionalebioingegneria.it/wp-content/uploads/2022/01/GNB2020_Proceedings_full.pdf

† : equal contribution to the work.

Conference Poster presentations:

- **G. Saccomano**, M. Pinamonti, F. Ciompi, D. Dreossi, and F. Brun, "Precise 3D invasiveness detection for skin tumors diagnosis using X-ray Virtual Histology" in European Society of Pathology (ECP24 Florence, Italy), 2024.
- **G. Saccomano**, L. Brombal, D. Dreossi, M. Pinamonti, G. Tromba, and F. Brun, "Towards 3d virtual histology of melanoma tissue by means of lab-based x-ray phase contrast computed micro-tomography" in Eighth National Congress of Bio-engineering (GNB23 Padua, Italy), 2023.
- **G. Saccomano**, L. Brombal, D. Dreossi, M. Pinamonti, G. Tromba, and F. Brun, "3D virtual histology of melanoma tissue by means of lab-based X-ray phase-contrast computed micro-tomography" in Bioengineering Solutions for Biology and Medicine conference (BIOENG22 Munich, Germany), 2022. *European Travel Grant awarded.*

Experimental experiences in synchrotron facilities (access with proposal):

- Co-author of the proposal no. 20230337 with the title "X-ray virtual histology for the 3D assessment of lymphovascular invasion in resected non–small cell lung cancer" at the SYRMEP beamline, Elettra Sincrotrone, Basovizza IT. November 2023.
- Main proposer of proposal no. 20225155 with the title "X-ray Phase Contrast 3D Virtual Histology for the assessment of staging in human melanoma tissue" at the SYRMEP beamline, Elettra Sincrotrone, Basovizza IT. May 2023.
- Co-author of the proposal no. LS-3190 with the title "X-ray holotomography of human ovarian tissue samples and monitoring cryopreservation effects" at the Id16a beamline, European synchrotron facility, Grenoble FR. May 2023.
- Co-author of the proposal no. 32149 with the title "3D Characterization of Hybrid Nanoplatforms for Theranostic Applications in Hepatocellular Carcinoma (HCC)" at the I13 beamline, Diamond light source, Didcot UK. September 2022.

Workshop and summer school experiences:

- Attendance at "XLIII GNB Annual School 2024: Neurotechnologies to understand and restore the nervous system" in Bressanone IT. September 2024. *Best project awarded.*

- Virtual participation at “3D biomedical imaging with synchrotron radiation: State-of-the-art and future possibilities”. May 2024.
- Participation at “International School on Advanced Imaging Techniques” in Pavia IT. September 2022.
- Virtual attendance at “International Conference of Industrial Computed Tomography”. February 2022.